INTERPHASE

On Nanofabrication and Electrical Double Layer Dynamics with Electrochemical Scanning Probes

Ph.D. Thesis, University of Amsterdam, January 2021
Interphase: On Nanofabrication and Electrical Double Layer dynamics with Electrochemical scanning probes
Mark Aarts

ISBN: 978-94-92323-45-3

The work described in this thesis was performed at
NWO-Institute AMOLF, Science Park 104, 1098 XG Amsterdam, The Netherlands.

This work is part of the Dutch Research Council (NWO).

A digital version of this thesis can be downloaded from
http://www.amolf.nl

INTERPHASE

On Nanofabrication and Electrical Double Layer Dynamics with Electrochemical Scanning Probes

ACADEMISCH PROEFSCHRIFT

ter verkrijging van de graad van doctor

aan de Universiteit van Amsterdam

op gezag van de Rector Magnificus

prof. dr. ir. K.I.J. Maex

ten overstaan van een door het College voor Promoties ingestelde commissie,

in het openbaar te verdedigen in de Agnietenkapel

op dinsdag 26 januari 2021, te 15:00 uur

door Mark Aarts

geboren te Leiden

Promotiecommissie

Promotor:	prof. dr. A. Polman	Universiteit van Amsterdam
Copromotor:	dr. E. Alarcón-Lladó	AMOLF

Overige leden:

prof. dr. J.W.M. Frenken	Universiteit van Amsterdam
prof. dr. P. Schall	Universiteit van Amsterdam
dr. K. Newell	Universiteit van Amsterdam
prof. dr. F.G. Mugele	Universiteit Twente
prof. dr. P.E. de Jongh	Universiteit Utrecht

Faculteit der Natuurwetenschappen, Wiskunde en Informatica.

Table of Contents

Table of Contents iii

1 Introduction 1

1-1 Electrocrystallization . . . 2

1-2 The Solid-liquid Interface . . . 6

1-3 Electrochemical Scanning Probe NanoLithography . . . 8

1-4 Direct current (DC) nanoscale electrochemistry . . . 11

1-5 Outline of the thesis . . . 15

2 Direct nanoscale writing through double layer perturbation 17

2-1 Introduction . . . 17

2-2 Direct writing of copper nanostructures . . . 18

2-3 Influence of electrochemical parameters . . . 20

2-4 Influence of tapping dynamics . . . 21

2-5 Discussion . . . 23

2-6 Conclusion . . . 25

2-7 Methods . . . 26

2-8 Supplementary information . . . 28

3 Shape evolution in nanoscale electrocrystallization 35

3-1 Introduction . . . 35

3-2 Out-of-plane growth . . . 36

3-3 Nanoscale shapes . . . 37
3-4 Growth from a dilute 1 μM $CuSO_4$ electrolyte . . . 40
3-5 Statistical analysis of growth . . . 42
3-6 Conclusion . . . 43
3-7 Methods . . . 44

4 Pulsed electrochemical scanning probe nano-lithography 47
4-1 Introduction . . . 47
4-2 Comparing diffuse layer charge relaxation to machining literature . . . 49
4-3 Nanoscale electrodeposition with an STM . . . 50
4-4 Conclusion . . . 55
4-5 Methods . . . 55
4-6 Supplementary information . . . 57

5 Potential dependent adhesion mapping 61
5-1 Introduction . . . 61
5-2 Adhesion mapping with potential control . . . 62
5-3 Conclusion . . . 67
5-4 Methods . . . 67
5-5 Supplementary information . . . 69

6 Nanofluidics in microscopic systems 73
6-1 Introduction . . . 73
6-2 Conductance measurements in an asymmetric microchannel . . . 75
6-3 Ion current rectification . . . 78
6-4 Conclusion . . . 79
6-5 Methods . . . 80
6-6 Supplementary information . . . 81

Summary 83

Samenvatting 85

List of Publications 89

Acknowledgements 91

References 93

Chapter 1

Introduction

Few things have impacted modern society as much as the advent of nanotechnology, which is now ever present in industries, homes, and pockets. However, with the famously predicted room at the bottom indeed being 'plenty', this description is less applicable to the amount of techniques capable of patterning at the smallest scales. Large-scale nanofabrication is in fact dominated by optical lithography, which is increasingly running into resolution limits imposed by the wavelength of the used light. Resolving this by the use of smaller wavelengths is possible (up to a point), but very costly, with ASML's latest extreme ultraviolet lithography machines priced over 100 M€.

A different long-standing strategy for nanofabrication has been the use of scanning probes, where a sharp tip interacts with-, and modifies the surface. With the capability of patterning with single atom resolution, scanning probe lithography (SPL) has resulted in some of the most well-known images in modern physics, such as the atomic IBM logo, and the quantum corral [1, 2]. A major drawback however has been the throughput, which is rather low for SPL in ultra high vacuum (UHV), being around ~ 15 orders of magnitude slower than optical lithography systems. Yet, recent advances in ambient SPL have shown greatly enhanced writing speeds ($\sim$ 10 orders of magnitude), making it competitive for some applications [3]. In fact, commercial SPL systems such as the NanoFrazor (SwissLitho, now Heidelberg) with single-digit nanoscale resolution have recently become available. An additional boost in throughput, as was also pursued in IBM's Millipede project, can be achieved by mass-parallelization of simultaneously writing tips [4]. As such, SPL is rapidly progressing towards the required writing speed for more widespread application.

A distinct advantage of SPL over optical lithography is the wide variety of available tip-sample interactions. A subset of SPL techniques therefore allows for additive manufacturing, which is recently getting more attention at the nanoscale [5]. Combined with the spatial freedom of a scanning probe, this ultimately allows for the direct free-form writing of arbitrary 3D structures [6], enabling the fabrication of novel device architectures which can for example provide enhanced mechanical [7], optical [8], and chemical [9] properties.

With this goal of free form additive manufacturing in mind, an attractive option is the use of localized electrocrystallization. Electrochemical deposition is typically done in solution, thus

avoiding the need for UHV. Furthermore, as growth is controlled by a potential and often done near equilibrium, this can lead to high quality of the deposited metals or semiconductors, without the need for high temperatures. Importantly for 3D structures, electrochemical deposition can be done in a continuous fashion. As such, local electrodeposition has also recently resulted in commercialization of a scanning probe system, with the FluidFM (Cytosurge) currently printing at submicron scales.
Confining local electrocrystallization further to scales below 100 nm has proven difficult however. While the electrochemical deposition process is governed by the interface, further confinement often involves bringing the probe very close to the substrate. The resulting confined system is influenced by interactions with the probe and can give rise to new effects, as the dynamics of the interfacial region are relatively unknown at the molecular level.
Fundamentally, localizing electrochemistry is about control over the behavior of ions at or near the electrified interface. This thesis therefore explores ion dynamics at the nanoscale. We do this primarily for the purpose of scanning probe nanofabrication, but also with the aim of considering the inverse problem, using confined electrocrystallization to shed light on the local processes at the interface.
This first chapter introduces some of the concepts regarding electrocrystallization and the solid liquid interface, in sections 1-1, and 1-2. Section 1-3 reviews the history of electrochemical SPL. We then present an estimate for the achievable degree of localization in section 1-4, which will serve as an initial hypothesis for the rest of this thesis, of which the outline is provided at the end of this chapter.

1-1 Electrocrystallization

Electrochemical equilibrium

With the aim of controlling electrodeposition at the nanoscale, we first consider the conditions under which electrochemical deposition occurs. As the name implies, electrochemical reactions are mainly controlled by an electrical potential. Therefore, the chemical potential of a species j, is often described in terms of the internal chemical potential μ_j and a term for the electric potential ϕ, giving the so-called electrochemical potential $\overline{\mu_j}$,

$$\overline{\mu}_j = \mu_j + z_j F \phi \tag{1-1}$$

where z_j is the charge number and F the Faraday constant. When considering a system with multiple phases however, such as a metal electrode in solution, the electric potential in the two phases is typically not the same. A nice illustration is given in the book by Staikov [10] for a metal electrode immersed in an electrolyte with its metal ions A^{z+}. In equilibrium, the electrochemical potential of both the solution and the crystal have to be equal ($\overline{\mu}_{A,s} = \overline{\mu}_{A,c}$). With the internal chemical potential μ_j defined analogously to that for an ideal gas ($\mu_j = \mu_j^0 + RT\ ln(\frac{P_j}{P_j^0})$, with μ_j^0 the standard chemical potential $P^{(0)}$ the

(standard) pressure, R the gas constant, and T the temperature) this yields,

$$\begin{aligned} \overline{\mu}_{A,s} &= \overline{\mu}_{A,c} \\ \mu^0_{A,s} + RT\ln(a_{A,s}) + z_A F\phi_s &= \mu^0_{A,c} + z_A F\phi_c \\ \phi_c - \phi_s &= \frac{\Delta\mu^0}{Fz_A} + \frac{RT}{Fz_A}\ln(a_{A,s}) \end{aligned} \tag{1-2}$$

With $\Delta\mu^0 = \mu^0_{A,s} - \mu^0_{A,c}$, and where the activity a is typically equal to the concentration c_A, in dilute electrolytes[1]. Equation 1-2 is just a form of the Nernst equation, and has the interesting result that the immersed electrode in equilibrium will set up an electric potential difference, $\phi_c - \phi_s = E_{eq}$, with the solution, which depends on the concentration of ions in the electrolyte.

This is illustrated in Fig. 1-1, which shows the potential difference between the electrode and the solution as a function of the ion activity, yielding an equilibrium curve (black solid line). This line separates two regimes, where the system is in electrochemical *undersaturation* ($\overline{\mu}_{A,s} < \overline{\mu}_{A,c}$), or *supersaturation* ($\overline{\mu}_{A,s} > \overline{\mu}_{A,c}$), depending on whether the system is above or below the equilibrium line, respectively. In either case, there will be an electron flow to restore equilibrium; in supersaturation through the oxidation of the crystal (negatively charging the electrode), or in undersaturation through the reduction of metal ions (negatively charging the solution). From the figure it now becomes apparent that there are 2 main ways to achieve supersaturation, and subsequent metal ion reduction, as illustrated by the dashed arrows; i) by lowering the potential difference $\phi_c - \phi_s$, and ii) by increasing the ion activity, e.g. through increasing the ion concentration. In order to localize electrochemical deposition for scanning probe lithography, one would therefore require an inhomogenous profile of either of these two quantities across the substrate-solution interface so that supersaturation is achieved only close to the tip.

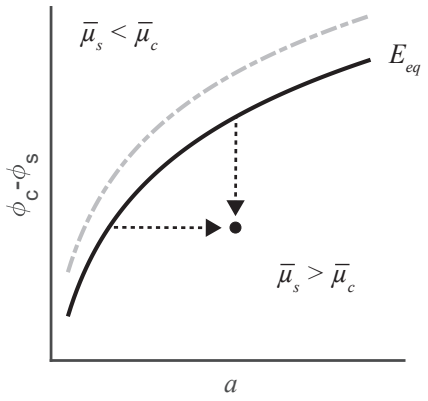

Figure 1-1: Schematic depiction of the equilibrium potential, $\phi_c - \phi_s = \mathrm{E}_{eq}$ as a function of ion activity for a system with metal ions and an electrode of the same species (black solid line), or a foreign substrate (grey dashed line). The line separates a region of supersaturation (indicated by the black dot), where metal ions reduce on the substrate, and undersaturation, where the electrode oxidizes. Adapted from reference [10].

[1]The concentration is corrected by a coefficient to yield the activity, capturing ion-ion and ion-solvent interactions [11]. For the crystal the activity is set to 1, which is why the natural logarithm does not appear in the expression for its electrochemical potential.

An interesting consequence of the thermodynamic description above is the phenomenon of underpotential deposition [12, 13]. In the previous example, where the metal ions are of the same species as the electrode, $\Delta\mu^0$ in equation 1-1 is taken to be constant as ions move from or onto the electrode. More often, deposition will take place on a foreign substrate however. In that case it is easy to imagine that $\Delta\mu^0$ takes a different value, as the difference in standard chemical potentials of the solution and the crystal is not the same, which shifts the equilibrium curve. If this difference in chemical potential is larger for the foreign substrate than it would be for an electrode of the same material, the equilibrium curve for the metal ions with respect to the foreign substrate moves up in Fig. 1-1, as is illustrated by the grey dashed line. At electrode potentials between the 2 curves deposition is only possible on the foreign substrate and not on the native metal. This then opens a window of $\phi_c - \phi_s$ potentials in which deposition will occur as a single layer, as to cover the electrode with the corresponding metal after which equilibrium is attained.

Kinetically controlled growth

In electrochemical deposition the system is typically continuously driven out of equilibrium, e.g. by applying a potential difference between the substrate and the liquid. As outlined in the previous section, thermodynamics then tells us that this will drive metal reduction, but the deposition *rate* is determined by the reaction kinetics, which can vary dramatically (electrochemical rate constants can vary by over 10 orders of magnitude [14]).
The current density resulting from metal reduction (or oxidation), which is also called the Faradaic current for electrochemical charge transfer at an electrode, typically depends exponentially on the applied potential, given by the well-known Butler-Volmer equation. It expresses the total electrochemical current as a sum of the reduction and the oxidation reaction, that both depend exponentially on the potential difference with equilibrium,

$$J_{BV} = J_0 * (e^{\frac{(1-\alpha)nF}{RT}\eta} - e^{\frac{-\alpha nF}{RT}\eta}) \tag{1-3}$$

Here T, F, and R are the temperature, Faraday-, and gas constant, respectively, n is the number of electrons in the reaction, and η the overpotential, or potential difference with respect to the equilibrium $E - E_{eq}$. J_0 is the exchange current density, and is a key parameter in determining the rate of the reaction at a certain overpotential. Considering the temperature dependence of equation 1-1, it makes sense that the equilibrium curve in Fig. 1-1 denotes a dynamic equilibrium for a system at finite temperature. As the electrochemical potential is the same in both phases, both oxidation and reduction reaction occur continuously as electrons are transferred across the interface in both directions through thermal fluctuations. As there is no *net* electron transfer across the solid-liquid interface along the curve, the rates of both reactions have to balance each other at equilibrium, yielding the exchange current. As such, the exchange current is a metric for how kinetically easy the reaction is.
Finally, α denotes the transfer coefficient, prescribing the symmetry of the forward and backward electron transfer. While their rates are equal at equilibrium, these do not have to change in the same way when the system is not. The transfer coefficient was introduced to capture the difference in the change of the energy barrier away from equilibrium, and can for example yield an asymmetric $J - \eta$ curve as will be illustrated in section 1-4.
Besides potential and ion activity, kinetics or exchange rate offer another way of local control

over the reaction. Here we can imagine certain locations on the substrate that provide a higher reaction rate, so that deposition will occur faster/only at those locations. An example of this is the use of step edges for preferential deposition, which has been used for the electrochemical deposition of horizontal nanowires [15].

A relevant example of different electrochemical rates for this thesis is that of copper deposition on a gold substrate from an aqueous solution containing sulphates. This is illustrated in Fig. 1-2a, showing a crystalline copper particle nucleated by means of a potential pulse. The AFM topography image (left) is transformed to represent the inclination of the topography with respect to the substrate (right), so that a constant slope is represented by the same color. The particle is highly faceted, represented by the equal-angle planes. Based on the shape of these facets and their orientation with respect to each other and the substrate, we can identify two types of facets with the {111} and {100} crystal orientation of the fcc crystal, slightly tilted with respect to a {110} growth direction.[2] [16, 17]. This faceting is typically a result of the different crystal planes having a different growth rate, where the slower growth directions result in exposed facets.

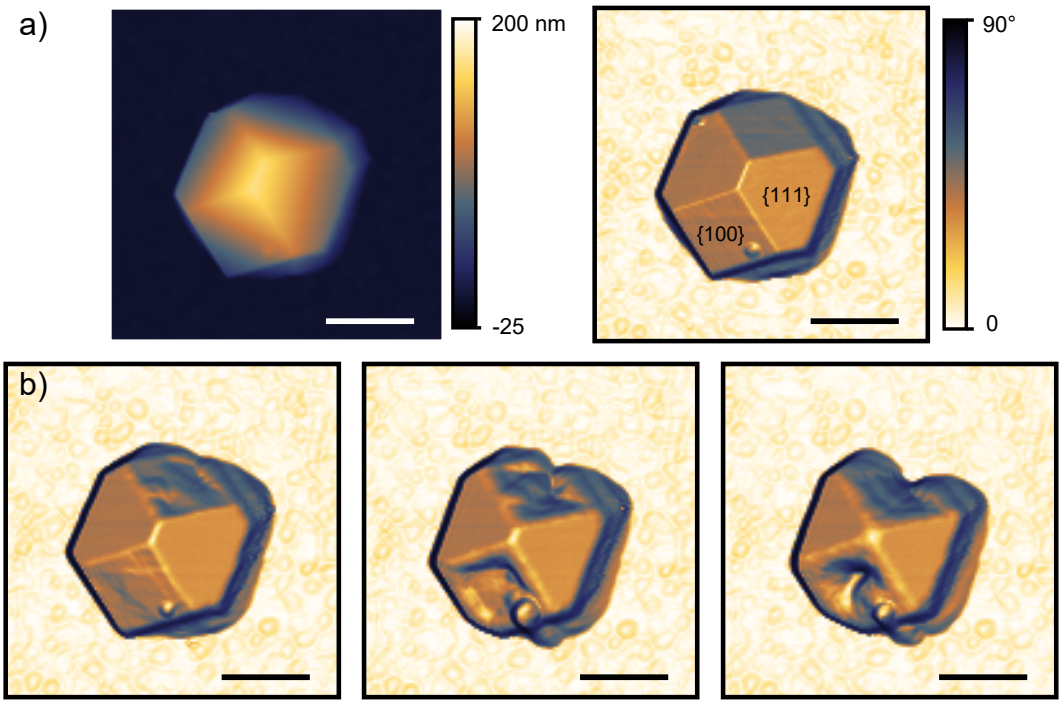

Figure 1-2: a) AFM topography (left) and inclination (right) image of an electrodeposited copper crystal. The {111} and {100} oriented facets are indicated. **b)** Subsequent inclination images as the crystal dissolves preferentially on certain facets. The time between images is ∼1 minute. The scale bar is 200 nm in all images.

[2] the {111} and $\{\bar{1}\bar{1}1\}$ facets have an angle of 70° (30°+ 40°), and the {100} and $\{\bar{1}00\}$ facets have an angle of 90° (40°+ 50°), with respect to the base.

While the faceted nature of the deposit does not have to be a direct consequence of different electrochemical rates, as growth can also occur through other processes such as surface diffusion [18], the different rates are seen more clearly in the time evolution of the island as it dissolves. Fig. 1-2b shows AFM inclination images as the particle dissolves over time, where the {100} planes do so much faster than the {111} facets in this case.
In this example, the growth/dissolution kinetics are generally governed by the surface energy of the different crystallographic orientations [19], with high energy planes growing/dissolving the fastest. Fig. 1-2 therefore implies that the order of surface energies for this system is $\{111\} < \{100\} < \{110\}$, in accordance with literature [20]. Additionally, these electrochemical rates can be affected by the specific adsorption of ions to certain planes, where in our example sulphates are known to adsorb to Cu{111} [21]. Consideration of the electrolyte and associated passivation of certain crystal orientations is therefore one of the examples in controlling the growth rates of different facets, providing fine control over the resulting crystal morphology [22–24].

1-2 The Solid-liquid Interface

The previous section considered electrochemical growth through charge transfer across the solid-liquid interface, where this charge transfer is described by the Butler-Volmer model as a function a potential difference between the solid and the liquid. As the charge transfer across the interface is ultimately an electron tunneling process this implies that the potential drop in the liquid has to occur very close (nanometers) to the interface. While a rigorous description of the solid-liquid interface is beyond the scope of this chapter, this section introduces some of the relevant length,- and time scales associated with the potential distribution at the interface.

The Electrical Double Layer

Solutions with a dissolved electrolyte contain free charge carriers in the form of mobile ions. In fact, imagining the simple case of a dilute 1:1 electrolyte where both ions have the same mobility, the liquid can be considered somewhat 'metallic' as ions will redistribute to screen internal electric fields, and excess charge will be located at the boundary of the solution. For example when placing a polarized electrode in the solution (which we take here to be 'blocking', or without Faradaic currents), the electric field will be compensated by ions close to the electrode surface, so that the potential difference naturally occurs near the interface. These spatially separated charge distributions on the electrode and in the solution are referred to as the Electrical Double Layer (EDL). The length scale associated with this electrical screening is given by the Debye screening length,

$$\lambda_D = \sqrt{\frac{\epsilon\epsilon_0 k_B T}{2z^2 e^2 N_a C}} \tag{1-4}$$

Where ϵ and ϵ_0 are the relative and vacuum permittivity, respectively, k_b is the Boltzmann constant, T is the temperature, z is the charge number, e the elementary charge, N_a the

Avogadro constant, and C the concentration of the electrolyte. As $\lambda_D \propto \sqrt{\frac{1}{C}}$, the screening length can vary by ~ 3 orders of magnitude for different concentrations, ranging from angstroms at C = 1 M to a few hundred nanometers at C = $1e^{-6}$ M.
The potential extending into the liquid will then typically have an exponential profile with the decay length, or distance for the e^{-1} value of the potential, given by λ_D. The exponential shape is determined by a dynamic equilibrium of electrostatic interactions between ions and the charged surface, and randomization through thermal processes. The screening of charges on an electrode surface therefore results in a somewhat loosely bound region of an increased (decreased) concentration of counterions (coions) near the surface, which is known as the diffuse,- or Gouy-Chapman layer. [14]
The diffuse layer is only one part of the general description of the structure of the interface, which is complimented by an additional layer, or Stern layer, accounting for specific adsorption of ions at the electrode. Furthermore, the potential profile in the diffuse layer is exponential only in the limit of low potential differences between the electrode and the liquid ($V \ll \frac{k_b T}{ze} \sim 25mV$). As such, the actual potential profile deviates from the purely exponential decay, through e.g. specific adsorption, high applied potentials, and/or steric effects [14, 25].
It should be stressed that while we discuss the screening length in terms of the interface, λ_D is not related to the electrode and is rather a material property of the electrolyte. It is however the relevant length scale for the extent of the electric field into the solution and therefore the only region in the electrolyte with a non-zero charge density.[3]

Charging the interface

With the screening of a surface charge on an electrode resulting in a spatially separated charge distribution in the electrolyte, the interface is often modeled as a capacitor. As such, upon the application of a potential difference between two electrodes the interface charges over time as the ions redistribute in a process that is not at all trivial, even at low potentials (below the thermal voltage, or ≤ 25 mV) [26]. The time scale over which the charging occurs is dependent on λ_D, as it sets the distance over which ions have to migrate towards the electrode. For example the time it takes for an ion to diffuse over a distance λ_D, the Debye time τ_D, is given by $\tau_D = \lambda_D^2/D$, with D the diffusion coefficient. This is typically a very fast process and therefore the initial part of EDL buildup, as the screening length is in the order of nanometers. Full charging takes longer however, as ions need to be supplied from the bulk through conduction. The associated time scale τ_C is given by $\tau_C = \lambda_D L/(2D)$, with L the electrode separation, and also emerges as the RC time when considering the interface as a capacitor charged through a solution resistance [27]. It is worth noting that this time scale for charging of the interface is dependent on the electrode separation, as is also stated in reference [26] by emphasizing "the fundamental coupling of double-layer charging to bulk transport in finite polarizable systems". Finally, at much longer times τ_L, the ion distribution at the interface equilibrates with the bulk concentration through diffusion at times $\tau_L = (L/2)^2/D$. As a result, dynamic equilibrium (or steady state) is reached when the electric field in the bulk solution vanishes and the charge at the electrodes is fully screened. This charging process in the simple case of an instantaneously applied potential between two electrodes is shown schematically in Fig. 1-3.

[3] This does not have to be so in more complex cases, e.g. systems that display liquid junction potentials through ion mobility differences.

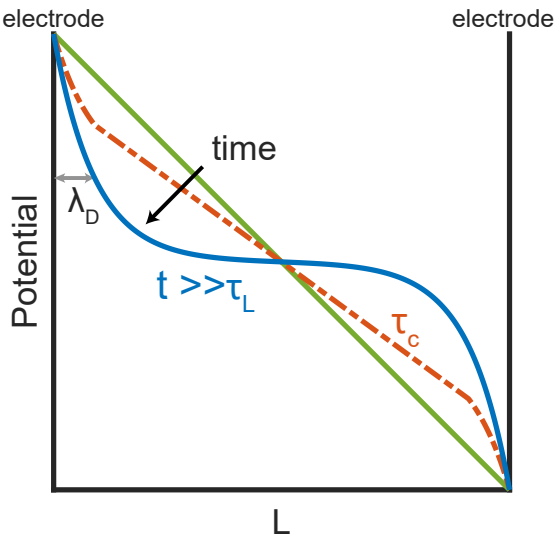

Figure 1-3: Schematic representation of the charging dynamics for 2 electrodes when a potential is applied at t = 0 (green solid line). After the RC time τ_C the interface is partially charged, with the remaining electric field further driving ion migration (red dash dotted line). At long times the system equilibrates with 2 diffuse layers, confined to the screening length λ_D (blue solid line). The Stern layer is disregarded in this image. The figure is based on reference [27].

1-3 Electrochemical Scanning Probe NanoLithography

In section 1-1 we defined three main ways of controlling electrochemical reactions; i) through the applied potential, ii) a change in activity, and iii) a difference in the reaction rate. This section will briefly look at methods that have been used for localization in prior work on electrochemical scanning probe lithography (EC-SPL), which can often be interpreted in terms of these mechanisms. For clarity, the material and typical dimensions (lateral dimension x height), will be denoted for the works concerning deposition.

One of the early methods demonstrating electrochemical deposition at the nanoscale was through the creation of local defects on an highly oriented pyrolytic graphite (HOPG) substrate with an STM tip. Following the voltage induced pitting of the substrate in a silver plating solution, silver dots would deposit locally as the defect acted as nucleation center [28, 29] (Ag, ∼20x7 nm). In a similar fashion of locally enhancing the deposition rate, copper structures have been deposited by using an AFM to mechanically remove passivating layers at the substrate, after which deposition occurs locally [30–32] (Cu, < 100x100 nm).

A conceptually different method was developed by Kolb et al [33, 34]. In this case metal clusters were transferred to the substrate through mechanical interaction by first depositing on the STM tip and then bringing the tip into contact with the substrate. This 'jump-to-contact' method was also demonstrated to be fast (50 clusters/second) and able to make large patterns [35] (Cu, 4x1 nm).

A rather elegant adaptation of the process of depositing on the tip itself was developed by Schindler et al. [36–39]. Initial loading of the tip is followed by 'burst-dissolution' when reversing the potential, while keeping the substrate potential just positive of the deposition

potential. The dissolution creates a high concentration of metal ions underneath the tip, and locally shifts the equilibrium potential, following the explanation in section 1-1. Deposition is then enabled locally, as the same substrate potential is at a slight overpotential for the reduction reaction where the concentration is raised, but is at equilibrium for the bulk (Co, Pb, ∼15x5 nm).[4]

Along this line of deposition through an inhomogenous concentration profile is the use of confined systems, or local delivery, albeit through a very different mechanism than a shift in the Nernst potential. Confined electrochemical oxidation by means of a water meniscus forming between the tip and the substrate has been around since the early days of SPL [41], but has been adapted to direct electroplating by the group of Yu [42]. They used a probe that consists of a nanopipette, pulled from a glass capillary, and filled with the plating solution. After bringing the pipette into (electrical) contact with the substrate through the droplet sticking out of the nozzle, deposition is confined to the area of the meniscus. The meniscus can be steered with the probe, tracking the deposit, and allowing for structures with any aspect ratio. This technique has been used succesfully for multiple materials [43, 44], 3D shapes [45], parallel layer-by-layer deposition [46], and integrated with a tuning fork feedback system [47] (Cu, Pt, 150 nm diameter). In our lab, we have also used this scheme to print copper and indium micropillars (Fig. 1-4). More recently, a similar strategy of local delivery has been used inside an electrolyte bath without the metal ion, by injecting ions through the nozzle [48] (Cu, 500 nm) and has even been integrated into AFM systems through hollow cantilevers, also demonstrating layer-by-layer printing [6, 49, 50] (Cu ∼, 800 nm diameter).

While local delivery strategies as described above are capable of printing complex 3D structures, the smallest features that can be printed are typically 1 to 2 orders of magnitude larger than that of the aforementioned EC-SPL techniques, mainly due to limitations on the nozzle size and diffusion/ejection profiles [5, 51].

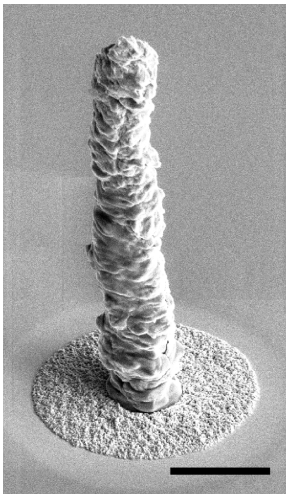

Figure 1-4: SEM image of an indium pillar printed by meniscus confined electrodeposition using a glass pipette. The scale bar is 5 μm.

[4]Getting ahead of an outlook, an approach that I would find interesting and has not been reported in literature would be the use a conducting probe conformally coated by a dielectric. When polarizing the core and using a proper dielectric cladding, this should result in a high concentration of ions near the tip that screens the field, comparable to ref [40]. This 'concentration-probe' could then also be used to locally shift the Nernst potential, analogous to Schindler's approach.

A simple approach of direct electrochemical writing by means of local overpotentials has proven difficult to implement at the nanoscale however. As a polarized probe is placed close to the substrate, the electric field can become very large, which has been used in high-field SPL techniques that use electron field emission or field-induced decomposition of precursors for local deposition [52–56] (Au, 15x3 nm, Ni, 20x5 nm, Ge, 70x5 nm).
In electrochemical systems, electric fields are typically screened near the interface due to freely moving ions, as discussed in the previous section. However, if the tip-substrate distance is smaller than the screening length, electrochemical potentials become rather ill-defined. It is then not straightforward to explain some of the local electrochemistry observed in SPL literature for both etching and deposition. This has been attributed to electric fields due to overlapping double layers [57–59], electrostatic repulsion of ions from the gap and/or shielding by the tip [60], or other mass transport limitations [61] (Cu, 8x1 nm). Furthermore, a locally increased concentration due to dissolution from the tip can not always be excluded, especially for some works employing a more complex polarization routine than a single potential difference between the tip and the substrate [62, 63] (Pb, 5x2 nm, Ag, 5x2 nm).
A more controlled technique in terms of defined local electrochemical potentials was developed by Schuster et al. By applying short (ns) pulses to a tip electrode, migration is highest close to the probe due to a short tip-substrate path having a low resistance, so that the interface charges more rapidly locally. This mechanism is described in terms of an equivalent RC-model for the electrochemical system and is quite successful in predicting the localized etching of metals [64–67] down to 200 nm wide lines [68], but does not seem to have the same accuracy for deposition [61], possibly due to the considerations for the electrochemical potential distribution mentioned above.
Finally, perhaps the most general form of direct electrochemical localization was shown using the scanning electrochemical miscroscope (SECM), by simply applying a potential difference between the tip and the substrate, originally in a conducting polymer electrolyte [69] (Ag, Au, 200 nm wide lines), but also using aqueous electrolytes [70–72]. Noteworthy in this context is the strategy employed by the group of Heinze, called the 'chemical lense' [73–76]. In this case the metal ion complexes in the electrolyte, and the electrode tip produces a decomplexing species. As a consequence, metal ions are freed near the tip, after which the ions can be reduced at the substrate. As the complexing agent diffuses towards the electrode, and re-complexes the metal ion, the writing resolution actually improves as the probe is positioned further from the substrate. Using this mechanism, the chemical lense is one of the few schemes that can decidedly write features smaller than the electrode size (10 μm wide, Ag).
To summarize; even when narrowing the scope of SPL to electrochemical techniques, quite a few approaches have been developed in the last decades. Continuous direct writing at the nanoscale using a potential difference remains elusive however, with one of the earliest works being a rare example [77] (Au, 300x100 nm). The next section will attempt to outline the requirements for confining an electrochemical reaction, using an electric circuit model similar to the RC circuit used to describe the local charging with ultrafast pulses.

1-4 Direct current (DC) nanoscale electrochemistry

As a starting point for the rest of this thesis, we estimate the degree of localization that can be achieved with an AFM tip, based on a simple electrical circuit model of the system under DC operation. Localized deposition by simply positioning a metal wire electrode closely above a conducting substrate and applying a large bias potential has been demonstrated quite successfully in micro-sized systems. This was pioneered by Madden and Hunter [78], showing the free-form deposition of Ni, and has since been often demonstrated using Cu structures [79,80]. In these cases, localization is explained by means of the high electric field strength when the probe is placed close to the sample, resulting in an image charge on the substrate and enhancing mass transport through migration [81, 82]. Potential (and growth) profiles are then based on Laplace's equation for the electric field in the absence of free charge, $\nabla^2\phi = 0$.
Considering the discussion in section 1-2 this explanation should be used with caution however when the electrode separation is much larger than the screening length, as the electrolyte is filled with free charge carriers in the form of ions and potentials applied to the electrode are screened close to the surface by the diffuse layer. In fact, it is charge that passes through the interface that creates potential differences and enhanced migration in the solution, rather than the charge density on the electrode.
A different approach is to consider an electrical circuit for the Faradaic current flowing through the electrode, rather than a model based on electrostatics. The condition that has been formulated for localized deposition and 3D growth from efforts in the field of maskless electroplating is that the electrolyte resistance R_{el} has to be much larger than that for charge transfer across the electrode R_{CT} [83]. This can be understood by considering a simplified Randles circuit for the electrochemical system as shown in Fig. 1-5a. Here the solution resistance is modeled by a resistor R_{el}, which depends on the resistivity ρ of the solution and the tip-substrate distance, d. The interface consists of a capacitor for the electrical double layer parallel to a voltage dependent charge transfer resistance R_{CT}. Any effects related to mass transfer are neglected here (i.e. we assume that the concentration near the interface is the same as in the bulk, $c_{interface} = c_{bulk}$)[5]. Under DC operation the double layer capacitance can be disregarded, so that the circuit reduces to two resistors in series. We now consider that the system of a probe above a homogeneous substrate consists of many of such two-resistor circuits in parallel. It then becomes apparent that the distance dependent R_{el} is the only way to create an inhomogeneous deposition current along parallel current paths of different lengths from the probe to the substrate, as R_{CT} is the same over the whole substrate. This then leads to the same condition $R_{el} \gg R_{CT}$ for 3D growth, as stated above.
This principle has been identified as a limiting factor in the direct fabrication of oxide structures in scanning probe lithography as the resistance of the growing phase quickly becomes larger than that of the electrolyte, even in the case of ultrapure water, forcing the use of meniscus-confined strategies [83–85]. However, while a large resistance is not expected to be an issue for the growth of metals [10], the direct electrochemical writing of nanostructures by means of DC resistance-based localization has been remarkably absent in literature [3,86,87].

[5]Some effects related to mass transport could otherwise be captured in an additional Warburg impedance in series with R_{CT} [14]

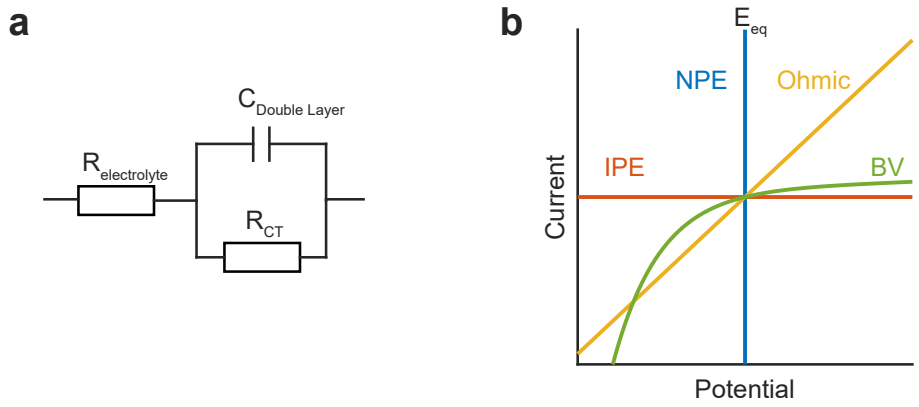

Figure 1-5: **a)** Simplified Randles circuit, where the interface is represented by the double layer capacitance in parallel with a charge transfer resistance. **b)** Polarization curves for an ideally polarizable electrode (IPE, red), non-polarizable electrode (NPE, blue), regular Ohmic resistance (yellow), and generalized charge transfer based on Butler-Volmer kinetics (green) with $J_0 = 0.05\ \frac{mA}{cm^2}$ and $\alpha = 0.9$.

Before focusing on the conditions required for the localized deposition and 3D growth of metal (nano)structures it is useful to first consider some I-V, or polarization, curves of electrochemical elements, as shown in Fig. 1-5b. These curves can also be interpreted as the potential difference required over the element for a certain current to flow. The extreme cases are the Ideally Polarizable Electrode (IPE) and Non Polarizable Electrode (NPE) [14]. The IPE corresponds to a flat line in the polarization curve, meaning that it can sustain an arbitrary potential difference without allowing a change in the amount of current. The NPE, as its counterpart, will always have a constant potential regardless of the amount of current flowing through. It should be noted that this non polarizability is what is desired in a reference electrode, as the electrode will have a constant potential difference with the solution, allowing measurements with respect to that value.
Actual polarization curves will always show voltage dependent behavior in between these extremes, but can have similar characteristics on a certain potential range. To illustrate this, Fig. 1-5b further shows a linear relation as expected from a regular Ohmic resistor, and that corresponding to the Butler-Volmer (BV) equation from section 1-1 describing the electrochemical current across the interface. The shape of the BV curve in Fig. 1-5b is of particular interest here, where J_0 and α are chosen to make the curve asymmetric. As such, the resulting curve is similar to an IPE at the displayed potentials positive of the equilibrium potential E_{eq}, but resembling an NPE for higher overpotentials negative of E_{eq} as the current increases exponentially.

Considering the aforementioned circuit of Fig. 1-5a consisting of two resistors, we can express the applied potential as the sum of the potentials over the solution-, and interface resistance. We use this as a model for a simple 2-electrode system consisting of an AFM tip above a substrate, where we take the tip to be non-polarizable at 0 V,

$$V_{applied} = V_{electrolyte} + V_{interface} + V_{tip} = J_{BV}(V_{interface})\rho d + V_{interface} \tag{1-5}$$

Substituting equation 1-3 for a reaction with $E_{eq} = 0$, so that $\eta = V_{interface}$, equation 1-5 can then be solved for the potential over the interface as a function of the applied potential. We

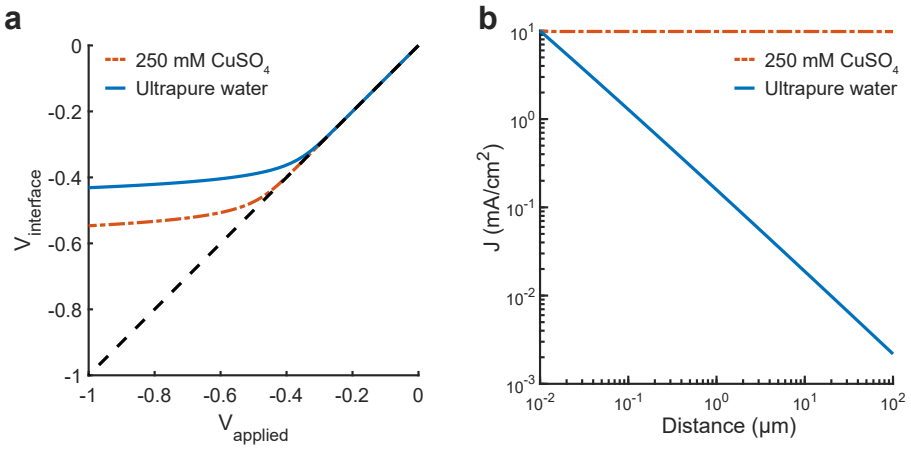

Figure 1-6: a) The resulting potential across the interface as a function of applied potential when the tip is $10\,nm$ from the surface. The red line is obtained using the resisitivity for 250 mM $CuSO_4$ ($0.6\ \Omega \cdot cm$) and the blue line for ultrapure water ($18\ M\Omega \cdot cm$). The black dashed curve is the line $V_{applied} = V_{interface}$, indicating no potential drop in the electrolyte (i.e. $R_{el} \ll R_{CT}$) **b)** The calculated current density through the interface as a function of distance for the same electrolytes, showing that the growth rate is constant for all distances in the high concentration electrolyte, but can be localized for highly resistive solutions. The applied potentials are set to to have a current density of 10 $\frac{mA}{cm^2}$ at a distance of $10\,nm$.

apply this now to investigate the electrodeposition of copper as a model system.
The result for $V_{interface}$ as a function of $V_{applied}$ is shown in Fig. 1-6a for an electrolyte based on 250 mM $CuSO_4$ (red dash-dotted line, $\rho = 0.6\,\Omega \cdot cm$ [88]) and ultrapure water (blue solid line, $\rho = 18\,M\Omega \cdot cm$) with the tip-sample distance set to 10 nm, and where negative $V_{applied}$ are used to reflect that the metal deposition is a reduction process.[6] The $V_{interface}$-$V_{applied}$ curve shown in Fig. 1-6a has 2 notable features; Firstly, while the whole applied potential drops at the interface for low $V_{applied}$, indicated by the dashed line $V_{applied} = V_{interface}$, the interface becomes close to non-polarizable for higher values, analogous to Fig. 1-5b. As any additional potential now mainly falls in the electrolyte this is essentially the condition $R_{el} \gg R_{CT}$ required for 3D growth.
Secondly, this behavior is seen for both cases but does shift to higher overpotentials. This implies that localization is possible for all concentrations, as long as the system is driven hard enough.

To verify the degree of localization, we solve for $V_{interface}$ obtained at different tip-substrate distances and apply this in equation 1-3 to obtain the current density. This yields the distance-dependent current density for a certain driving potential, where the resulting current-distance profile is shown in Fig. 1-6b on a log-log scale. Here, $V_{applied}$ is set to yield a current density of 10 $\frac{mA}{cm^2}$ at a distance of 10 nm. From the figure, it is apparent that the current density drops rapidly as a function of the distance for the resistive electrolyte, but it is virtually constant at higher concentrations. With regards to the result from Fig. 1-6a, this should only mean that the system is not driven hard enough. While this is correct from the model point of

[6] We further use the concentration dependent exchange current density using $J_0 = F * k_0 * c$. This expression is also used to obtain a concentration-independent rate constant $k_0 = 1.25 * 10^{-5} cm/s$ using $J_0 = 0.3\ \frac{mA}{cm^2}$ from reference [89]. This is based mainly on reference [14], even though this assumes the bulk concentration of the reduced and oxidized species to be equal.

view, integrating the current density over a circular area defined by *distance* yields that the total current required to flow through the tip is $\sim$ 30 nA for the dilute case, but is already $\sim$ 0.6 mA for the higher concentration! From these results, it therefore does not seem feasible to drive a nanometric probe at current densities high enough to establish localized growth, if the electrolyte is not highly dilute.[7]

With the distance dependent current density, we are now in the position to predict the degree of localization and shape of the obtained deposit, where we use the highly resistive electrolyte, and take copper growth as a model system for the material parameters. It should be noted that the ionic concentration of ultrapure water is $\sim 10^{-7}M$ through the dissociation of water (pH = 7), so that $\sim \mu M$ concentrations of copper salts are not expected to alter the resistivity much. This is due to the high diffusion coefficient of protons by means of the Grothuss mechanism [90], which is typically larger by an order of magnitude than that of dissolved metal salts. We use a distance dependent growth rate given by,

$$Rate(d) = \frac{A_r}{\rho_m F}\frac{J(d)}{n} \tag{1-6}$$

with A_r the atomic weight (63.546 $\frac{g}{mol}$ for copper), and ρ_m the mass density (8.96 $\frac{g}{cm^3}$ for copper). Fig. 1-7 shows the expected growth profile evolution over time for a flat tip with radius R_{tip} = 25 nm, where the tip is forced to be at 10 nm from the growing structure. The applied potential is set so that the current density at the substrate directly underneath the tip is 10 $\frac{mA}{cm^2}$.

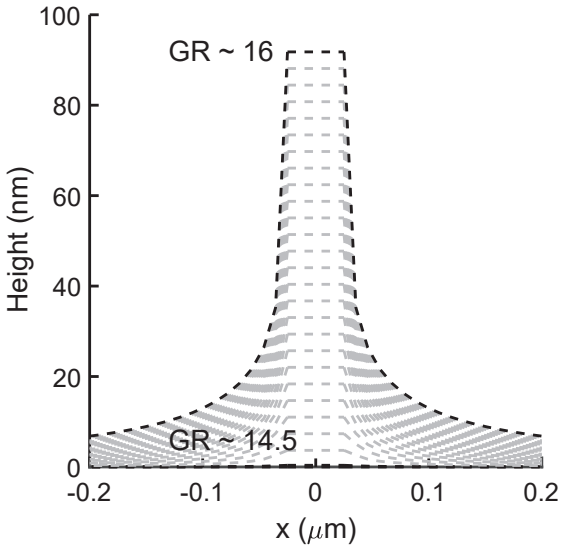

Figure 1-7: The resulting growth profile after 25 s using a flat tip with R_{tip} = 25 nm kept at a height of 10 nm from the growing surface. The applied potential is set as to keep the current underneath the tip at 10 $\frac{mA}{cm^2}$. Since the growth is faster underneath the tip, the growth ratio (GR = $\frac{rate(x=0nm)}{rate(x=200nm)}$ increases over time, as the surface effectively gets further away from the tip position. The grey lines depict the profile every 1 s.

[7] As the slope of the J-distance plot is $\sim$ 1, but the integration area scales with distance^2, the total current actually increases linearly with the substrate area. The numbers in the text are obtained from figure 1-6, i.e. integrated up to a distance of 100 μm

The resulting profile predicts that a high degree of localization can be achieved when the tip is positioned closely to the surface and driven at high currents, resulting in a sharp feature where the half width at half maximum of the deposit extends to < 1 R_{tip} on either side. Furthermore, since growth is accelerated underneath the tip, this results in a self-improvement of the localization over time as the tip retracts, since the constant height of the tip with respect to the growing structure means that the rest of the substrate is effectively moving further away. This is indicated in Fig. 1-7 by the growth ratio, GR, taken as the difference between the rate underneath the tip and at a distance of 200 nm.
Finally, it is interesting to note that the resulting profile in Fig. 1-7 is also Laplace-like, which results directly from the Butler-Volmer equation in this case, rather than from an electrostatic distribution. This is therefore an important result, as the circuit model also predicts a wide deposition 'foot' at the base of the structure, as found experimentally in micro electrochemical deposition [80].

1-5 Outline of the thesis

Armed with this initial hypothesis for localized deposition from highly dilute electrolytes we attempt the use of micromolar concentrations of copper salts for confined electrodeposition in **Chapter 2**. We demonstrate the direct writing of copper nanostructures (< 100 nm) using an atomic force microscope (AFM) and propose a writing mechanism based on periodic charging and discharging of the electrical double layer with the AFM tip.
In **Chapter 3**, we investigate the growth dynamics of the structures deposited in the previous chapter. Due to the difficulties of characterizing these nanostructures, we compare the directed growth with that in a regular electrochemical cell. We find that the tip-mediated writing follows an isotropic growth step after which it is directed out-of-plane, resulting in an increasing aspect ratio.
Chapter 4 explores a different mechanism of nanoscale electrodeposition, by applying short voltage pulses to the tip of a scanning tunneling microscope. Again, we achieve a writing resolution below 100 nm and we investigate the dependence of the achievable localization on the charging dynamics of the interface, based on the diffusion coefficients of ions present. We use a non-aqueous solvent for the deposition, and believe that this is key to achieve nanoscale confinement, as the fast diffusion of protons delocalizes the charging profile in aqueous electrolytes.
In **Chapter 5**, we map electrochemical changes of the surface as a function of the applied potential, through the adhesion between an AFM tip and the surface. We show that this adhesion force depends on the potential of the substrate, and is spatially inhomogeneous. This is linked to the electrochemical state of the surface, where the adhesion denotes the varying energy required for reorganization of the surface at different locations.
Lastly, in **Chapter 6** we turn from current flow through,- to current flow along the interface, and consider a microscopic device characterized by transport through the electrical double layer. Specifically, we experimentally demonstrate the phenomenon of ion current rectification in asymmetric microscopic channels, without chemical modification, and compatible with standard CMOS fabrication techniques.

Chapter 2

Direct nanoscale writing through double layer perturbation

This chapter demonstrates the direct writing of copper nanostructures using an oscillating nano-electrode atomic force microscope tip (AFM). Strikingly we observe that deposition only occurs at very low concentrations, but also requires particular combinations of the AFM operating parameters. Based on our results, we propose a mechanism based on cyclic charging and discharging of the electrical double layer (EDL). The extended screening length and slower charging dynamics in dilute electrolytes allow the nanoelectrode to operate inside, and disturb, the EDL even for large oscillation amplitudes ($\sim$ 100 nm). This can not only be used for controlled additive nano-fabrication but also provides insights into ion behavior and EDL dynamics at the solid-liquid interface. The work in this chapter is reproduced from reference [91] with permission from the Royal Society of Chemistry.

2-1 Introduction

Electrochemical deposition can revolutionize the fabrication of (opto)electronic nanodevices if carefully controlled at the nanoscale. Among its advantages are the relatively small infrastructure costs, low thermal budget and fine dynamic control over reaction kinetics and thermodynamics, which does not exist with any other synthetic method. However, the biggest challenge in integrating electrodeposition and nanotechnology is the controlled down-scaling of chemical reactions down to the nanoscale [92, 93]. This control would provide additional freedom in designing free-form nano-architectures with extraordinary properties and functionalities [5, 7, 8, 51]. One approach to confine growth is by spatially restricting the electrochemical cell or the feeding of precursors, such as in meniscus confined electrodeposition, local dispensing of ions, or electrohydrodynamic jet printing [45, 48, 50, 94–96]. A different strategy is the direct electrochemical writing with small electrodes. Complex 3D structures have been successfully made at the scale of tens to few hundredths of microns by using scanning microelectrodes, where the size of the electrode and its distance to the sample define the fabrication

resolution [47, 82]. At the nanoscale, scanning probe microscopes (SPM) have demonstrated high precision in nanostructuring metal, semiconductor and oxide surfaces under gas or liquid conditions, based on a variety of tip-surface interactions [3,30,32,55]. However, in most cases, growth is restricted to a few nanometers in height (such as clusters). Additive electrochemical nano-fabrication of structures beyond atomic cluster size with scanning probes has been difficult, contrary to what could be expected from conventional electrochemistry. This is due to the fact that when the tip-substrate gap is of the order of nanometers, the reaction dynamics are governed by a complex interplay of electrochemical potential distributions [38], poor communication with the bulk solution, and mass transport limitations preventing ion access into the small gap [60, 72, 97]. In general, effects of the structure and dynamics of the electrical double layer (EDL) at the solid-liquid interface on nanoscale electrochemistry are not fully understood [40,98]. In the past years, several groups have focused on using SPM techniques to probe the solid-liquid interface [99–106], in terms of specific adsorption [107], charge density, and screening [108, 109]. In all these studies, care was taken to ensure minimal perturbation of the EDL by the probing tip. However, it has been suggested that in some cases, the probe may strongly perturb the charge distribution at the interface [57, 60]. Schuster and co-workers demonstrated the etching and deposition of metals with micrometer resolution by locally polarizing the EDL at the water-substrate interface upon the application of a voltage pulse at a micro-electrode [64]. The authors described the reaction confinement by considering a simple RC equivalent circuit, concluding that nanometer resolution would require fs pulses. However, this timescale is much faster than the typical electric double layer dynamics ($\sim$ns-μs) [27]. Interestingly, nanoscale local etching and deposition has been demonstrated with μs pulses to a scanning tunneling microscope (STM) tip [61–63]. In this work, we take advantage of the capabilities of an electrochemical atomic force microscope (EC-AFM) tip to dynamically perturb the EDL in order to control growth at the nanoscale. We achieve this by using a highly dilute electrolyte and a highly asymmetric tip-substrate system (in terms of material and potential). We demonstrate direct electrodeposition of copper on gold, with lateral dimensions down to 50 nanometers and an aspect ratio slightly above 0.5 for a writing speed of 3 nm s^{-1}. We show a critical dependence of the ability to confine growth on the salt concentration, and the dynamics of the tip movement during the writing. We propose a local growth mechanism facilitated by a combination of periodic disruption and build-up of the EDL, followed by forced electrodeposition due to the strong perturbation of the electrochemical potential between the tip and the sample. The ability to control solution-based growth down to the nanoscale can revolutionize nanofabrication, by enabling the manufacturing of combined logical circuits, LEDs, photodetectors and many other (opto)electronic devices on the same platform with nanoscale resolution. Additionally, local deposition with dynamic EC-AFM can be used as an indirect means to probe EDL dynamics in general, which has a strong impact in any electrochemical process such as in batteries, or elecrocatalysis.

2-2 Direct writing of copper nanostructures

We control the local growth of copper on gold by applying a potential difference directly between a Au substrate and an AFM tip in a dilute aqueous electrolyte (1 μM $CuSO_4$). The tip apex, with a nominal radius of 50 nm, is coated with platinum and is the only part of the cantilever that is exposed to the liquid [110]. During writing, the AFM is operated in the PeakForce (PF) tapping mode, where the cantilever is driven by a sinusoidal signal far below

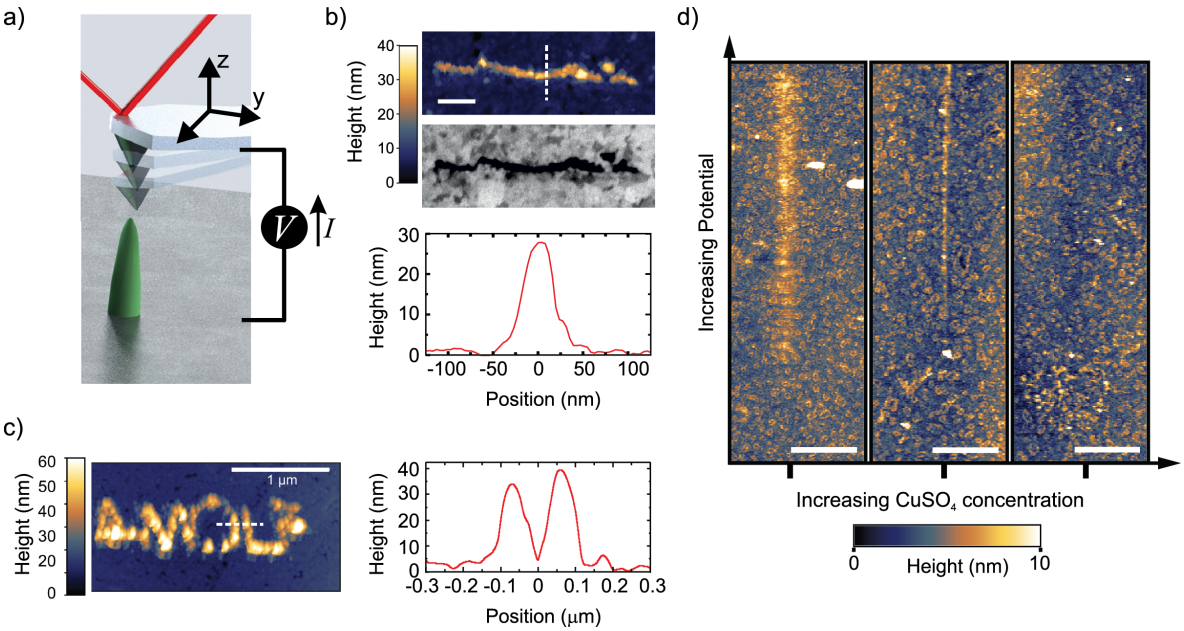

Figure 2-1: Direct writing of copper with dynamic EC-AFM. **a)** Cartoon representing the EC-AFM writing set-up. **b**) Ex situ AFM-topography, cross section height profile, and in-column SEM, of a 1 μm long line deposited in a single EC-AFM pass at 3 nm s^{-1} with an applied potential of 1.7 V. **c)** Ex situ AFM-topography and cross section height profile of the written AMOLF logo, deposited in a consecutive double pass at 30 nm s^{-1} and 3 nm s^{-1} with an applied potential of 1.7 V. The writing in b) and c) were done in 1 μM $CuSO_4$ solutions. The scale bar is 200 nm in b) **d)** In situ AFM topography, after following a 12 μm-long path across the center of each image while ramping the potential from 1 to 2.5 V (in the first two panels) and 1.2 to 2.7 V (in the rightmost panel). Three different concentrations of $CuSO_4$ were used (from left to right: 1, 4 and 12 μM). The deposition disappears by increasing the concentration. The scale bar is 2 μm.

its resonance frequency (2 kHz for the experiments in this chapter). The experimental setup is depicted schematically in 2-1. In this mode, the force exerted by the tip on the sample is used as the feedback signal (3 to 30 nN in our experiments), while the intermittent contact results in minimal lateral forces on the substrate. By moving the tip along a programmed xy trajectory with the potential applied, we demonstrate that arbitrary shapes can be written (Fig. 2-1b and c).

Single lines down to a full width half maximum (FWHM) of ~50 nm and as closely spaced as 125 nm are obtained with aspect ratios above 0.5, as illustrated by the line profiles. It should be noted that the extent of the deposition profile is in the order of the expected tip diameter, which is typically regarded as the lower limit on resolution in most SPM-based nanofabrication [3,87]. The clear Z-contrast of the deposited structure with the gold substrate as obtained from backscattered electrons in a scanning electron microscope (SEM) highlights the chemical nature of the deposited copper wire. This is also found by energy dispersive X-ray (EDX) analysis from a larger structure (SI 2-5). To enable the local writing, however, we find two counterintuitive results that disagree with previously reported micro and nano-SPM based electrochemical deposition mechanisms.
First, we find that the local deposition only occurs when reducing the salt concentration

down to a few μM. The panels in Fig. 2-1d show the topography after the tip is translated over a 12 μm long path with the PF feedback enabled and ramping the voltage ($1 < V < 2.7$ V) along the path. The figure clearly shows the deposition emerging with increasing potential in the case with the lowest ion concentration, which gradually disappears with increasing concentration. In fact, at concentrations above 10 μM, we are unable to observe any growth within our typical AFM scan range ($\sim$15 μm) and parameters (force setpoint of 2-10 nN). While increasing the concentration of $CuSO_4$ should accelerate growth, mainly through facilitating mass transport, it is not in line with our observations. This is therefore a critical result and rules out other known writing mechanisms, such as AFM-induced local depassivation of a metal substrate [30, 32] or electric-field enhanced mass transport [78, 80, 82]. Second, no deposition is observed when the tip is kept at a fixed tip-substrate distance (ranging from 3 to 300 nm). In fact, the rest of the chapter will show that the AFM tip dynamics play a critical role in the direct writing mechanism.

2-3 Influence of electrochemical parameters

First, we investigate the electrochemical nature of the deposition process. The electrochemical behavior of the tip-substrate system is shown in Fig. 2-2a, where no current flows until a minimum potential of around 1.2 V is reached, after which the current increases exponentially. This is consistent with a minimum thermodynamic potential difference between the oxidation of water at the tip and copper reduction at the substrate.
From *ex situ* AFM topography, we determine the deposited volume as a function of the total charge passed through the system, which is controlled by varying either the voltage (1.3 to 2.1 V in steps of 0.1 V, Fig. 2-2b) or writing time by means of the translation speed (3, 10, 30, and 100 nm s^{-1}, Fig. 2-2c).

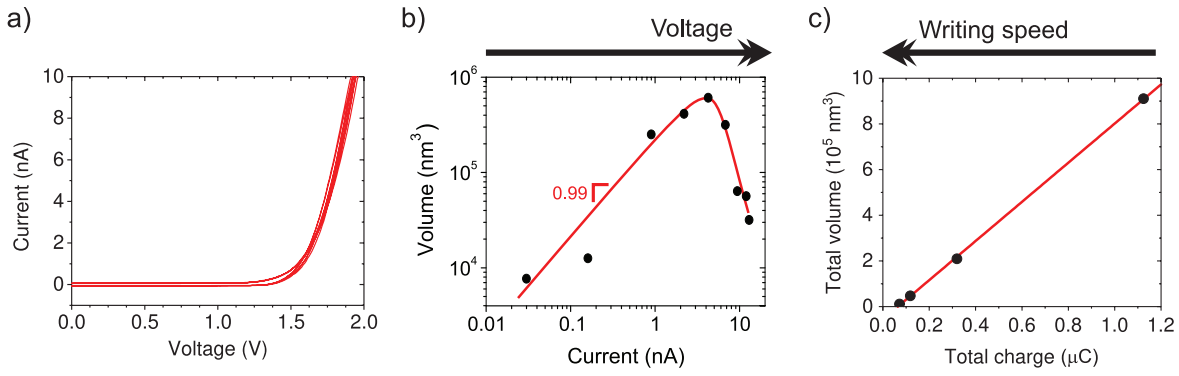

Figure 2-2: Electrochemical nature of the local Cu deposition. **a)** Current-voltage characteristics of the tip-Au substrate two electrode system. At positive bias, current in the electrolyte flows from the tip to the substrate. **b)** Linear scaling of the volume as a function of current in 1000 nm-long lines for a fixed set of AFM parameters. Different currents are obtained by increasing the applied potential. At high potentials/currents the deposition efficiency drops, most likely due to the competing hydrogen evolution reaction. The volume is obtained from ex situ AFM topography. **c)** Volume of 1000 nm-long lines as a function of the total charge transferred for a given voltage and the same PeakForce parameters as in b). The different points are obtained by different writing speeds, from 3 to 100 nm s^{-1}.

The linear dependence of the volume on current supports the electrochemical nature of the process. However, the amount of charge required to obtain an equivalent volume of solid copper from Cu^{2+} is five orders of magnitude smaller than that derived from the measured current. This suggests that large stray currents are present across the substrate that do not result in copper growth, which is not surprising given the large surface area of our substrate electrode ($\sim$5 cm^2). Moreover, Fig. 2-2b shows that the deposition is suppressed at high currents/potentials, most likely due to the competing proton reduction reaction, which leads to a "working" potential window. Actually, the formation of bubbles is observed underneath the tip with an optical microscope at higher current densities (typically $\sim$20 nA).
The additive nature of the fabrication is highlighted by the increase in volume with time when driving the system at a fixed potential. In particular, the volume increases linearly with charge, but only after a certain threshold (Fig. 2-2c). We attribute the presence of a minimum amount of charge required for growth to kinetic limitations of the nucleation.

2-4 Influence of tapping dynamics

In the following, we investigate the impact of AFM tapping parameters on local growth to better understand the mechanism of confined electrochemistry. We adjust the tip position dynamics through the PeakForce amplitude (PFA) and the force setpoint (FS) parameters (Fig. 2-3a). The time-averaged tip-sample distance or gap size (<z>) and time in contact (CT) are estimated from the PFA and FS settings as described in SI 2-6. The effect of the FS on <z> is quite significant. For instance, at the nominal spring constant of 1.5 N m^{-1} of our tips, the maximum gap size is reduced by 20 nm when the FS is increased by 30 nN, a value that may represent a large fraction of the oscillation amplitude.
The influence of the tip dynamics on the local growth is represented by the average maximum height of a line deposited along a 1000 nm-long path as a function of current (Fig. 2-3b). We do not observe a consistent trend in the width of the deposit as a function of the oscillation parameters or the current (SI 2-7). Here, the paths are followed at either 10 or 30 nN, corresponding to dashed and thick lines, respectively, and with three different oscillation amplitudes (15, 50 and 300 nm). The corresponding average gap size and contact time are listed in the table of Fig. 2-3b. Similar to Fig. 2-2b, local growth is favoured within a limited electrochemical window, leading to an optimal drive condition. Surprisingly, the optimal drive strongly depends on the AFM operation parameters. At large oscillation amplitudes, where the tip is above the substrate most of the time, little deposition is seen regardless of the force set point. This reinforces the notion that the process is not primarily driven by surface depassivation from simple mechanical tip-sample interaction. We find that the share of time spent in contact with the sample appears to be a key parameter for determining the optimal driving condition for local growth. This is particularly evident at 15 nm amplitude, where height-current behavior for the two forces is quite different. Rather, the data for 10 nN resemble that of 30 nN with a similar contact time (i.e. amplitude of 50 nm).
In order to further investigate the link between CT and local deposition, we plot the total deposited volume as a function of CT (varied by means of the amplitude) for lines written at a fixed force of 3 nN and various potentials (Fig. 2-3c). The most striking feature in Fig. 2-3c is that growth is absent for all potentials when the contact time is shorter than $\sim$25 μs. The presence of a threshold value for the contact time is in line with the observation that no deposition is obtained with the tip held at a fixed distance above the surface (limit of

zero contact). For times longer than the threshold, the deposited volume generally increases with CT. Interestingly, when writing at low drives (1.5 and 1.6 V), the volume saturates after ∼50 μs. By contrast, at higher drives (1.7 and 1.8 V), the volume increase with CT is less strong and does not saturate within our tested conditions. This is consistent with the data from Fig. 2-3b, where growth at long contact times (dark red solid data) only occurs at high currents. The interplay between potential and contact time with the local deposition efficiency is discussed in the following section, within the framework of the deposition mechanism.

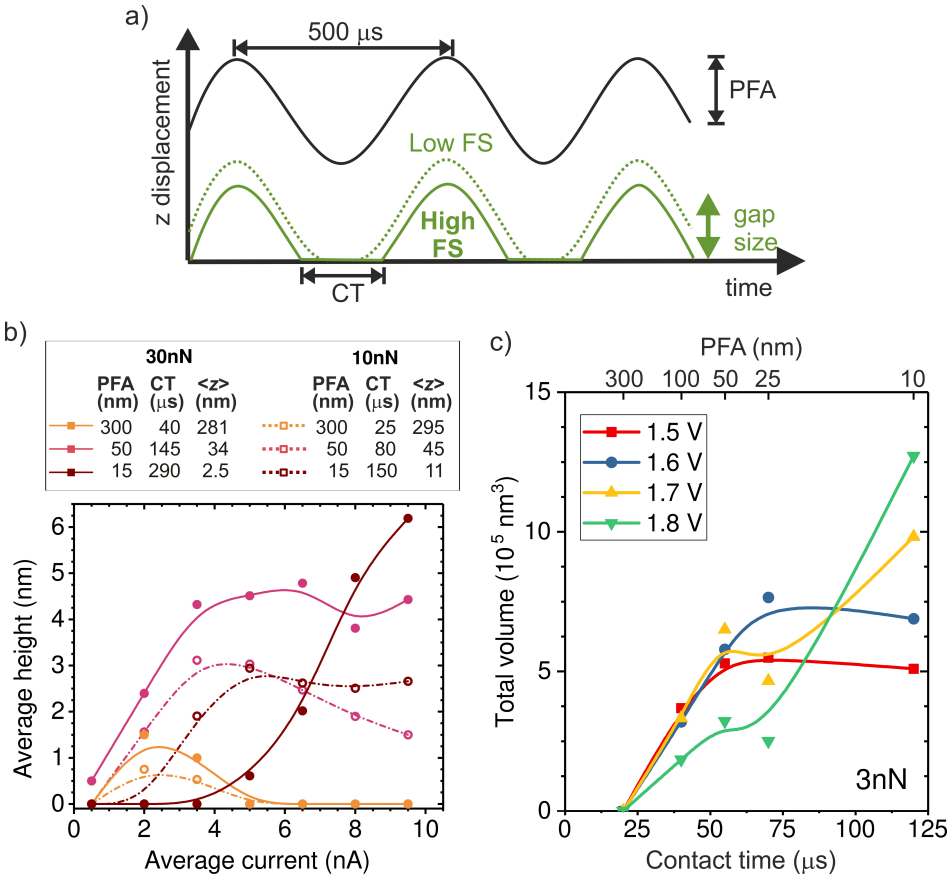

Figure 2-3: Influence of the AFM tip dynamics on the local deposition. **a)** Representation of the tip dynamics over a few tapping cycles. The PeakForce oscillation amplitude (PFA) sets the amplitude of the drive signal (black curve). While the cantilever follows the drive signal, the actual tip position (green curves) and contact time (CT) depend on the force set point (FS) as well. As a result, the center of oscillation moves up and down as a function of both parameters. (b) Height of Cu lines, averaged along a 1000 nm path written at 10 nm s^{-1}, as a function of applied current for different PFA and FS. The estimated CT and average gap size (<z>) during the oscillation are listed above. Both the height of the deposit and the optimal current change as a function of the oscillation parameters. **c)** Total deposited volume in Cu lines written along a 500 nm path as a function of CT, which is controlled by changing the PFA from 10 to 300 nm. All lines are written with the same FS of 3 nN, a translation speed of 10 nm s^{-1} and at fixed bias voltages from 1.5 to 1.8V (average currents of ∼1, 2.5, 4, 6.5 ± 0.5 nA). The figure displays a threshold contact time for deposition of ∼25 μs.

2-5 Discussion

While we have proved that the localized Cu deposition process studied here is electrochemically driven, we find a particularly intriguing critical dependence of deposition on the contact time. Namely, the longer the contact time, the more material is deposited. This is rather counter-intuitive as we suspect the tip to be in electrical contact with the substrate during the time in contact (See SI 2-8 for more details), and therefore suspend electrochemical growth. To understand the need for an "off-time" for local electrochemistry, we consider the role of ion dynamics in the charge transfer at the solid-liquid interface.

Upon application of an external voltage at an electrode, ions in solution are expected to reorder and form the electrical double layer, i.e. a region containing a nonzero charge density that screens the electrode potential. The screening occurs in a diffuse layer extending from the electrode to the bulk solution (Fig. 2-4a). While this potential drop typically occurs within a distance of 1-2 nm, the screening length or Debye length, λ_D, extends to ∼150 nm for the highly dilute 1 μM $CuSO_4$ solution. This is due to λ_D being inversely proportional to the square root of the concentration ($\lambda_D = \frac{9.7}{n}\sqrt{C}[nm]$ for aqueous solutions with $\epsilon = 80$ at room temperature, where n is the ion valence and C the concentration in units of mM) [11, 111]. Faradaic currents exponentially increase with the potential difference between that of the solid and of ions in the liquid within a tunnelling distance (few nanometers). Consequently, in conventional electrochemistry the ultimate current for a given bias is achieved once the double layer is fully formed, bringing ions close to the interface, and its magnitude increases with decreasing λ_D.

Considering oscillation amplitudes ranging from 10 to 300 nm, it becomes apparent that the typical electrode separation lies within the long screening length of the dilute electrolyte. In fact, due to incomplete screening the electrostatic attractive force is large enough to be sensed by the AFM. We observe this as an attractive force offset of ∼4 nN in the baseline when executing a single force curve on the substrate and toggling the applied potential at contact (SI 2-9). In the case where the electrode separation is $\leq 2\lambda_D$ (which has also been referred to as double layer cross-talk) [57], the electrochemical conditions in the gap are not well-defined and may lead to unconventional electrochemistry. The double layer overlap between an STM tip and a metal substrate has been suggested to cause an enhanced local dissolution of the substrate while being held at a known potential, where no dissolution is expected [58,60,112]. Particularly different in these works with respect to ours, is the much smaller gap sizes (< 2 nm to ensure feedback from tunnelling current) and the unlimited access to the solid metal atoms for the oxidation reaction.

The interesting implication of incomplete screening in the gap is that the tip and substrate effectively form a capacitor. In other words, the ions inside the gap are subject to a (linear) potential profile between the electrodes purely defined by gap size and bias voltage (Fig. 2-4b). In the limiting case of no free charges in the gap, the potential can be calculated by solving Laplace's equation. Considering the plane of closest approach for a solvated ion (0.6 nm arising from the size of the water molecule [11]), the solution potential at the interface is raised by $\sim 5\%$ of the tip voltage at a 10 nm gap size, and up to $\sim 20\%$ at 3 nm, as illustrated in Fig. 2-4c. Since we typically use bias voltages up to ~ 2 V, the unscreened tip perturbation can potentially increase the electrochemical potential of ions inside the gap by up to a few hundred mV through direct electrostatic interaction. This effect greatly enhances the local charge transfer, leading to local growth. However, the direct electrostatic interaction quickly

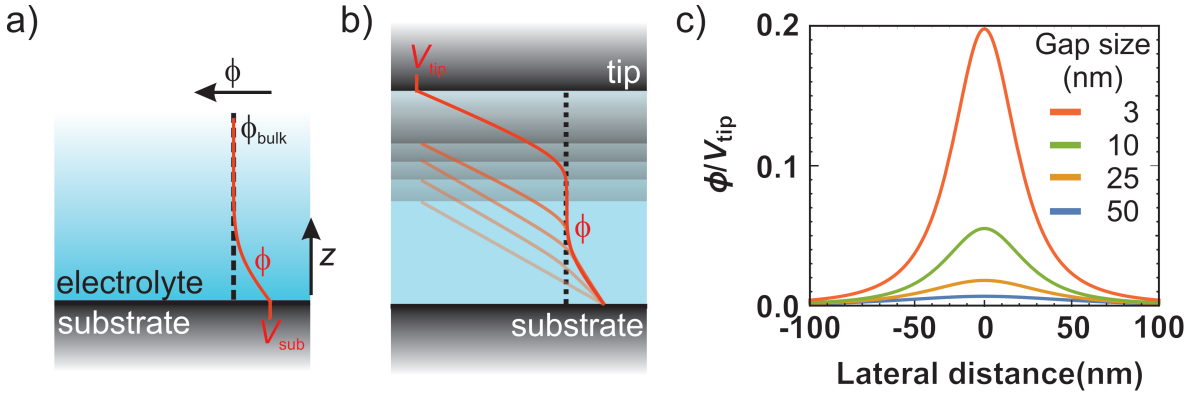

Figure 2-4: Tip-enabled local deposition mechanism in dilute electrolytes. **a)** Schematic representation of the potential drop at the solid-liquid interface for the general case of a metal electrode and **b)** within the tip-substrate gap. When the gap size is smaller than twice the Debye screening length, the potential linearly decays with the distance. **c)** Calculated potential profiles at 0.6 nm above the substrate for various gap sizes (3, 10, 25 and 50 nm) as obtained from the 2D Laplace's equation. We have considered a tip of 25 nm in radius held at a potential of V_{tip} and a grounded substrate. The potential is normalized to the tip bias.

disappears as the tip moves away from the substrate and/or upon the build-up of the double layer.

At small potentials, both the assembly and disassembly of the double layer are associated with the diffusion of ions from the bulk to the interface, and vice versa, through the diffuse layer over a time $\tau_D = \frac{\lambda_D^2}{D}$, with D being the diffusion coefficient [26]. In standard electrochemistry, τ_D is of the order of ns. However, given the extended screening length in the dilute electrolyte, τ_D is 22 μs (33 μs) for the SO_4^{2-} (Cu^{2+}) ions (using $D_{SO_4^{2-}} = 1.065 * 10^{-5}$ cm^2 s^{-1}, $D_{Cu^{2+}} = 0.72 * 10^{-5}$ cm^2 s^{-1}), which is remarkably close to the contact time threshold for deposition found in Fig. 2-3c. The continuous full disruption of the EDL by the tip being in contact with the substrate for a time $> \tau_D$ facilitates the incomplete screening in the gap at each tapping cycle. Similar to potential-pulsed electrochemistry, the contact time or "off-time" results in electrochemical equilibrium by means of double layer relaxation. This equilibrium is then disturbed when the cantilever moves up, and the EDL reassembles again by ions moving into the tip-sample gap. Potential pulses at STM tips have led to confined electrochemical machining, atomic layer electrochemical deposition or control over crystallographic defect formation, among other phenomena [13,61,64,113].

Although the proposed writing mechanism predicts that the local current increases with tip bias, we observe that the deposition is generally hampered at high potentials unless the gap size is small (Fig. 2-3). We believe that accelerated charge screening from field-enhanced ion transport reduces the total effective time for tip-induced double layer squeezing. Along this line, we suspect that access of ions into the gap becomes restricted for gap sizes smaller than 10 nm (see approach curves in SI 2-8). In this case, a higher driving potential is required to facilitate mass transport. This results in a balancing between the driving potential and the gap size, as observed in our measurements in Fig. 2-3b and c. Also, it seems that at high driving potentials the CT threshold for growth occurs at longer times. We suspect that steric effects may play a role, based on the fact that at high potentials or in highly concentrated electrolytes (such as ionic liquids), the double layer actually expands [25,114]. In such a case,

more time would be required to reach electrochemical equilibrium during the "offtime".
Finally, we comment on the fact that higher concentrations hamper the local deposition within our available parameter window. Considering the discussion above, it is noteworthy that at just slightly higher concentrations, 10 μM, the improved screening power of the electrolyte results in the Debye screening length being about three times shorter ($\lambda_D \sim 50$ nm). Double layer cross-talk and direct electrostatic interaction in less dilute electrolytes are therefore expected only at small oscillation amplitudes, where mass transport limitations become dominant. Further dilution of the electrolyte might broaden the deposition parameter window, but rapidly becomes impractical.
In summary, the writing mechanism requires a careful compromise between the tip-substrate electrostatic interaction (achieved by continuously disrupting the double layer and closely positioning the tip above the sample) while still allowing ion access. In our experiments, this occurs only in highly dilute electrolytes (< 5 μM) with an extended Debye screening length combined with either: (a) oscillation amplitudes $\sim$ 25-50 nm, CT $\sim$ 100-150 μs and low drive potentials, or (b) small oscillation amplitudes ($\sim$ 10 nm), long CT (> 200 μs) and high drive potentials. While the latter conditions result in faster writing speeds (up to 3 * 10^4 nm^3 s^{-1}), the former is best in terms of process efficiency, which considers the ratio between total charge transfer and local volume.
Based on the deposition mechanism described above, we suspect that only a small fraction of the non-contact time is responsible for the local deposition, reducing both the writing speed and process efficiency. In our system, the tip oscillation frequency is fixed at 2 kHz and we obtain practical deposition rates in the order of 10^4 nm^3 s^{-1}, which is comparable to that for focused ion beam induced deposition [5]. The writing speed, and consequently the process efficiency, may be optimised by tuning the tip oscillation frequency. Additionally, the overall process efficiency may also be improved by just reducing the substrate's surface area or by using a 4-electrode configuration, which fixes the substrate potential exactly at the $Cu|Cu^{2+}$ equilibrium potential.
Regarding the writing resolution, further down-scaling is possible by the use of sharper tips considering that the observed resolution is of the size of the nominal tip diameter. Nowadays, conductive tips can be routinely fabricated with a diameter < 10 nm. Sharper tips may also aid the deposition process by mitigating screening effects, due to the enhanced charge density and capacity of sharply curved metal surfaces [13].

2-6 Conclusion

We have demonstrated the confined high-resolution direct additive writing of copper nanostructures by using a biased AFM tip in a dilute electrolyte, where the tip is in intermittent contact with the substrate through the oscillation of the cantilever. We find a particularly intriguing critical dependence of deposition on the tapping dynamics of the AFM and ion concentration. We propose a confinement mechanism that balances access of ions and shaping of the electrochemical potential in the tip-substrate gap. While this method is expected to be general for the electrochemical deposition of a variety of materials, opening up new routes for nanofabrication, probing local reactions through topography provides a way to understand the local dynamics and charge transfer at the electrical double layer, such as the Debye time.

2-7 Methods

Sample and electrolyte preparation
The substrate consists of a Au film ($\sim$ 50 nm thick) with a $\sim$ 5 nm Cr adhesion layer deposited by thermal evaporation on top of an n-type Silicon sample (Siegert Wafer) as a flat support. The solutions were prepared using $CuSO_4{\cdot}5H_2O$ powder (99.995%, from Sigma-Aldrich) in MilliQ®(18.2 M$\Omega \cdot$ cm) water. The low concentration electrolyte was prepared before every experiment from a 1 mM $CuSO_4$(aq) stockpile and diluted (100-1000x) using fresh MilliQ water. Before preparing the dilute electrolyte, all containers were rinsed (5-10x), ultrasonicated, and rinsed again (5-10x) using fresh MilliQ water. Both the container and electrochemical cell only contained the dilute copper electrolytes, after initially cleaning them by an overnight soak in 1 M HCl. All experiments were carried out under ambient conditions inside a fume hood. Samples and the electrochemical cell were stored in a 1% humidity nitrogen environment.

Electrochemistry
Our electrochemical system consists of an AFM nanoelectrode tip immersed in a filled electrochemical cell and connected to an external potentiostat, which controls and monitors potential and current. At positive potentials (tip vs. substrate), we expect the oxygen evolution reaction to occur at the tip and either copper reduction or hydrogen evolution at the sample. The electrochemical cell was homemade and consisted of Teflon™, made leak tight by an O-ring. Top-contacts were made by either attaching a wire connection directly to the sample edge, or by using a spring-loaded pin outside of the O-ring. Potential/current control and readout were done with a CH760E potentiostat. In all experiments, the system was connected in a 2-electrode fashion, by shorting the reference and counter electrode.

Atomic force microscopy
The measurements and writing were performed using a Bruker Dimension Icon AFM, controlled through the Nanoscope software. The nanoelectrode AFM probes were obtained from Bruker (PeakForce SECM) and were electrically insulated except for the platinum coated apex, which has a diameter of $\sim$ 50 nm [110]. The AFM spring constant was obtained for each cantilever (i) directly in the electrolyte, by doing a thermal tune at a distance of $\sim$ 1 mm from the substrate after obtaining the deflection sensitivity on the gold substrate inside the electrolyte, or (ii) before filling the cell using the thermal tune method in air at a distance of $\sim$ 1 mm from the substrate, after obtaining the deflection sensitivity on the gold substrate. The deflection sensitivity of the cantilever was then re-calibrated on the gold substrate, inside the electrolyte. The measured f_0, Q, and used k are reported in tables 2-1 and 2-2 in SI-6, as proposed in reference [115]. Ex situ topography and data in Fig. 2-1 b, c, and 2-2 were obtained in air using ScanAsyst-air tips (Bruker, nominal tip radius 2 nm). In situ images and data in Fig. 2-1d and 2-3 were collected using the SECM tip, directly after deposition.

Writing Protocol
For writing, the tip follows a programmed trajectory (NanoScript) in the xy-plane with the PeakForce (PF) feedback enabled, while applying either a potential difference between the tip and the substrate (potentiostat) or forcing a fixed current through the tip (galvanostat). In all presented experiments, the PeakForce frequency was set to 2 kHz, other AFM parameters used are listed in SI-6 table 2-1. Lift experiments where the tip is kept at a fixed distance above the substrate, as mentioned in the text, were done by initiating a Thermal Tune within the AFM software at a certain height.

Data Treatment

AFM images were treated by removing the polynomial background (first or second order) and removing image defects by aligning rows or removing scars using the Nanoscope Analysis and Gwyddion software [116]. The volume data in Fig. 2-2 were defined as the bearing volume in the deposited lines, with a threshold value for each pixel set to two times the sample roughness. The height data in Fig. 2-3a were obtained by taking the average line profile of a written copper wire and fitting a Gaussian to obtain the height and full width half maximum as illustrated in SI 2-10. The volume in Fig. 2-3b was then taken to be the area of this fit multiplied by the length of the path. Fitting was done using the Origin 2017 software.

Analytical Model

We have considered a mirror charge at a distance of 'gap size' from the interface. V_{tip} is defined as the potential at a radial distance of 25 nm, and we have used the dielectric constant of water (80). We consider the substrate to be grounded with respect to the solution. This is a fair approximation given the much larger current density flowing through the tip.

2-8 Supplementary information

SI-1 Elemental characterization of a larger deposit using SEM-EDX

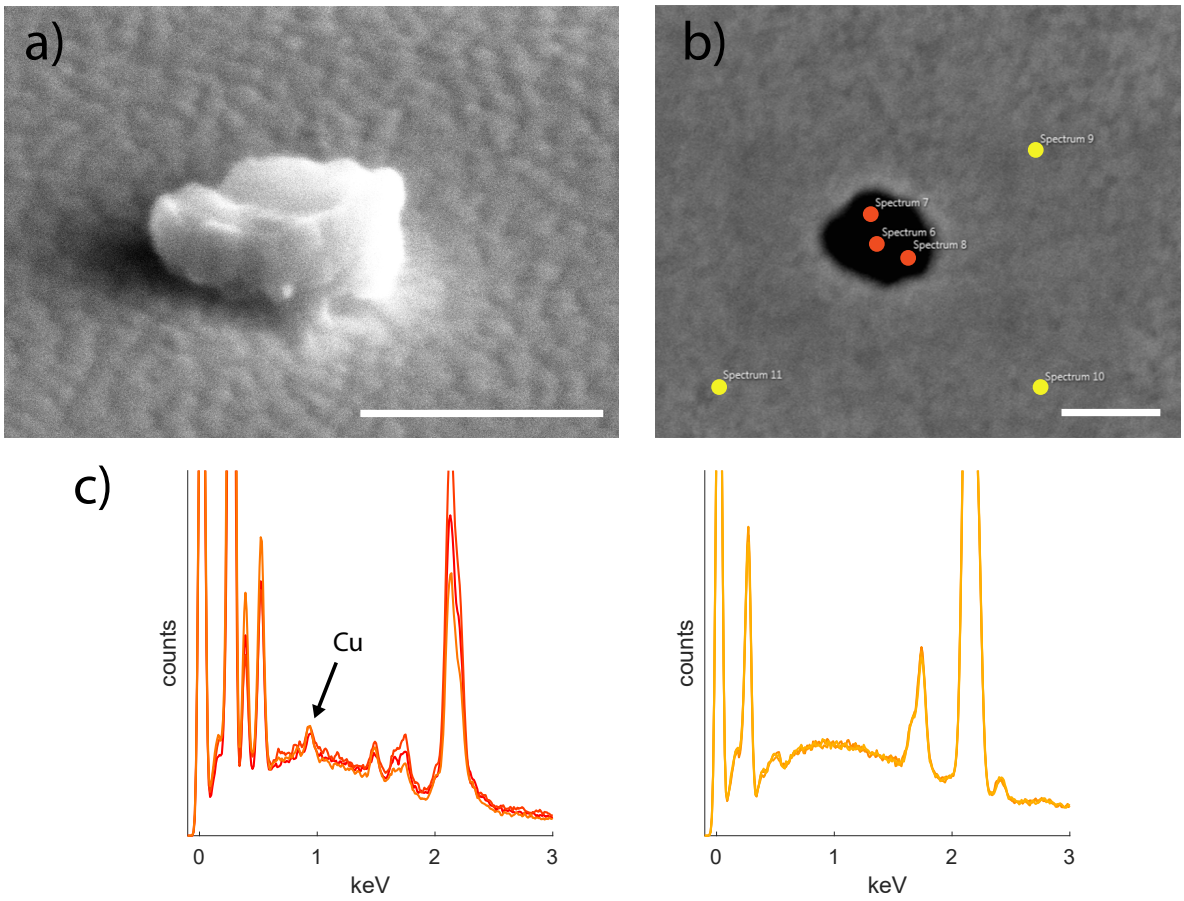

Figure 2-5: A larger structure was deposited by keeping the tip at the same location for an hour (while tapping) with a potential difference of 2 V between the tip and substrate. **a)** Secondary electron SEM image of the deposit (55° tilt) **b)** Backscatter electron image (0° tilt), displaying elemental contrast between the deposit and the substrate. The scale bar is 400 nm in both images. **c,d)** EDX spectra of the points indicated in b) on the deposit, c), and on the substrate, d). A clear peak associated with copper is observed at $\sim$ 0.94 keV, which is absent in the reference spectra. Peaks in the reference are associated with gold, 2.13 keV, silicon, 1.74 keV and carbon, 0.02 and 0.27 keV. Additional peaks in the deposit include oxygen (0.52 keV), nitrogen (0.39 keV), and aluminum (1.49 keV), the last 2 of which we attribute to scattering inside the SEM chamber. Spectra were acquired with an acceleration voltage of 5 keV and a current of 800 pA.

SI-2 Dependence of cantilever position on AFM parameters

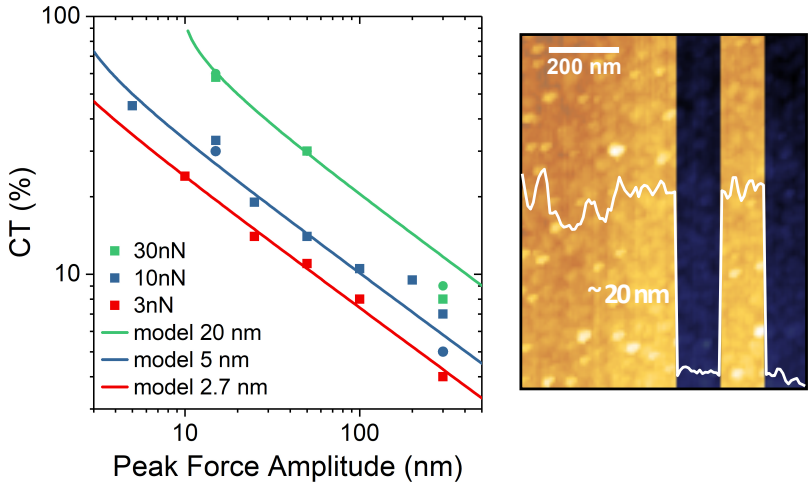

Figure 2-6: The average gap size <z> as referred to in the main text is determined by integrating the tip position from the highest point up to the point of contact divided by half the oscillation period (eq. 2-1). The figure illustrates the effect of peak force amplitude and peak force setpoint on the amount of time spent in contact with the sample. **Left)** Contact time as read out from the Nanoscope software as a function of peakforce amplitude for different force setpoints (squares). The center of the sinusoidal oscillation is expected to shift by the force setpoint divided by the spring constant, assuming no indentation of the sample. For the nominal spring constant of 1.5 $\frac{N}{m}$ This gives a shift of 2, 6.7, and 20 nm for a setpoint of 3,10, and 30 nN, respectively. The solid lines are a fit to the data calculated for a sinusoidal movement of the tip with the center of oscillation given by amplitude-x, yielding x = 2.7, 5, and 20 nm for the different forces in good agreement with the expectation. **Right)** Raw AFM height sensor data when switching the peakforce setpoint from 3 nN to 30 nN twice during the scan (scan from left to right). The height profile in the overlay illustrates how the z-piezo moves down ($\sim$ 20 nm) due to the force setpoint.

$$< z >= \int_0^{\frac{T-CT}{2}} PFA \cdot cos(\frac{ft}{2\pi})\, dt \cdot \frac{2}{T} \tag{2-1}$$

With CT the measured contact time, PFA the peakforce amplitude and using frequency f = 2 kHz, and period T = 500 μs

SI-3 Width of deposited lines

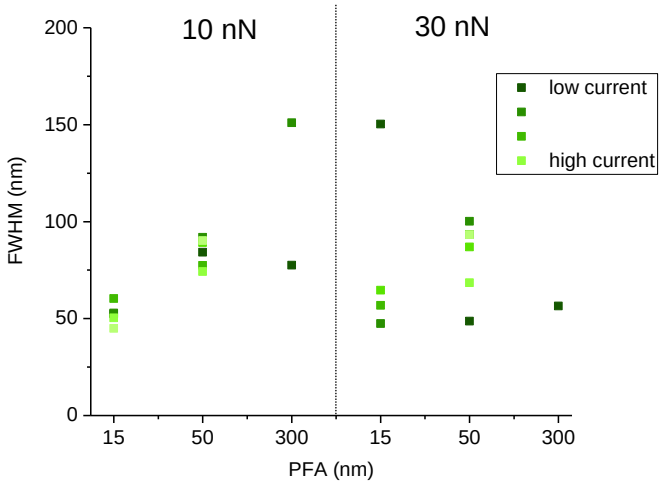

Figure 2-7: The full width at half maximum of the lines used for Fig. 2-3b in the main text. The individual datapoints for all currents are displayed, where dark to light green indicates low to high current (arbitrary scale).The amount of current datapoints varies for each set of oscillation parameters as growth is not always observed (see main text). While the width seems to increase slightly at intermediate amplitude, no clear trends in the width are observed as a function of the applied current.

SI-4 Current response of the nanoelectrode in consecutive approach curves

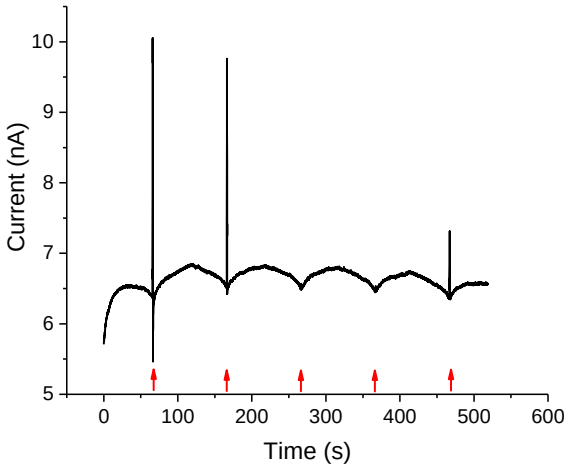

Figure 2-8: Current response at the AFM nanoelectrode when executing 5 consecutive approaches with a tip potential of 1.7 V. The tip is approached and retracted over a distance of 1 μm with a frequency of 0.01 Hz (20 $\frac{nm}{s}$). The approach curves show that the current decreases/increases as the tip approaches/retracts from the surface. At the point of contact (red arrows), a show circuit current is observed. The current sampling rate is 20 Hz. The approach is terminated at an applied force of $\sim$ 10 nN.

SI-5 Deflection of AFM cantilever in liquid when applying a potential

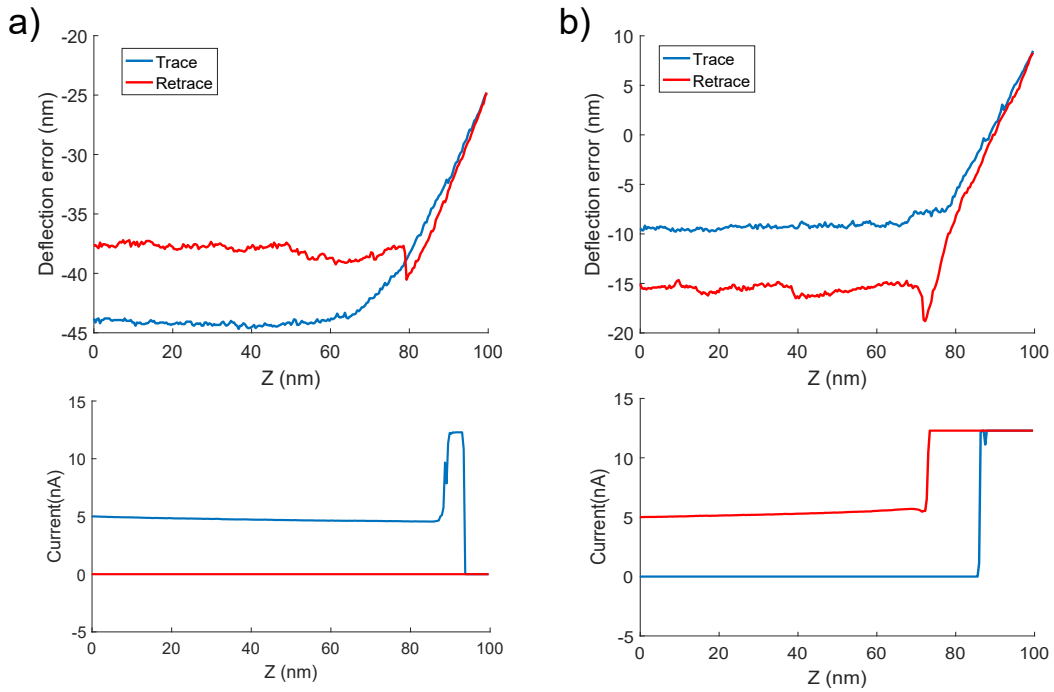

Figure 2-9: Single approach curve of the AFM tip where the tip-substrate potential (2.1 V) was manually turned off/on during contact for the retrace in the left/right panels, as seen in the current channel (bottom panels). In both cases, an attractive force is observed in the deflection of the cantielver (top panels) when the potential is applied. The difference in deflection of $\sim$ 5 nm corresponds to $\sim$ 4 nN. The ramp size is 100 nm, at a frequency of 0.01 Hz (2 $\frac{nm}{s}$). The force trigger for the approach was set to $\sim$ 15 nN.

SI-6 AFM parameters and cantilever resonance characteristics

Table 2-1: AFM parameters used during the deposition process.

Used in Fig	Peakforce Amplitude (nm)	PeakForce setpoint (nN)	Translation speed ($\frac{nm}{s}$)
1b	50	30	3
1c	50	30	30 + 3 (consecutive)
1d	50	6.3†	10
2b	50	30	10
2c	50	30	3,10,30,100
3b	15, 50, 300	10, 30	10
3c	10, 25, 50, 100, 300	3	10
SI 2-5	50	30	
SI 2-7	15, 50, 300	10,30	10

† The Force was set in terms of the photodiode voltage with a deflection sensitivity of 35 $\frac{nm}{V}$ and a spring constant that was later determined to be 1.8 $\frac{N}{m}$ (see next table). This yields a

force of 6.3 nN for the used setpoint of 0.1 V.

Table 2-2: Resonance characteristics and spring constants of cantilevers used.

Used in Fig	f_0 in air (kHz)	Q in air	k ($\frac{N}{m}$)
1b	65.7†	208	1.68
1c	32.6‡	-	1.80
1d	63.4†	214	-
2	65.7†	208	1.68
3b	58.3	195	1.41
3c	63.4†	210	1.59
SI 2-5	51.3†	116†	
SI 2-7	58.3	195	1.41
SI 2-8	58.3	200	1.25
SI 2-9	52.1†	105†	1.15

† Frequency and Q-factor were obtained in air for that tip on a different day than the day of the measurement, the reported spring constant is the value used on the day of the measurement, as obtained in the liquid.
‡ Frequency was obtained with the tip immersed in the liquid

SI-7 Line profile fitting and analysis

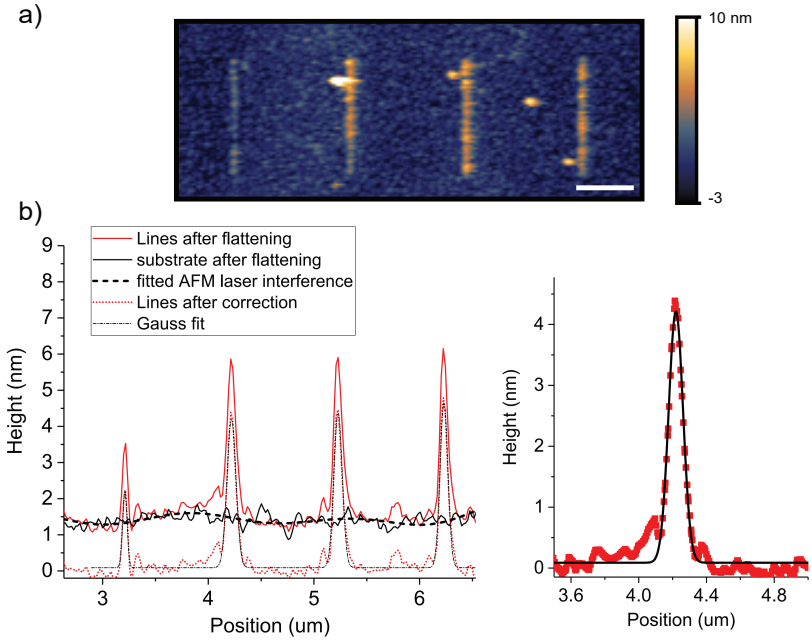

Figure 2-10: a) Representative AFM image as used in the main text (Fig. 2-3b, 30 nN, 50 nm amplitude, for different currents). The scale bar is 500 nm. **b)** *left)* averaged profile of the lines along the vertical direction (solid red curve). The solid black curve is the average profile of the substrate outside the lines used to account for the laser interference (dashed black cuve). The dotted red line is the background corrected average line profile. The thin dash-dotted line is the Gaussian fit. *right)* zoom-in of the profile and fit of 1 line (second from the left)

Chapter 3

Shape evolution in nanoscale electrocrystallization

The previous chapter demonstrated the direct electrochemical writing of copper nanostructures. While we show high spatial control over the electrodeposition process, in the context of the free-form fabrication of functional materials it is relevant to control the nucleation and time-dependent growth, and assess the quality, e.g. crystallinity, or material properties of the deposited structures. Analysis of the nanoscopic deposits is difficult as there is little material available. We therefore investigate these structures, and compare the directed growth to that of copper structures grown in a regular electrochemical cell, using atomic force microscopy (AFM) and X-ray photelectron spectroscopy (XPS). We find that the directed deposition from μM electrolytes is distinctly different that that of conventional copper deposition, but results in similarly shaped spheroidal nuclei as those obtained in macroscopic growth in dilute conditions. The latter are found to mainly contain CuO, making it likely that the directed deposition also consists of copper oxide species. The methods presented in this chapter are general and open further possibilities of *in-operando* study of electrochemical growth or surface stability.

3-1 Introduction

Controlling the shape evolution of crystallization process is an important step in tailoring materials for specific functions. In solution based growth, such as electrochemistry, considerable control over the shape can be achieved through combinations of solvents, additives, and pH, in addition to heat and pressure. For instance, as illustrated in section 1-1, crystal morphology is often controlled through capping agents that hinder growth of certain crystal facets by specific adsorption [22, 117]. By judiciously choosing growth parameters and environment, materials can be engineered for a wide variety of applications ranging from catalysis to nano-photonics [118–121]

Recently, localized electrochemistry has emerged as a way to direct the growth in space as

it happens, in a 3D printing fashion. Moving scanning probes and pipettes have shown to direct growth for a number of metals and semiconductors into intricate 3D nanostructures. Studying the early stages of electro-crystallization is often not trivial however [93,102,122], as the low density and small volume of the deposits hampers the use of standard characterization methods, such as X-ray diffraction, X-ray photoelectron spectroscopy (XPS) or transmission electron microscopy.
Atomic force microscopy (AFM) yields high resolution topography of the sample which holds information on the particle shape, and crystal orientation through faceting. However, analysis of the resulting images is often dependent on the use of color maps and height profiles along sections. Especially in images with a large height distribution (and associated colorrange) or many regions of interest, features can be obscured. More generally, resolving the shape of the particle from the topography map requires perception of the *gradient* in the color scale [123] To better assess particle shape and characteristics of differently grown particles, regardless of overall size, we consider inclination maps, where each pixel represents the magnitude of the local inclination with respect to the substrate through the simple arithmetic operation [124,125],

$$\theta(x,y) = \arctan\left(\sqrt{\frac{dz}{dx}^2 + \frac{dz}{dy}^2}\right) * \frac{180^\circ}{\pi} \tag{3-1}$$

With x, y, and z the topography coordinates, and θ the local inclination.

In this chapter the crystal growth in directed nanoscale-electrochemistry from a highly dilute electrolyte is compared to that in macro-electrochemical copper deposition using AFM and XPS. AFM topography-, and inclination mapping are combined to highlight the shape and orientation of nanoscale growth centres, regardless of their overall size. We find that the nanoscale deposits are different from typical copper deposition but resemble a spheroidal shape similar to those found in macroscopic electrodeposition in similarly dilute conditions. XPS confirms that the latter mainly consists of CuO, making it likely that the directed deposition also consists of copper oxide species. Furthermore, we show that the tip-mediated deposition evolves with an increasing aspect ratio, which is critical for the controlled fabrication of out-of-plane structures.

3-2 Out-of-plane growth

The previous chapter demonstrated the direct electrochemical writing of copper nanostructures through a mechanism illustrated schematically in Fig. 3-1a, with the deposition tracking the tip as it is translated along the surface. Upon inspection of the written lines, these appear to consist of multiple grains, as depicted in the line in Fig. 3-1b, written by translating the tip at 10 $\frac{nm}{s}$. In fact, as the nucleation does not appear to be instantaneous, the grain density changes by varying the translation speed along the line.
Fig. 3-1c shows 4 lines (1 μm long) written at different translation speeds, and the projected area along the 1 μm paths (left axis, black) and the total volume (right axis, blue) are plotted, as obtained from the ex-situ AFM images. All lines are written from a 1 μM $CuSO_4$ solution, with the same tapping parameters (30 nN peakforce setpoint, 50 nm amplitude, at 1.7 V)
From the figure, we observe a slowed increase of the footprint as the writing time increases. This can be explained by an increase of the grain density within the line, which saturates

once the grains along the path coalesce, but do not expand laterally. The volume on the other hand increases linearly with writing time, as expected from the electrochemical nature of the process at $\sim$ constant current. Importantly, the fact that the volume grows faster relative to the projected area indicates that the tip-mediated growth is directed out-of-plane at longer writing times.

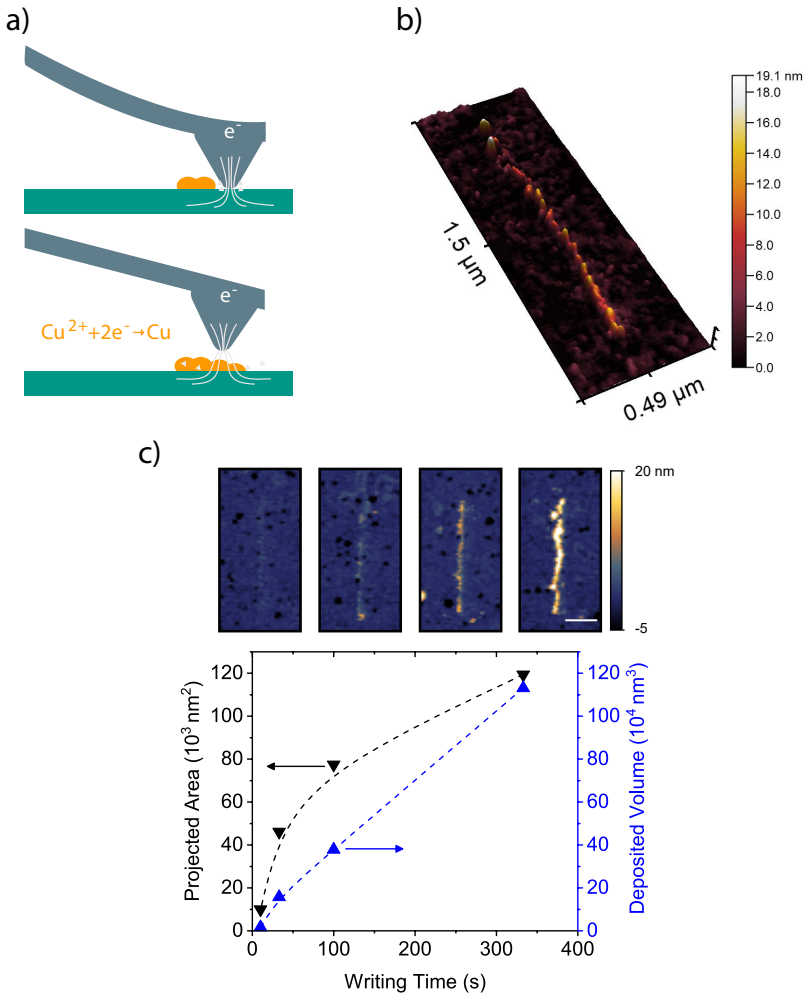

Figure 3-1: a) Schematic representation of the direct patterning of electrochemical deposition. **b)** Directed electrodeposition of a single line by translating the AFM tip electrode along a 1 μm long path at 10 $\frac{nm}{s}$. **c)** Projected area (black, left) and total deposited volume (blue, right) of lines for increasing writing time, obtained from ex-situ AFM topography maps, as shown in the panels on top. The writing time is varied by means of the translation speed of the tip along the 1 μm long lines. The scale bar in the panels is 250 nm.

3-3 Nanoscale shapes

The fact that growth occurs via nucleation, grain growth and coalescence has major implications in the material quality of deposits as well as in the interplay between directed

electrodeposition and crystal energetics, which will define the 3D shape of the deposit. We are therefore interested in the initial stages of the deposition process.
However, as there is very little material in structures grown using the AFM, and the coverage is extremely low, characterization of the deposits is difficult. We therefore compare the topography of crystal growth in directed nanoscale-electrochemistry to that of copper deposition in a conventional 3-electrode system, where all substrates are gold coated silicon.

Fig. 3-2 a-c display the resulting AFM topography images with Fig. 3-2a a line fabricated by directed Cu electrodeposition, at a translation speed where the individual grains can be discerned. We observe spheroidal-like grains with no clear facets as those reported in literature for (non-directed) Cu electrodeposition from $CuSO_4$ salts [126, 127].
This is depicted in Fig. 3-2b, showing the *in-situ* topography obtained after non-directed Cu electrodeposition from 100 mM $CuSO_4$ upon applying -50 mV vs. a Cu wire quasi reference electrode (QRE) for 6 seconds. Notice that the salt concentration is similar to what is used in standard Cu electrodeposition, and it is five orders of magnitude higher than in our directed growth experiments, which leads to slightly lower pH values (pH $\sim$ 4 vs. 6). In agreement with literature, growth under high salt concentration results in well-defined faceted nanocrystals.
As a fairer comparison, we performed non-directed Cu electrodeposition with the same electrolyte conditions as in the directed case (1μM $CuSO_4$), the topography of which is shown in Fig. 3-2c. Here we use a macroscopic Cu wire as counter electrode instead of the tip, as a means to replenish copper ions and avoid depletion in the bath. After 50 minutes of potentiostatic growth at -1 V vs. Cu wire QRE, the gold substrate was covered by small ($<$ 100 nm) elongated nanostructures,that appear to be limited to $\sim$ 10 nm in height.

The resulting morphology is very different to the concentrated electrolyte case. We therefore turn to the corresponding inclination maps, obtained from the topography using equation 3-1, shown in Fig. 3-2 d-f . Additionally, Fig. 3-2 h-j display histograms of the angle distribution of the particles indicated in Fig. 3-2 a-c (green squares and red ellipses, the pixels used in the histogram are defined using a mask)
In the high concentration case (Fig. 3-2e), the faceted nature of the particles is clearly represented by equi-angle planes. Furthermore, the figure highlights one of the difficulties encountered in representing particles with a large size distribution, where one of the particles is clipped in the axis of 3-2b, while Fig. 3-2e reveals that this particle displays 4 distinct facets. From the histograms in Fig. 3-2i, we observe two well-defined peaks in each grain, at 28° and 42° or 20° and 50°, arising from the two facets that can be seen in the particles in Fig. 3-2e. The 70° angle between the two facets in both grains is in good agreement with that expected between the {111} and $\{\overline{1}\overline{1}1\}$ planes of a Cu crystal with respect to a {110} base. The broad peak around 60° is likely an artifact. Despite that the nominal tip shape should allow access to angles up to 65-75°, Fig. 3-2i shows that the main contribution to the high angle peak comes from the edges, where the tip falls of the grains.
This is quite different from both cases where dilute electrolytes were used. The angle distributions as shown in is Fig. 3-2h and 3-2j are broad, asymmetric, and centred at small angles, and it is well reproduced by that of the top half of a spheroid given by (dashed curves);

$$z = \sqrt{h^2 - \frac{x^2 * h^2}{l} - \frac{y^2 * h^2}{w^2}} \tag{3-2}$$

with base dimensions w, and l, and height z obtained from the topography images.

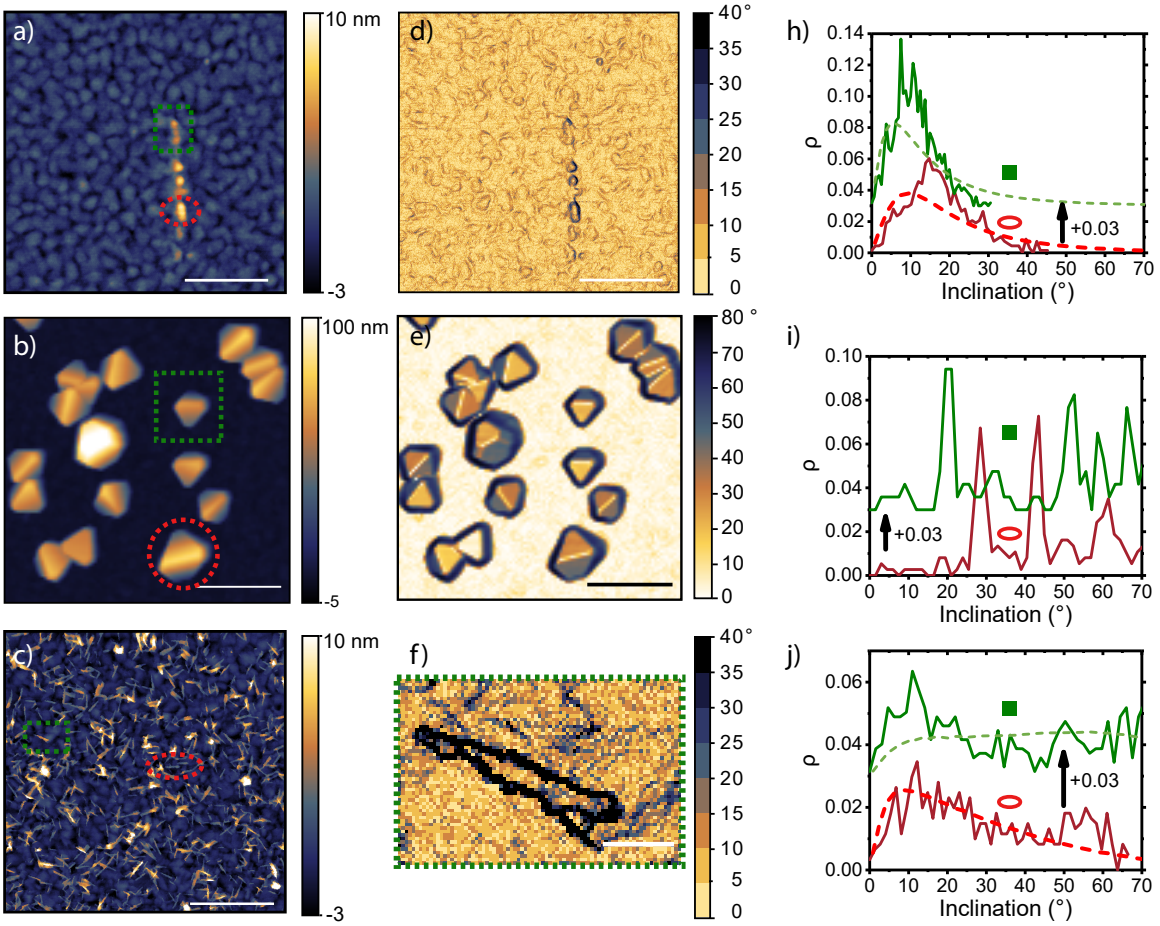

Figure 3-2: left column, a-c) AFM topography of **a)** a line written at 10 nm/s with directed electrodeposition, which shows a few individual grains along the writing path. **b)** Non-directed Cu electrodeposition at -50 mV vs. Cu QRE for 6 s from a 100 mM $CuSO_4$ solution, showing crystalline particles. **c)** non-directed Cu electrodeposition from 1 μM $CuSO_4$ at -1 V vs. Cu QRE for 50 minutes, showing a random distribution of small fin-like elongated grains. **Middle column, d-f)** Corresponding inclination maps of images a-c. **f)** only displays the particle as indicated by the green dashed square. **Right column, h-j)** Normalised histogram of the angle distributions for the grains indicated in a-c by either a green square or red ellipse. The dashed lines correspond to the expected inclination distribution for a spheroidal shape with dimensions obtained from the topography images. The curves are vertically shifted as indicated, for clarity. The scale bar in all images is 300 nm, except for **f)**, which is 20 nm.

In the case of directed growth, the grain footprint is more symmetric and the base-to-height aspect ratio is smaller, giving rise to a narrower angle distribution as compared to that grown in the regular EC-cell. We also observe some deviation in the angle distribution from that of a spheroid. A peak at low angles (around 10° for the grain marked in green and at $\sim$ 15° for that marked in red) and the absence of angles from 30° and onwards deviate from the simple spheroid shape. Both deviations can be attributed to a slightly slanted base around the grain that is consistently found in grains in direct-written lines, as illustrated in Fig. 3-2d.

In the case of non-directed growth, a broad secondary peak in angle distribution can be discerned around 55-60°, which is again seen to be located at the edge of the particle in Fig. 3-2f. and attributed to a tip artefact. Notably, there is no indication of equi-angle facets in either case.

3-4 Growth from a dilute 1 μM $CuSO_4$ electrolyte

The deposition from the dilute electrolyte is somewhat curious, as quite high potentials and long growth times were required for deposition. Fig. 3-3a shows AFM topography images (*ex-situ*) after ∼15, 50, and 420 minutes of potentiostatic growth at -1 V vs. the Cu QRE. No growth was found at lower potentials (-50, -300 , -500 mV vs. the Cu QRE for 15 min). Longer growth times result in higher particle coverage with particles progressively overlapping. Particles that can be identified as single rods for the longest growth time in Fig. 3-3a are still limited to ∼ 10 nm in height, with larger clusters going up to ∼ 100 nm. Considering the clearly progressive nucleation, these individual particles could either be limited in their growth or nucleated at later times, compared to the clusters.
Furthermore, when considering one of the large particles in Fig. 3-3b, the edges are now much steeper. While this appears similar to the faceted growth from the higher concentration, it is more likely an effect of a changing aspect ratio, as the histogram is still captured well by an equivalent spheroid (Fig. 3-3d) until the maximum angle of ∼ 75° allowed by the tip.

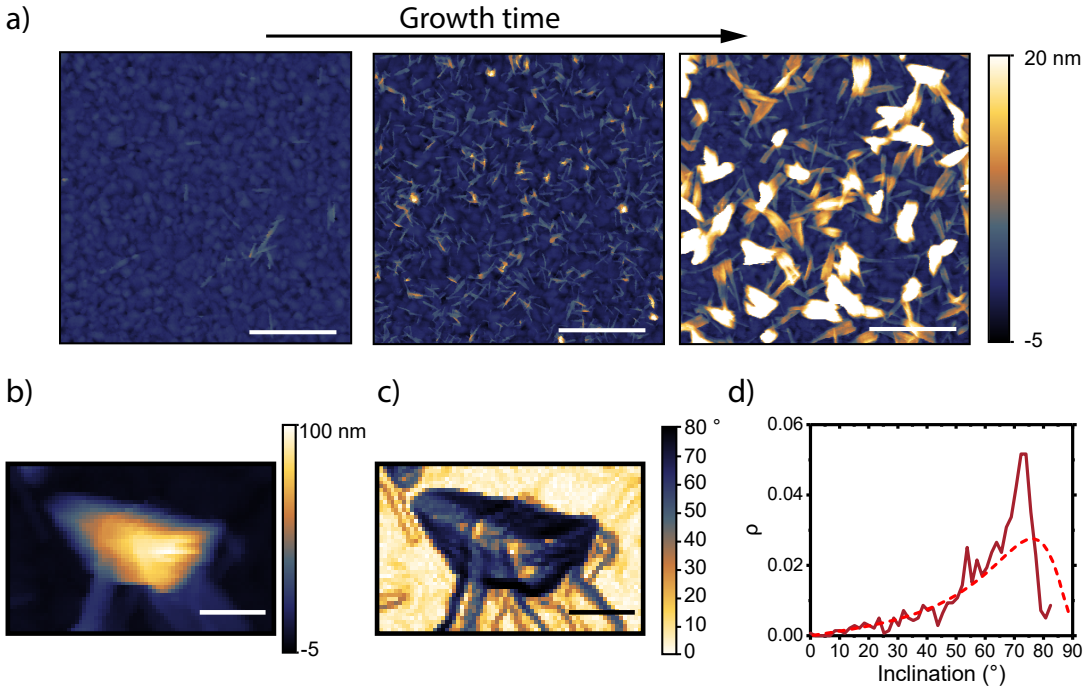

Figure 3-3: a) AFM topography maps of copper grown from 1 μM $CuSO_4$ at -1 V vs. Cu QRE, for increasing growth times, 1000 s, 3000 s, and 25000 s. The scale bars are 300 nm. **b,c)** AFM and inclination map of one of the larger particles in a) for the longest growth time. The scale bars are 50 nm. **d)** Normalized histogram of the angle distribution of the large particle. The dashed line corresponds to the expected inclination distribution for an equivalent spheroidal shape, with dimensions obtained from the topography.

Considering the Pourbaix diagram for Cu at room temperature in the absence of an acidic supporting electrolyte, the deposit is expected to consist of Cu for low salt concentration and either Cu or Cu_2O for high salt concentration [128, 129] Also, similar thin leaf-like morphologies have been found for the (electro)chemical and hydrothermal growth of CuO [130, 131]. Kartal et al. suggested that CuO or Cu_2O forms by the spontaneous chemical oxidation of Cu with dissolved oxygen in the electrolyte when the Cu deposition rate is small. Due to the low metal salt concentration yielding a very low current density ($\sim 1\ \frac{\mu A}{cm^2}$) and the fact that the solution was exposed to air, we suspect that these nanostructures are oxidized.

To verify the elemental content of the structures deposited from the dilute electrolyte we do X-ray photoelectron spectroscopy (XPS) measurements on the sample with the highest coverage, grown for 25000 s as shown in Fig. 3-4. The oxidation state is determined using the Cu $2p_{3/2}$ core level. The binding energy values are calibrated using the Au $4f_{7/2}$ peak of the gold substrate. The predominant species is identified as CuO (blue line), based on the characteristic satellite peak for CuO species, its relative intensity, and the binding energy difference to the main peak [132]. A second species is required to fit the experimental data, which is identified as Cu_2O (purple line), based on the peak position of 932.2 eV. The lowest binding energy peak of the CuO peaks is measured at 933.7 eV, which is 0.6 eV higher than the literature value of 933.1 eV. This is attributed to the charging of the non-conductive CuO species. Based on the Cu $2p_{3/2}$ peak areas, 91% of the sample volume probed by XPS corresponds to CuO and 9% to Cu_2O. While this indeed confirms that the copper is oxidized, this measurement does not rule out the possibility of the oxidation occuring after removing the sample from the electrochemical cell.

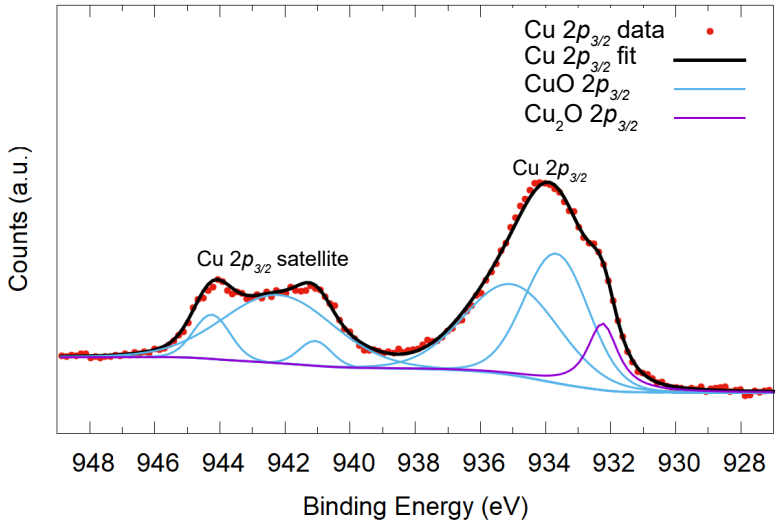

Figure 3-4: Deconvoluted XPS spectrum of Cu $2p_{3/2}$. At the higher binding energy the Cu $2p_{3/2}$ satellite is shown and at the lower binding energy the Cu $2p_{3/2}$ main peak is shown. The experimental values are shown as red dots, the peak fit envelope is shown in black, the CuO $2p_{3/2}$ peaks are shown in blue, and the Cu2O $2p_{3/2}$ peak is shown in purple. The binding energy is calibrated to the Au $4f_{7/2}$ peak of the substrate.

3-5 Statistical analysis of growth

To investigate the grain growth kinetics and shape evolution of the AFM-directed growth compared to the self-assembling case we use the grain analysis developed by Guo et al. [19] Comparing the geometrical information of grains of different size provides information about the growth kinetics, where it is assumed that each island grows independently and obeys the same growth law.
Fig. 3-5a plots the volume and projected area obtained from AFM topography images of grains found in multiple direct-written lines by translating the tip along a 1 μm long trajectory (red circles), where the grains are defined by a pre-defined height threshold in the topography maps. We have considered several conditions for the directed growth, such as different voltages and oscillation parameters, at a translation speed of 10 $\frac{nm}{s}$, where individual grains are visible. Similarly, we also include geometrical data from individual grains obtained from the dilute non-directed growth after 1000 s (blue triangles), and the data for copper grains grown from the higher concentration of 100 mM $CuSO_4$ (green squares).
As explained in Ref [19], the volume (V) and footprint (A) of a growing grain increase following the power-law:

$$V = \alpha A^m \tag{3-3}$$

where α is a proportionality constant that depends on the grain shape (e.g. $\alpha = 1/2$ or 1 for a spherical or cubic shape, respectively) and m carries information about the growth mechanism. The latter is also the slope in a double-logarithmic representation and is defined as $m = 1+b/2a$, where a and b are the corresponding exponents for the lateral and vertical grain growth over time, respectively (i.e. width $\propto time^a$ and height $\propto time^b$). Consequently, the slope reveals whether the grain grows isotropically ($a = b$ and, giving $m = 1.5$), preferentially in-plane ($a > b$, $m < 1.5$) or preferentially out-of-plane ($a < b$, $m > 1.5$).
It is interesting to note that the slope for the dilute growth is the same, regardless of being directed by the AFM. We obtain a slope of $m \sim 1.1$ from fitting a power-law to the data. which indicates preferential in-plane growth. For the higher concentration, we find the growth to be more isotropic with a slope of $m \sim 1.26$ in the double-logarithmic representation, in agreement with literature [133].
This seems to be in stark contrast with the result of Fig. 3-1. However, it should be remembered that the red circles are obtained along lines for a single translation speed so that individual grains are visible. The data as a function of translation speed, representing total area and volume along the line, is depicted by the open yellow circles, where it should be noted that datapoints at higher/lower speeds fall below/above the fitted line, respectively.
Analogously for the non-directed case, the blue triangles in Fig. 3-5a represent the shortest growth time (1000 s), where individual grains could be identified. Due to the increased overlap at longer growth times it becomes harder to define single islands. However, adding a few particles from the sample grown for 25000 s, such as the one from Fig. 3-3b, that are characterized by being much higher than their surrounding shows a similar trend. They are placed above the initial slope (purple open triangles), indicating a changing growth dynamic that is directed more out-of-plane as the coverage becomes high.

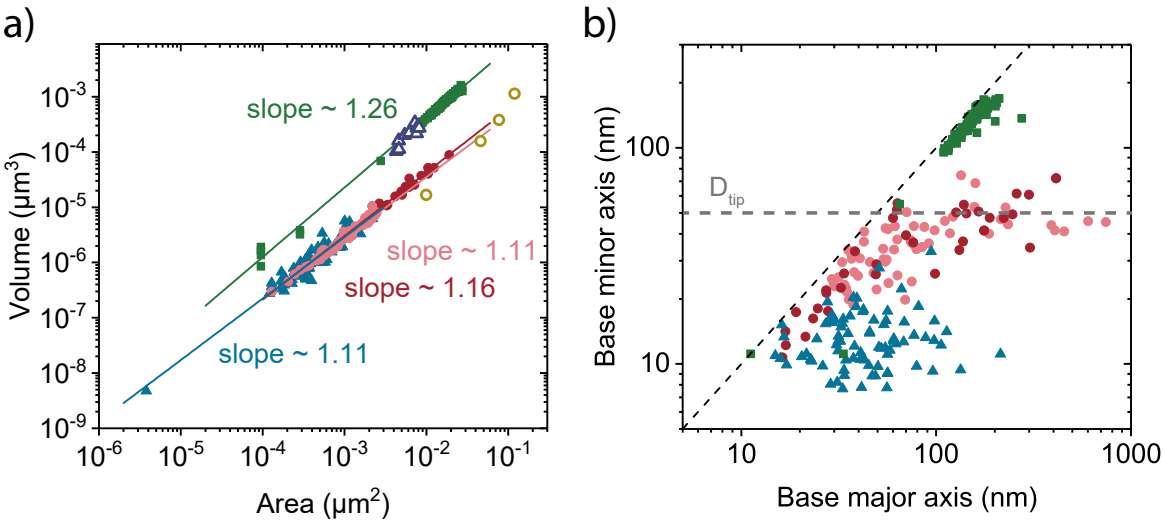

Figure 3-5: a) Volume vs. footprint area for individual nuclei grown under different conditions, as obtained from ex-situ AFM topography. Light and dark red circles: directed growth from 1 μM $CuSO_4$ (aq); blue triangles: non-directed growth from 1 μM $CuSO_4$ (aq); green squares: non-directed growth fom 100 mM $CuSO_4$ (aq). The solid lines are power-law fits to the data points. Open yellow circles and purple triangles correspond to the lines written in directed deposition as shown in Fig. 3-1c, and individually picked large grains from the sample grown for 25000 s as shown in Fig. 3-3a, respectively. **b)** Footprint (a)symmetry evolution represented by the minor vs. major axis for the equivalent ellipse of the same grains as in a). Different markers correspond to the same growth conditions as in a). The black dashed line indicates isotropic growth (major axis = minor axis), and the dashed grey line indicates the nominal tip diameter in directed growth.

Finally, to illustrate the progression of the nanostructure footprint, Fig. 3-5b represents the largest and smallest in-plane dimensions (major and minor axis from a fitted ellipse, respectively) of the same individual grains as in Fig. 3-5a. As expected from the AFM images, the self-assembled wire-like nanostructures (blue triangles) preferentially grow along one of the two in-plane dimensions (i.e. highly anisotropic).
For the directed deposition (red circles) the in-plane growth is notably isotropic (black dashed line) until the grain size reaches the tip diameter ($\sim$ 50 nm, grey dashed line), at which point the grain width (in the direction perpendicular to the writing direction) saturates. It is worth mentioning that the datapoints for the largest major axes consider a more or less fully coalesced line (1 μm). As such, the initial stage of the grain evolution in directed deposition resembles that for the higher concentration (green data points). In this case, the in-plane growth is clearly isotropic as the two in-plane dimensions are approximately the same as the grains grow. It is important to note however, that the slope in Fig. 3-5a does not change when fitting only to those isotropic grains (using the grains for which $A < D_{tip}^2 = 2500$ nm^2, yielding a slope of 1.14)

3-6 Conclusion

From our results it appears that the directed growth occurs in 2 main steps; i) isotropic in-plane growth, confined to the tip dimensions, ii) decreased in-plane, and increased out-of-

plane growth.
We believe that despite the low ion concentration, the close proximity of the tip counter electrode to the substrate facilitates a faster deposition rate compared to the non-directed case with the same electrolyte conditions. This is evidenced by the fact that a much longer deposition time was required to grow the non-directed sample compared to the lines (factor 30 for the images in Fig. 3-2), despite yielding smaller islands. On the other hand, the fact that the vertical growth is hampered in the directed case as compared to growth from a non-dilute electrolyte, we believe is likely due to the restricted ion access by the tip itself.
The shape of the grains in directed growth and their time evolution is remarkably close to that in the macroscopic EC-cell, which we confirm to be mainly CuO. It therefore seems quite possible that the directed deposition also consists of copper oxide species. This can occur through direct copper deposition and subsequent oxidation, especially considering the reaction at the tip, which is expected to produce oxygen locally through the oxidation of water. For the deposition of pure copper it might therefore be interesting to deaerate the electrolyte and/or facilitate a different oxidation reaction.

3-7 Methods

Sample Fabrication and electrodeposition
For the direct writing, we use a 2-electrode configuration consisting of an insulated AFM tip, except for a Pt coated apex [110], and the metal substrate. The potential is controlled by either a CH760E or a BioLogic SP-300 potentiostat. The substrate electrode consists of a silicon substrate coated with a chromium adhesion layer and a gold top layer contacted from the top. Electrodeposition was done from 100 mM and 1 μM aqueous (MilliQ®, 18.2 MΩ·cm) copper sulfate solutions ($CuSO_4 \cdot 5H_2O$, 99.995% from Sigma-Aldrich). The low concentration electrolyte was prepared before every experiment from a 1 mM CuSO4(aq) stockpile and diluted (1000x) using fresh MilliQ water. Due to the hydrolysis of $CuSO_4$, the solution is more acidic for the higher salt concentration (pH $\sim$ 4 vs. 6). The nondirected deposition from the dilute electrolyte was done in an electrochemical cell outside of the AFM setup, with an exposed electrode area of 1.5 cm^2 using a coiled copper wire as the counter electrode.

Atomic force microscopy
AFM measurements were performed using a Bruker Dimension Icon AFM. The protocol for the directed nanoscale writing is explained in depth in the previous chapter. The in-situ images as shown in Fig. 3-2b are obtained with a ScanAsyst-Fluid+ probe (Bruker, nominal tip radius 2 nm), in PeakForce tapping mode. Ex-situ images were obtained with a ScanAsyst-Air probe (Bruker, nominal tip radius 2 nm). Ex-situ images were also used for the directed nanoscale deposition as the SECM probe used for the deposition was relatively large compared to the features of interest (nominal radius 25 nm).

AFM data treatment
AFM images were treated by removing the polynomial background (first or second order) and removing image defects by aligning rows or removing scars using the Gwyddion software [116]. The shape analysis is done using height thresholding and considering the pixels underneath the resulting mask. Projected area and bearing volume (Fig. 3-1) are obtained using a height threshold of 2 nm ($\sim$ 3x the sample roughness) for every written line. The masks in Fig. 3-2 are obtained by manually identifying the islands and combining that with a height

threshold, the histogram was then obtained using the slope distribution tool, with inclination maps constructed through the arithmetic operation as mentioned in the main text (eq. 3-1) . Similarly for the data in Fig. 3-5 the area of interest was combined with height thresholding after which the grain correlation tool was used to get projected area vs. volume and major vs. minor axis of the equivalent ellipse (the numbers in Fig. 3-5b are multiplied by 2 to reflect diameters rather than radii).

XPS

XPS spectra were acquired using a Scienta Omicron HiPP-3 analyzer and a monochromatic Al kα source operating at 20 mA emission current. The base pressure was $\sim$ 2x10^{-9} mbar, and the operating pressure was $\sim$ 5x10^{-9} mbar. Survey and high-resolution spectra were acquired at pass energies of 500 eV and 100 eV, respectively. Data analysis and quantification were performed using KolXPD from Kolibrik.

Chapter 4

Pulsed electrochemical scanning probe nano-lithography

This chapter considers the use of short voltage pulses to confine electrochemistry by means of time,- and distance dependent charging of the interface. We demonstrate the working principle with the nano-confined electrodeposition of cobalt. Furthermore, we interpret and predict the achievable resolution in terms of fundamental properties of the electrolyte. The presented results indicate the detrimental role of protons for the localization of the electrical pulse, and therefore have important consequences for the use of aqueous electrolytes in nanoscale deposition using this method.

4-1 Introduction

The previous chapters demonstrated a novel method for localized electrodepostion with a scanning probe. An early strategy in confining electrochemistry to the nanoscale however, has been the use of ultrashort potential pulses [61]. The working principle is outlined in reference [64] and depicted schematically in Fig. 4-1a. The authors consider an equivalent electrical circuit between a scanning probe and the substrate, which consists of the electrical double layer (EDL) capacitance at both electrodes in series with a resistor representing the solution as described in chapter 1. As such, the system contains many parallel RC-circuits that represent the current paths from the tip to different positions on the substrate, with the associated charging time being different for parts of the substrate further away from the probe by means of the increased solution resistance. By applying a short potential pulse to the probe, the interface is only significantly polarized close to the probe, as illustrated in Fig. 4-1b. In fact, due to the exponential dependence of the Faradaic current on the interface potential from Butler-Volmer kinetics (see section 1-1), even modest potential differences near the probe result in sharp profiles for the electrochemical rate.

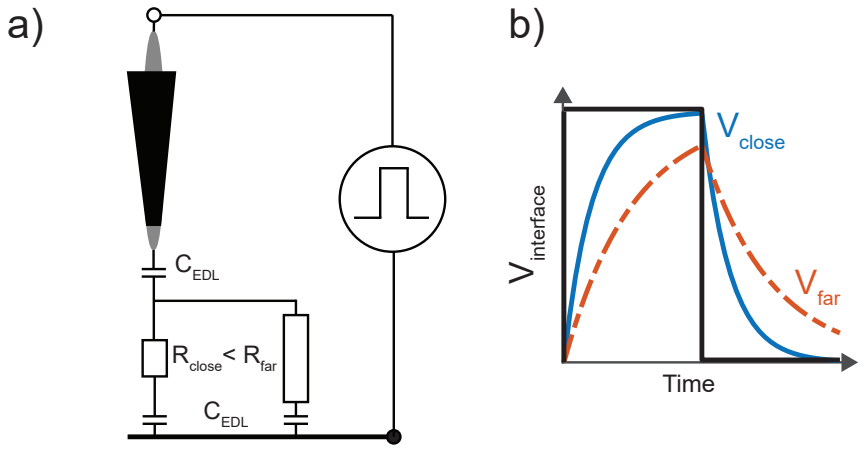

Figure 4-1: a) Illustration of the mechanism for electrochemical localization. By applying a potential pulse to the probe, the EDL at the substrate will charge more quickly close to the probe due to the lower path resistance through the solution. Adapted from reference [64]. **b)** Representation of the (partial) charging of the interface during a potential pulse (black line), for a tip-substrate path that is short (low resistance, blue solid line), or long (high resistance, red dash dotted line).

The main parameters influencing the electrochemical resolution therefore appear to be the solution resistance, and the pulse time. As such, electrochemical etching (machining) of features down to $\sim$ 200 nm has been demonstrated by using pulses of 500 ps [68]. While the mechanism has been expected to enable local electroplating by simply reversing the polarity of the pulse, this has proven to be more elusive and we did not find a clear demonstration in literature [61, 66, 134].
In this chapter we will consider a description analogous to the RC model to predict the attainable resolution, and demonstrate nanoscale deposition using short voltage pulses. Following the work of Bazant et al. [26] we consider the time constant τ_C as introduced in section 1-2, which emerges as the RC time for a simple electrochemical system of 2 parallel plates with a 1:1 electrolyte when a potential is suddenly applied, and has been formulated as the charge relaxation of the diffuse layer through bulk electrolyte conduction [27].

$$\tau_C = \frac{\lambda_D L}{2D} \quad \longrightarrow \quad L_{\tau_C} = \frac{2D\tau_{pulse}}{\lambda_D} \tag{4-1}$$

Where λ_D is the screening length, L the electrode separation, and D the diffusion coefficient. For the purpose of predicting the achievable charging distance, the equation is rewritten to yield the electrode separation L_{τ_C}, which then represents the maximum distance where the interface charges to e^{-1} of the applied pulse for a given time τ_{pulse}. Importantly, equation 4-1 expresses the expected distance over which significant charging occurs in terms of fundamental constants of the electrolyte, namely the diffusion coefficient, the concentration, and the dielectric constant of the solvent; $L_{\tau_C} \propto D\sqrt{\frac{C}{\epsilon}}$, using the expression for λ_D as given by equation 1-4 in section 1-2.
Along this line, dimethyl sulfoxide (DMSO) based electrolytes have been used previously as a means to decrease the ion diffusion coefficient and therefore increase the resolution with

respect to aqueous solutions for the localized etching of gold [135, 136]. We use this approach of DMSO as a solvent to demonstrate the nanoscale deposition of cobalt using short voltage pulses, with feature sizes below 100 nm. Furthermore, we argue that the difficulties in confining ultrashort pulses in aqueous electrolytes are ultimately due to the high diffusion coefficient of protons, which we confirm by a comparison with literature and observe experimentally in the greatly enhanced writing resolution as compared to aqueous electrolytes.

4-2 Comparing diffuse layer charge relaxation to machining literature

First, we compare the resolution predicted from the diffuse layer charge relaxation with that reported in nano/micro-machining resolution literature for the electrochemical etching of holes or trenches in metal electrodes. To assess the extent of the charging process, we consider works that have a long total machining time, so that the etching process is expected to be complete, i.e. longer machining times would not result in wider etched features. By considering these terminated processes, we assume that the width of the etched features corresponds to the farthest distance at which the double layer is sufficiently charged to thermodynamically allow the oxidation reaction at the substrate, and the corresponding reduction reaction at the tool/tip.
It should be realized that τ_C corresponds to the RC time, after which the interface is charged to e^{-1}, or $\sim$ 63 % of the applied pulse. As we are interested in the maximum distance at which the interface is charged to a certain potential for a given pulse time, this distance should therefore be corrected by the time-dependent charging.
This is illustrated in Fig. 4-2a for the case where the required potential is reached before the interface is charged to 63 % of the applied pulse. As such, the reaction can occur for pulse widths below τ_C. The maximum distance L_{max} at which the reaction will still proceed is then determined by the shortest pulse of time t_{min} that results in charging of the interface to V_{req}. We solve for the minimum time, t_{min}, for a certain pulse height V_{pulse} in terms of τ_C, obtained from the time dependent charging of a capacitor $V(t)$; $V_{req} = V(t_{min}) = V_{pulse}(1 - e^{-t_{min}})$. For all considered works this yields t_{min} in units of τ_C, which then represents the required charging time to allow the etching reaction to occur for the employed pulse height V_{pulse}. This minimum time is then used in equation 4-1 to obtain the etching resolution.

The predicted resolution is compared with that shown experimentally in the works of Schuster et al. [64], De Abril et al. [66], and Kock et al. [68], which include different metals (Ni, Cu), electrolyte concentrations (1-200 mM), and pH (1-3). Importantly, we consider the diffusion coefficient of protons (D = $1{\cdot}10^{-8}\frac{m^2}{s}$ [90]), as all works use acidic electrolytes. Following the discussion in the previous paragraph, we define the required potential, V_{req}, as the sum of the potential change required for both the tool and sample, from the respective rest potentials, to reach the corresponding reaction standard potentials. We consider the hydrogen evolution reaction (HER) to occur at the tool/tip, with a pH-dependent potential E_{HER} = 0 - 60 mV*pH, and the metal oxidation at the substrate, where we use the potentials E_{Cu} = 340 mV, and E_{Ni} = 80 mV [137] for copper and nickel, respectively, with potentials vs. the standard hydrogen electrode (SHE). All parameters used to determine the required charging time are shown in SI Table 4-1.
Fig 4-2b shows the results, with open symbols indicating the literature values, and closed

connected symbols the predicted resolution. The figure shows that the values calculated from equation 4-1 match those obtained in literature rather closely, in particular for the shortest pulse times, and within a factor ~ 2 for all datapoints. Here it should be noted that most data displays the expected linear dependence between pulse time and etching resolution. Furthermore, the calculated values capture the concentration dependence that is observed experimentally, which in the model results from a decrease in the screening length. As such, we propose that considering τ_C as the governing parameter for localized electrochemistry provides a handle to quantitatively predict the extent of the reaction in terms of fundamental constants of the electrolyte, being the screening length and diffusion coefficient.

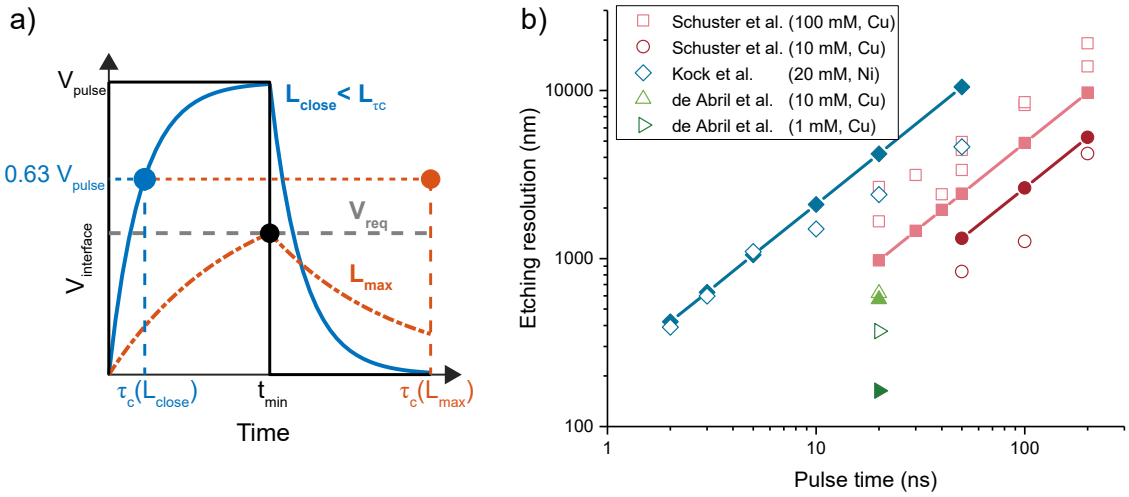

Figure 4-2: a) Illustration for the charging of the interface at the maximum etching distance L_{max} (red dashed curve). As the minimum potential required for the reaction to proceed is less than 63 % of the pulse height, L_{max} is obtained at the shortest pulse time t_{min} where the interface just charges to the required potential. The charging curve for a distance that is shorter than the distance at which the interface charges to 63 % of the pulse height for a pulse of width t_{min} (L_{τ_C}) is shown for comparison (blue curve) **b)** Comparison of the etching resolution reported in literature (open symbols), with that predicted by diffuse layer charge relaxation (closed connected symbols). The results seem to be in good quantitative agreement within a factor 2 for all datapoints, considering different concentrations and electrolytes. The works considered are references [64, 66, 68].

4-3 Nanoscale electrodeposition with an STM

The previously considered works focused on localized etching. In principle, the reverse process of local deposition by reversing the polarity of the pulse is expected to be equivalent. We conduct deposition experiments with an electrochemical scanning tunneling microscope (STM) in a 4-electrode setup under ambient conditions. The STM is coupled to both a bipotentiostat, and a pulse generator, as is schematically shown in Fig. 4-3a. As such, the potential of the tip and substrate can be controlled independently, which is critical for the operation of the tunneling feedback mechanism that requires a potential difference between the tip and the substrate. As the feedback current is typically set to ~ 1 nA, STM tips are coated with an insulating wax to decrease the exposed area and minimize parasitic Faradaic

current along the length of the probe.
The connection to the tip is switched between the potentiostat and the pulse generator through a relay, where the connections of both are such that potential control over the tip is maintained when the relay is switched (the tip connection is at measurement ground in both cases). The deposition protocol is as follows; i) scanning of the surface, ii) withdrawing the tip by a certain 'dwell distance', iii) switching the relay to the pulse generator and sending a pulse train into the tip, iv) switching back the relay to the potentiostat. A detailed description of the setup can also be found in reference [51]
The electrochemical cell consists of 4 electrodes, where both the counter electrode and quasi-reference electrode (QRE) are gold wires, the substrate is single crystal (111) Au, and the probes were either commercially available Pt-Ir tips, or an electrochemically etched Pt wire. Following the discussion in section 4-1, we use DMSO as a solvent to decrease the diffusion coefficient of ions in solution with either a 50 mM or 500 mM $CoSO_4$ electrolyte.
Fig. 4-3b shows a cyclic voltammogram (CV) of the substrate in 500 mM $CoSO_4$ (DMSO). The reduction reaction with an onset at $\sim$ -900 mV is associated with the deposition of cobalt, as confirmed by STM imaging. The cobalt oxidation is connected to the oxidation wave starting at $\sim$ -400 mV (blue curve), as confirmed by the absence of the oxidation wave when stopping the scan at higher potentials (grey dashed curve). The reduction reaction at $\sim$ -300 mV is thought to be associated with oxygen present in the electrolyte and was found to disappear when the solution was deaerated.
An important consideration for the electrolyte is the reversibility of the deposition reaction. As the reduction/oxidation of Co are separated in potential by a few hundred mV, this provides an electrochemical window where the substrate potential can be fixed as to both prevent global deposition on the substrate to occur, while also preventing dissolution of the deposited structures. The tip and sample rest potentials are depicted in Fig. 4-3b, where the tip has to be kept at a different potential with respect to the substrate to enable the tunneling current feedback.

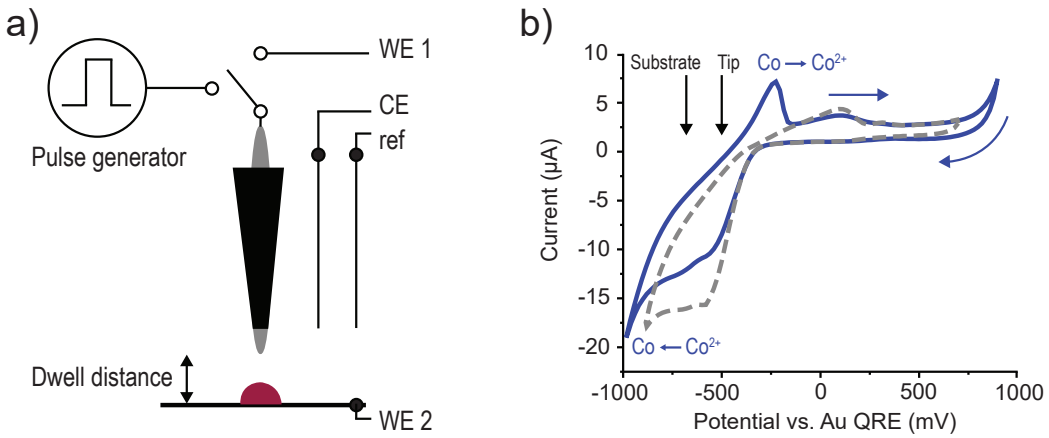

Figure 4-3: a) Schematic representation of the electrochemical STM setup, connected in a 4 electrode configuration. Local deposition is done by lifting the tip and switching the connection to the tip from the bipotentiostat to an external pulse generator. **b)** Cyclic voltammetry on the Au (111) single crystal substrate in 500 mM $CoSO_4$ (DMSO). The reduction (~ -900 mV) and oxidation (~ -400 mV) potentials for Co^{2+}/Co are indicated. The tip and substrate potential are kept apart to enable scanning feedback, where the substrate potential is kept within the electrochemical window of cobalt. The scan rate is 100 $\frac{mV}{s}$.

In-plane writing

We demonstrate the possibility of in-plane nanoscale writing using this method. Fig. 4-4a displays the topography of 500 nm lines written at different dwell distances (10, 20, 30, 60 nm) from 500 mM $CoSO_4$ (DMSO). The lines are written with 10 consecutive pulse sequences at positions spaced 50 nm apart, as indicated by the red dots in the first image. For every point the tip finds the surface, is retracted by the dwell distance, and a pulse train is sent. The pulse train consists of 2000, 5 V pulses of 100 ns, with a 10 μs period. The tip/sample potential is kept at -500/-700 mV vs. Au QRE. To reduce the total charging required for the tip, the low level of the pulse is set to 1 V (i.e. 500 mV vs. Au QRE).

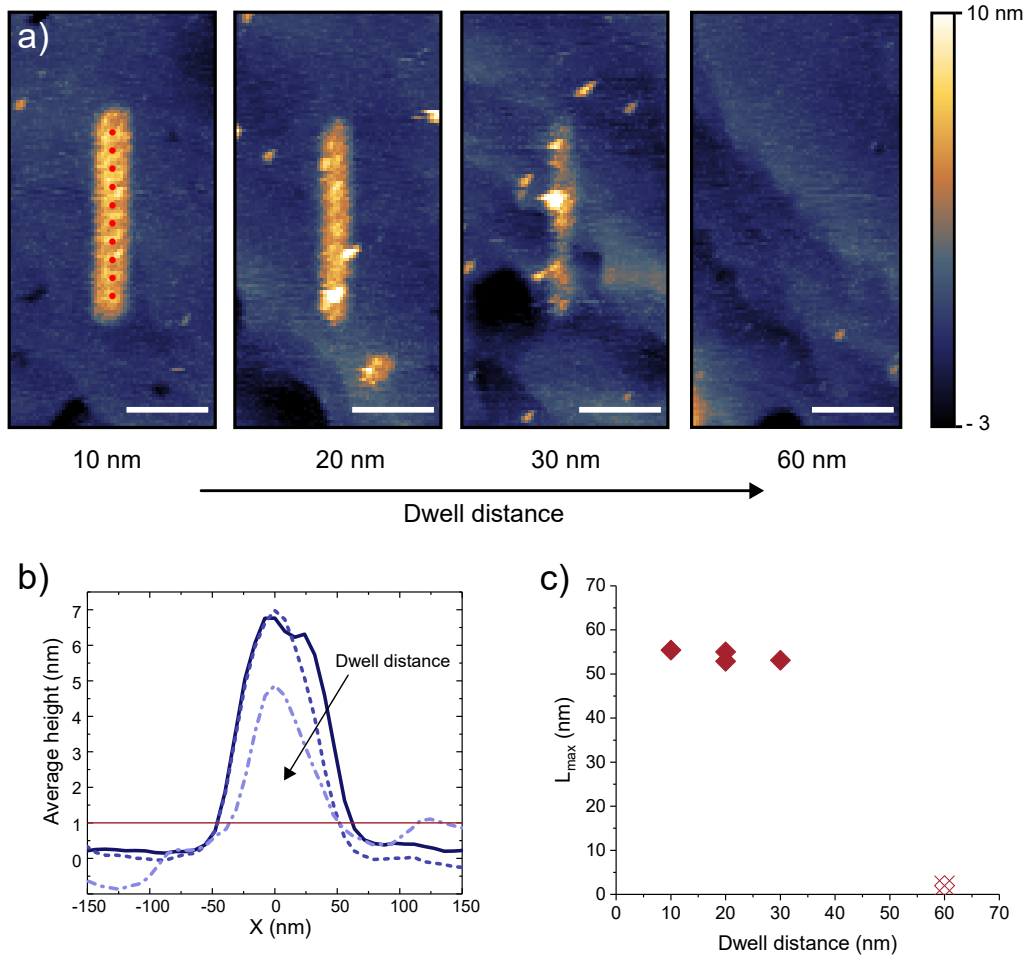

Figure 4-4: a) STM topography images of cobalt lines written at different dwell distances by 10 consecutive pulse sequences 50 nm apart (red dots in first panel). The scale bars are 200 nm. **b)** Profile averaged along the length of the lines in a) for different dwell distances (solid, 10 nm, dashed, 20 nm, dash-dotted, 30 nm). The width of the lines is defined as the region where the average profile is higher than 1 nm (red line). **c)** L_{max}, as defined in the main text as the shortest path from the tip to the edge of the deposit for different dwell distances.

Figures 4-4b and 4-4c illustrate the robustness of the localization by considering the maximum writing distance from the average profile of the written lines as $L_{max} = \sqrt{Dwell\ distance^2 + \frac{w}{2}^2}$, with w the width of the deposit taken as the average height above 1 nm (red line in Fig. 4-4b), where it should be noted that the pixel resolution of the images is $\sim$ 8 nm. L_{max} is found to be constant at $\sim$ 55 nm, as expected when keeping the pulse parameters the same. Interestingly, this maximum is confirmed by attempting to write at a dwell distance of 60 nm, where no deposition was observed.

Charging distance as a function of pulse time

We systematically investigate the maximum distance over which deposition occurs as a function of pulse width. The employed measurement routine aims to consider only the shortest path from tip to sample, rather than attempting to determine the maximum deposition distance from the shape of the deposit, which can not always be unambiguously determined from the resulting deposition (see SI 4-6). We believe that this uncertainty can be due to the shape/quality of the STM tip, or possibly a high nucleation overpotential for the deposition. The experimental procedure is therefore as follows and is illustrated in Fig. 4-5a: The tip is lifted by a certain dwell distance after which the pulse width is increased until deposition is observed. The dwell distance is then considered as the maximum distance for that pulse time. This sequence is then repeated for the next dwell distance. The presence of deposition is therefore reduced to a binary qualification (SI 4-6), where deposition 'is' or 'is not' observed for a certain pulse width at a given distance. To eliminate effects of sample inhomogeneity, the potential of the substrate is lifted above the cobalt oxidation potential after deposition is observed. In all cases the deposits are then dissolved, partially confirming that they consist of Co, and allowing an experimental sequence to be done on the same spot.
The result is depicted in Fig. 4-5b, showing the minimum required pulse width for a certain dwell distance, with the error bars given by the longest pulse where no deposition was observed (error is 10 ns for the triangular datapoints). The pulse train consists of 10^4, 2.5 V pulses, with a period of 10 μs for all pulse widths. A low duty cycle is used to allow the system to settle between pulses. The dashed lines are linear fits to the data. All data is obtained from 50 mM $CoSO_4$ (DMSO), with the different symbols indicating different STM tips (Pt for triangles, PtIr for diamonds and squares). SEM images of the tips are displayed at the end of their respective fitted curves. (images of the tip apex are provided in SI 4-7). The tip/substrate rest potentials are -700/-900 mV (triangles, squares), and -850 mV/-1050 mV (diamonds).
The solid lines correspond to L_{τ_C} as a function of pulse width as obtained from equation 4-1. We use $\epsilon_{DMSO} = 46.7$ to obtain λ_D, and plot L_{τ_C} for i) a diffusion coefficient of Cobalt in DMSO that is estimated to be $5{\cdot}10^{-10}\frac{m^2}{s}$, based on measurements of $CoCl_2$ in water [138] and scaled with the viscosity η of DMSO ($\eta_{water} : \eta_{DMSO} = 1{:}2$, with $D \propto \frac{1}{\eta}$), and ii) for a diffusion coefficient of $7{\cdot}10^{-11}\frac{m^2}{s}$, found in literature [139]. The difference is expected to be due to the solvation of the Cobalt ions with either water or DMSO. As our experiments are carried out under ambient conditions, and the DMSO is hygroscopic, the actual diffusion coefficient is expected to be in between these two values [136]. As such, this indicates the distance to which the interface is polarized to at least e^{-1} times the pulse height. Considering a required polarization of $\sim$ 1500 mV, a slightly shorter required charging time of $\sim 0.9 \cdot \tau_C$ is expected for the 2.5 V pulses.

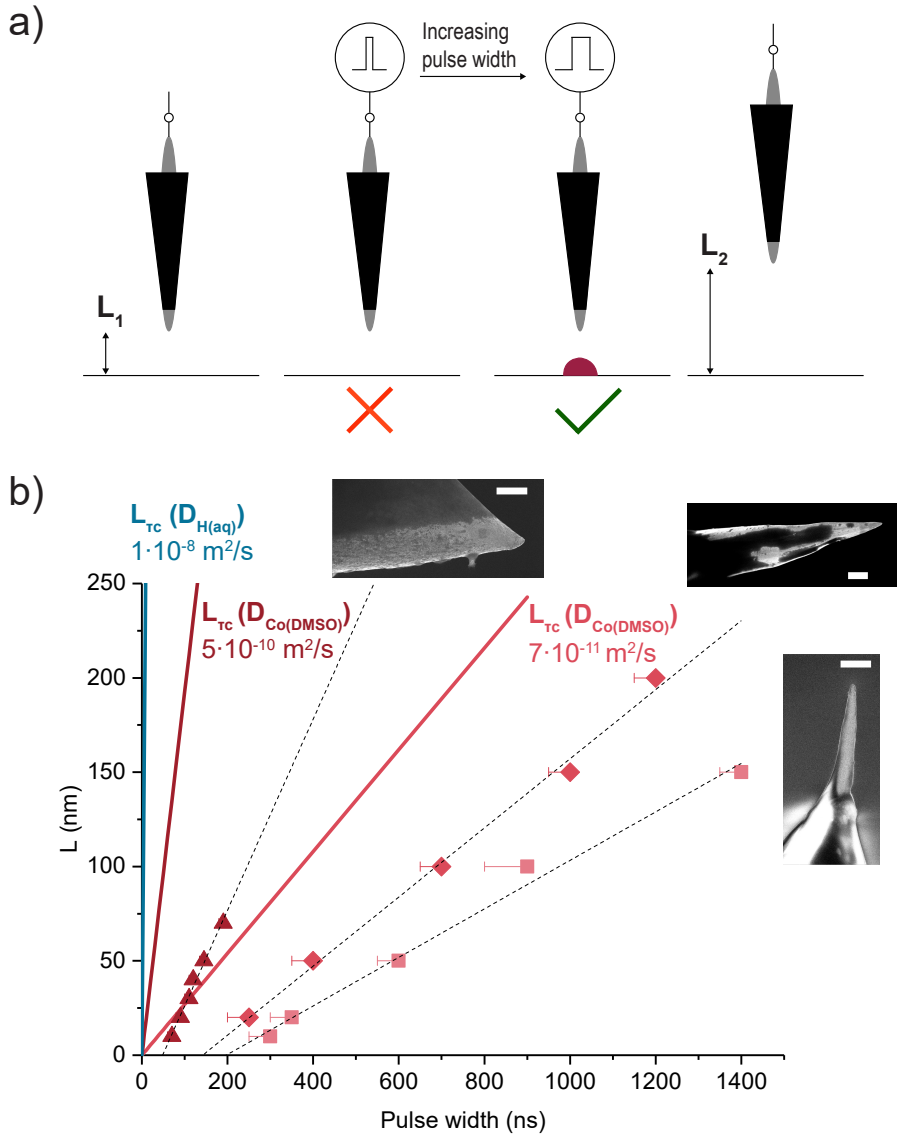

Figure 4-5: a) Illustration of the deposition protocol to determine the maximum distance. Deposition is attempted at a certain distance L_1 by increasing the pulse width until deposition is observed. The surface is scanned after every pulse train with a given pulse width. Once deposition is observed, the sequence is repeated at a higher distance (L_2). **b)** L vs. Pulse width, obtained with the procedure in a) in 50 mM $CoSO_4$ (DMSO). The datapoints indicate the minimum pulse width at which deposition is observed, with the error bars indicating the maximum pulse width without deposition. The different symbols indicate different STM tips, as shown next to the linear fits to the data (scale bar 2 μm). The solid lines represent L_{τ_C} as obtained from equation 4-1 from 50 mM aqueous and DMSO electrolytes.

From the figure it can be seen that that the maximum deposition distance is linear with the pulse width, as expected from equation 4-1, and that all datapoints fall within the region spanned by L_{τ_C}. As the required charging time for this pulse height is close to $1{\cdot}\tau_C$, the result is expected to lie close to the L_{τ_c} line. It is worth mentioning that we observed deposition in aqueous electrolytes (50 mM $CoSO_4$ (aq), pH $\sim$ 4) with 10, and 20 ns pulses at

dwell distances of 200, and 500 nm, respectively, which is only allowed by the diffuse layer relaxation model when accounting for the fast diffusion of protons. This is shown by the blue solid line, for which L_{τ_C} is obtained for an aqueous electrolyte, with $\epsilon_{H_2O} = 80.1$ and using a diffusion coefficient of protons of $1{\cdot}10^{-8}\frac{m^2}{s}$ [90] for comparison.
For the observed linear relation between pulse time and deposition distance. there are three main deviations from that given by the diffuse layer relaxation model; i) the slope is smaller for all tips compared to that for a diffusion coefficient of $D = 5{\cdot}10^{-10}\frac{m^2}{s}$ and for the sharpest tips (diamonds and squares) it is also smaller than the slope for $D = 7{\cdot}10^{-11}\frac{m^2}{s}$, ii) there is an offset for crossing of the x-axis, or time delay for the onset of deposition, iii) the slope and time delay are tip dependent.
It should be realized that the expression for τ_C assumes an instantaneously applied potential difference between two parallel electrodes. The fact that we observe a slower response in the form of longer required pulse times may therefore arise from parasitic capacitance along the STM tip that perturbs the pulse arriving at the apex. It has been demonstrated recently that machining resolution can be improved for a given pulse time by introducing an additional capacitor that slows down the charging [140]. This explanation of a perturbed pulse is supported by the observation that the slope decreases for sharper STM tips (SI 4-7), where sharply curved metal surfaces are expected to have a higher capacitance due to the 'lightning rod' effect.
It is harder to explain the offset for crossing the x-axis. Strikingly, we observe that the linear fits to the three datasets result in the same value for the intercept with the y-axis (at -25 nm $\pm$ 1 nm, not shown in the Fig 4-4). It is at this point unclear whether this is a coincidence, as the negative distance value does not not seem to have a straightforward physical meaning.

4-4 Conclusion

This chapter demonstrated the nanoscale electrodeposition of cobalt from a DMSO solution, using short voltage pulses applied to an STM tip. A framework was presented to interpret the achievable resolution in terms of fundamental properties of the electrolyte. This has implications for the use of aqueous electrolytes in nanoscale pulsed deposition, as the high diffusion coefficient of protons forces the use of extremely short pulses, which might not be feasible experimentally. We expect that this method can be extended to other materials, where a second important consideration is the reversibility of the metal deposition as to enable the substrate to be held at a suitable resting potential [137, 141].

4-5 Methods

Solution preparation
Solutions were prepared in glass vials cleaned in acid piranha and washed with MilliQ® water. Solutions were prepared with $CoSO_4{\cdot}\ 7H_2O$ powder (99.999 %, Alfa Aesar, Germany) in dimethyl sulfoxide (DMSO, analytical reagent grade, Fisher Scientific UK).

Tip preparation
PtIr STM tips were purchased from NaugaNeedles (NN-USPtIr-W250, nominal radius 25-50

nm). An electrochemically etched Pt wire tip was used for the red triangles in Fig. 4-5. All tips were coated with a thermoplastic wax (Apiezon, wax W).

Electrochemical cell
The electrochemical cell was made from polychlorotrifluorethylene. The sample was Au single crystal ((111)-out-of-plane < 1 %, 99.999 % purity, Mateck, Germany). For the experiments in Fig. 4-5 (diamonds, squares) the sample was cleaned by cyclic voltammetry in water with low amounts of H_2SO_4 prior to the experiment.

Electrochemical pulsed STM electronics
Measurements were conducted with an STM (Cypher-AFM in STM-mode, Asylum Research, USA). Potentials were controlled with a bipotentiostat (PGUmicro, IPS, Germany), and pulses were supplied by an external pulse generator (2x81111A, Agilent, USA). A detailed description of the setup can be found in reference [51].

4-6 Supplementary information

SI-1 Values used for predicting etching resolution

Table 4-1: Parameters used for the predicted resolution of the systems used in literature.

	Schuster et al [64]	Kock et al. [68]	De Abril et al. [66]
Material	Cu	Ni	Cu
charge number (z)	1.1	1	1
	1.5		1
Tip/substrate pot. (mV)	200/0 vs. Cu^{2+}	-5/-150 vs. Ag/AgCl	100/-100 vs. Cu^{2+}
Pulse Height (V)	1.6	2.2	3.2
pH	1	1	2
	2		3
E_{ox} substrate (mV)	0 vs Cu^{2+}	-150 vs. Ag/AgCl	0 vs Cu^{2+}
E_{red} tip (mV)	-400 vs. Cu^{2+}	-290 vs. Ag/AgCl	-460 vs. Cu^{2+}
	-460 vs. Cu^{2+}		-520 vs. Cu^{2+}
Total potential (mV)	600	285	660
	660		700
Required time in τ_C	0.47	0.14	0.23
	0.53		0.255

Table 4-1 lists the parameters used in predicting the etching resolution in aqueous systems. As explained in the main text the required charging time is scaled in terms of τ_C by solving $V_{Total} = V(t) = V_{PulseHeight}(1 - e^{-t})$. We further use a diffusion coefficient of $1{\cdot}10^{-8}\frac{m^2}{s}$ for protons [90]. The charge number z used in the calculation for λ_D is included, as the work of Schuster [64] uses a varying composition of the electrolyte.

SI-2 Example of determining deposition distance

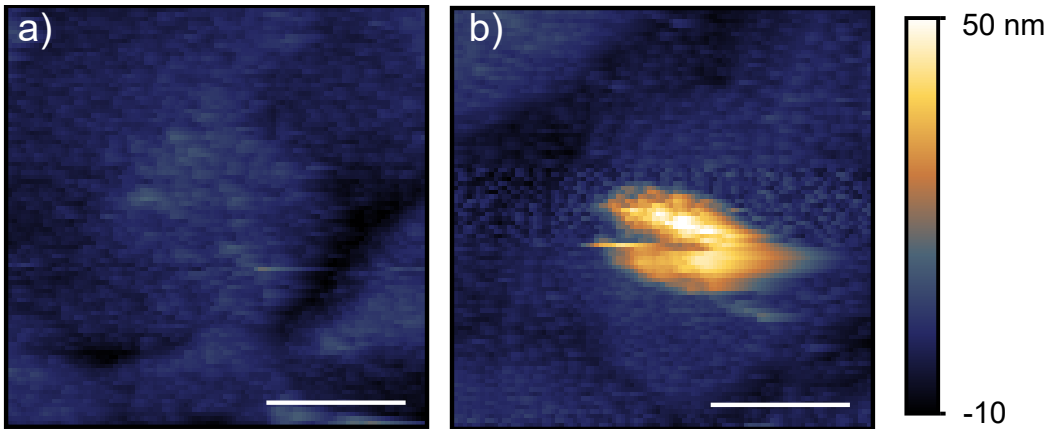

Figure 4-6: Example STM topography images of the qualitative determination of deposition as used for Fig. 4-4. **a)** Deposition at 20 nm dwell distance with 300 ns wide pulses. **b)** Deposition at 20 nm dwell distance with 350 ns wide pulses. From this procedure we take the distance over which deposition can occur to be 20 nm for the 350 (± 50) ns pulse, where we attribute the much wider deposition profile to the shape of the tip. The scale bar is 500 nm.

SI-3 SEM images of STM tips at higher magnification

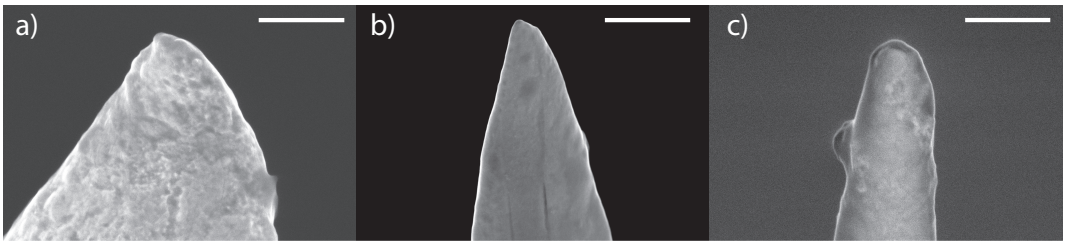

Figure 4-7: SEM images of the tip apex for the STM tips used in Fig. 4-4, used for the data as depicted by the **a)** triangles, **b)** diamonds, and **c)** squares. The scale bar is 500 nm.

Chapter 5

Potential dependent adhesion mapping

This chapter investigates the mechanical interaction between a gold substrate and an AFM tip under different electrochemical conditions by means of continuous force spectroscopy. In particular, we focus on the force of adhesion as a metric for the potential-controlled state of the surface. We present adhesion maps of the surface that are both spatially inhomogeneous and depend on the substrate electrochemical potential. As such, this can provide a way to map and spatially resolve surface processes *in-situ*.

5-1 Introduction

Electrochemical reactions are governed by the interfacial region near the electrified surface, which includes both the specific adsorption of ions at the substrate, and the potential distribution between the solid and the liquid. An accurate picture of this region is therefore very relevant for any electrochemical process [142]. A tool capable of probing the solution structure with high resolution is the electrochemical surface force apparatus (EC-SFA), which can provide a force profile when approaching a potential-controlled surface with sub-nanometer precision of the separation distance [143–145]. A disadvantage of the SFA is the lack of spatial information however, considering the importance of sample inhomogeneity for the electrochemical behavior [119, 146, 147], down to the single atomic level [148, 149].
The atomic force microscope (AFM) therefore provides an attractive alternative for force spectroscopy with spatial resolution [150, 151], and has been used in recent years for mapping of the electrical double layer (EDL) under different conditions [103, 107, 152]. Furthermore, potential control can be added to both the substrate and the tip [153], as has been done in efforts extending kelvin probe force spectroscopy to electrolyte systems, which also provides information on charging dynamics [27, 100, 108].
In this chapter we use a similar method of force spectroscopy, but rather focus on the force of adhesion between an AFM tip and a substrate under potential control, which we use to map the interaction spatially. This has garnered interest in the past [154–156], however to the best of our knowledge voltage dependent adhesion studies have been mainly limited to

single spots on the substrate.
The work of adhesion required to pull the tip from the sample can most broadly be understood in terms of the energy difference between creating a substrate-liquid and tip-liquid interface, and the original tip-substrate interface given by [156],

$$W_{adh} = \gamma_{SL} + \gamma_{TL} - \gamma_{TS} \tag{5-1}$$

With W_{adh} the work of adhesion, γ the interfacial free energy, and the subscripts S,L,T, indicating substrate, liquid, tip, respectively. The work of adhesion therefore comprises multiple physical effects,

$$W_{adh} = W_{VdW} + W_{solv} + W_{chem} + W_{EDL} \tag{5-2}$$

Where the right hand side denotes the work due to different interaction forces. As such, the adhesion holds information on Van der Waals (VdW), solvation (solv) [106, 157], specific chemical interaction (chem) [158], and the electric double layer and other electrostatic forces (EDL) [155]. The work of adhesion can be obtained directly from the pull-off force by using a proper model for the contact mechanics [144, 159]. As such, the adhesion force also contains information on the different interaction forces, which can all possibly be influenced by means of potential in an electrochemical system [156].
Here, we present spatially resolved adhesion measurements on a gold surface under potential control, in a Na_2SO_4 electrolyte. We observe a pronounced potential dependence in the adhesion which is inhomogeneously distributed over the substrate, and as such holds information on the local state of the surface.

5-2 Adhesion mapping with potential control

The experimental setup is shown schematically in Fig. 5-1a, and consists of an electrochemical atomic force microscope (AFM), using a Pt coated tip (Peakforce SECM, Bruker, nominal tip radius $\sim$ 25 nm) in a 3-electrode configuration. The counter and reference electrode are a circular Pt wire and a Ag/AgCl reference, respectively. The substrate is gold coated silicon with a titanium adhesion layer (50 nm Au + 5 nm Ti), which we observe to have a pronounced (111) orientation from X-ray diffraction measurements on a representative sample as shown in SI 5-4.
Experiments are done in an aqueous Na_2SO_4 electrolyte. The electrochemical behavior of the system is shown by the cyclic voltammogram (CV) in Fig. 5-1b, for 10 mM Na_2SO_4 at a scan rate of 5 $\frac{mV}{s}$. The potential-dependent surface processes of sulphate containing electrolytes on single crystal gold electrodes have been extensively characterized [160, 161]. In particular, the work in reference [160] illustrates a process of progressive sulphate adsorption on a gold (111) electrode as the potential is increased over the range $\sim$ 0.3 - 0.8 V vs. Ag/AgCl at pH 1. The adsorbed sulphates are found to be mobile on the surface up to the end of this range at $\sim$ 0.8 V vs. Ag/AgCl, when they form an ordered overlayer. From these works we interpret the oxidation wave at 0.5 V vs. Ag/AgCl as the onset of sulphate adsorption, with the reduction on the retrace being the opposite process. Importantly, the onset potential at 0.5 V vs. Ag/AgCl is also associated with both the point of zero charge (PZC) of the gold

electrode, and a reconstruction of the gold surface from (p x $\sqrt{3}$) to (1 x 1) [160]. Finally, we attribute the oxidation at higher potentials to the onset of gold oxidation. As such, we focus on the potential range between 0.2 - 0.8 V vs. Ag/AgCl, where we consider the main processes to be double layer charging for the region 0.2 - 0.4 V and progressive sulphate adsorption at potentials 0.4 - 0.8 V.

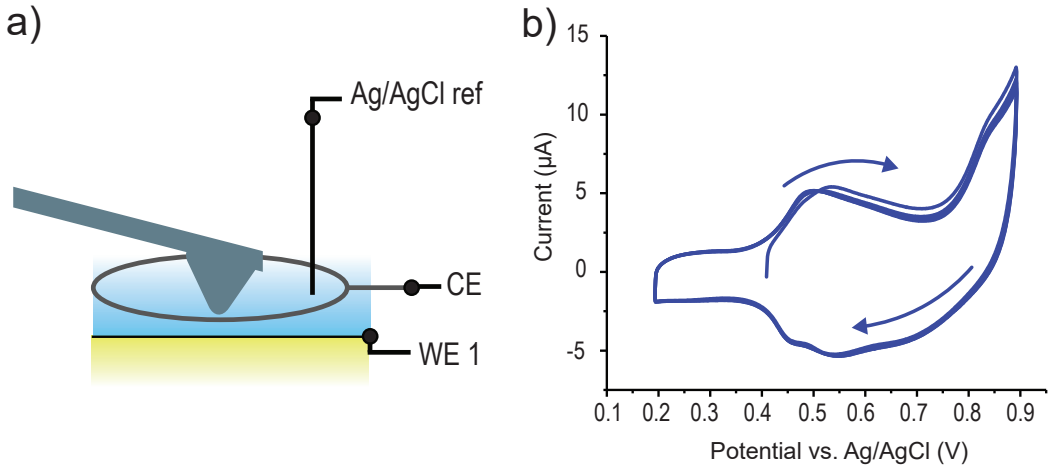

Figure 5-1: **a)** Schematic representation of the electrochemical AFM setup. The system is configured in a 3-electrode configuration. **b)** Cyclic voltammogram in 10 mM Na_2SO_4. The waves at $\sim$ 0.5 V are associated with sulphate (de)adsorption, with the oxidation of gold starting above 0.8 V. The scan rate is 5 $\frac{mV}{s}$.

Adhesion force mapping is done by operating the AFM in PeakForce tapping mode. In this mode, the cantilever is driven in a sinusoidal motion, where the tip is continuously executing a force curve in a tapping fashion. The frequency of oscillation is set to 122 Hz, and the cantilever deflection is sampled using High Speed Data Capture (HSDC) at a rate of 500 kHz. This is illustrated in Fig. 5-2a, where a typical force curve is shown. The force is measured by means of the deflection of the cantilever, monitored by a laser beam reflected from the cantilever onto a photodiode, and serves as the feedback signal. As such, approach of the cantilever yields a loading curve until it reaches the force setpoint (bottom of the driving sine, dashed curve), after which the tip retracts. We define the force of adhesion as the minimum value of the unloading curve, as highlighted in the figure (dashed circle).
The position dependent adhesion force as a function of applied potential is shown in Fig. 5-2b, where the tip is not under potential control. In the figure every pixel corresponds to the adhesion obtained from a single force curve. We continuously scan the same 500 nm long line by disabling the slow scan axis of the AFM system. At the same time the substrate potential is stepped between $\sim$ 0.2 - 0.8 V vs. Ag/AgCl in steps of 0.05 V, where every potential is maintained for 60 s. This polarization routine is executed 2 times. The oscillation amplitude of the cantilever is 100 nm, with a force setpoint of 10 nN. The scan rate of the AFM is set to 0.1 Hz, and force curves are only recorded during the trace of the scan. As such, there is a 5 second gap in recording between consecutive lines in Fig. 5-2b, and every 6 lines constitute a single potential step. The topography is obtained simultaneously, where the profile for the final line of the scan is depicted in Fig. 5-2b, with the full scan shown in SI 5-5.

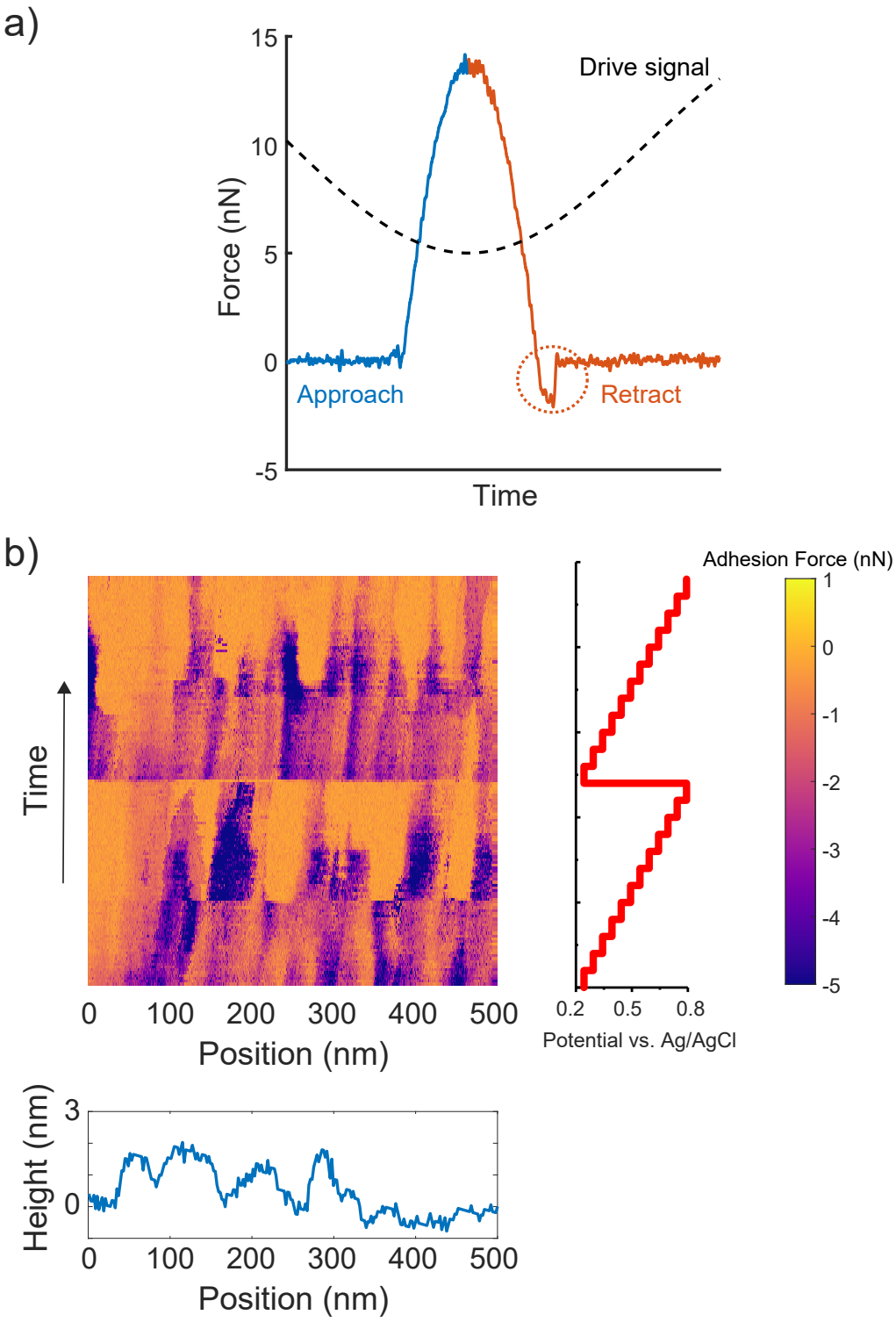

Figure 5-2: a) Illustration of a force curve in peakforce tapping, the cantilever is driven sinusoidally (black dashed curve), where the tip approaches the sample (blue) until the setpoint force is reached, after which the tip retracts from the surface (red). The adhesion is taken as the lowest point of the unloading curve, as illustrated by the dashed circle. **b)** Adhesion force map over a single 500 nm scan line as a function of time, while following the polarization routine as depicted on the right. The topography is shown at the bottom, as obtained from the final scan line.

Figure 5-2 shows a clear potential dependence in the adhesion force, which is reproduced over both cycles. A similar trend is present in the opposite direction of the potential sweep on a different area of the substrate (SI 5-6). We mainly observe higher adhesion at low potentials, which decreases when stepping the potential up. Importantly, the most pronounced change in adhesion occurs at ~ 0.5 V, which is the potential of the peak of the oxidation transient in the CV in Fig. 5-1b. We note however that the potential at which the adhesion abruptly changes is inhomogeneous over the surface.
To gain quantitative insight on the adhesion, we plot the histogram of adhesion at each potential for both cycles simultaneously as a violin plot in Fig. 5-3a, for both the forward and the backward potential scan [162]. The absolute value of the adhesion is depicted for clarity. While it is evident from Fig. 5-3 that the adhesion tends to high (low) values at low (high) potentials, a more intricate evolution with potential is now visible. In the positive scan direction (Fig. 5-3a, top) the distribution initially broadens asymmetrically to higher adhesion values, which we observe to be due to certain locations on the substrate in Fig. 5-2b. This fraction of the histogram with high adhesion is also reflected in the average value of the adhesion, as shown in Fig. 5-3b. The reverse scan shows a different potential dependent behavior in the region 0.6 - 0.4 V, resulting in a hysteresis loop in the average adhesion shown in Fig. 5-3b. Similarly to the forward scan however, the reverse sweep also displays an initial broadening of the distribution. While these measurements are done on different locations of the substrate, it should be noted that the final distributions and average values are very similar in both cases. We therefore consider it likely for the hysteresis to be caused by different electrochemical behavior for both scan directions, rather than a difference in the measurement locations.

We now compare these results with those reported in literature, where it should be noted that the shape for the average adhesion in Fig. 5-3b for the forward scan is qualitatively the same as that observed by Kasuya et al. [163] using K_2SO_4 on a gold electrode (1 mM, pH 7). Additionally, Serafin et al. [155] observe a similar increase in adhesion on a certain potential range for a gold surface in 10 mM NaOH. This increase occurs at the same potential as the specific adsorption of OH^- on the gold surface, as evidenced by cyclic voltammetry. Based on additional measurements in other electrochemical systems the force of adhesion is attributed to the reorganization energy of water and/or the anion at the surface. As such, a strong adhesion is expected for disordered surfaces. This explanation shows striking similarities with our experiments and the picture of the gold surface laid out at the start of this section, where progressive sulphate adsorption is expected in this system, culminating in an ordered overlayer at the highest potentials.
Considering again the results of Fig 5-2 and Fig. 5-3a with this interpretation in mind, the different parts of the adhesion distribution are then associated with certain regions that behave differently. Starting from the PZC and scanning the potential up, specific regions of high adhesion then contain weakly bound water or sulphates, which progressively become more ordered at higher potentials. On the other hand, some regions go directly into the final state of a more ordered layer, evidenced by a sudden switch to low adhesion at the PZC. Interestingly, while the general behavior is the same over both cycles, the response is not exactly the same for all sites for the consecutive potential sweeps. This therefore leads us to believe that the observed behavior is related to randomized adsorption, rather than effects related to the local topography.

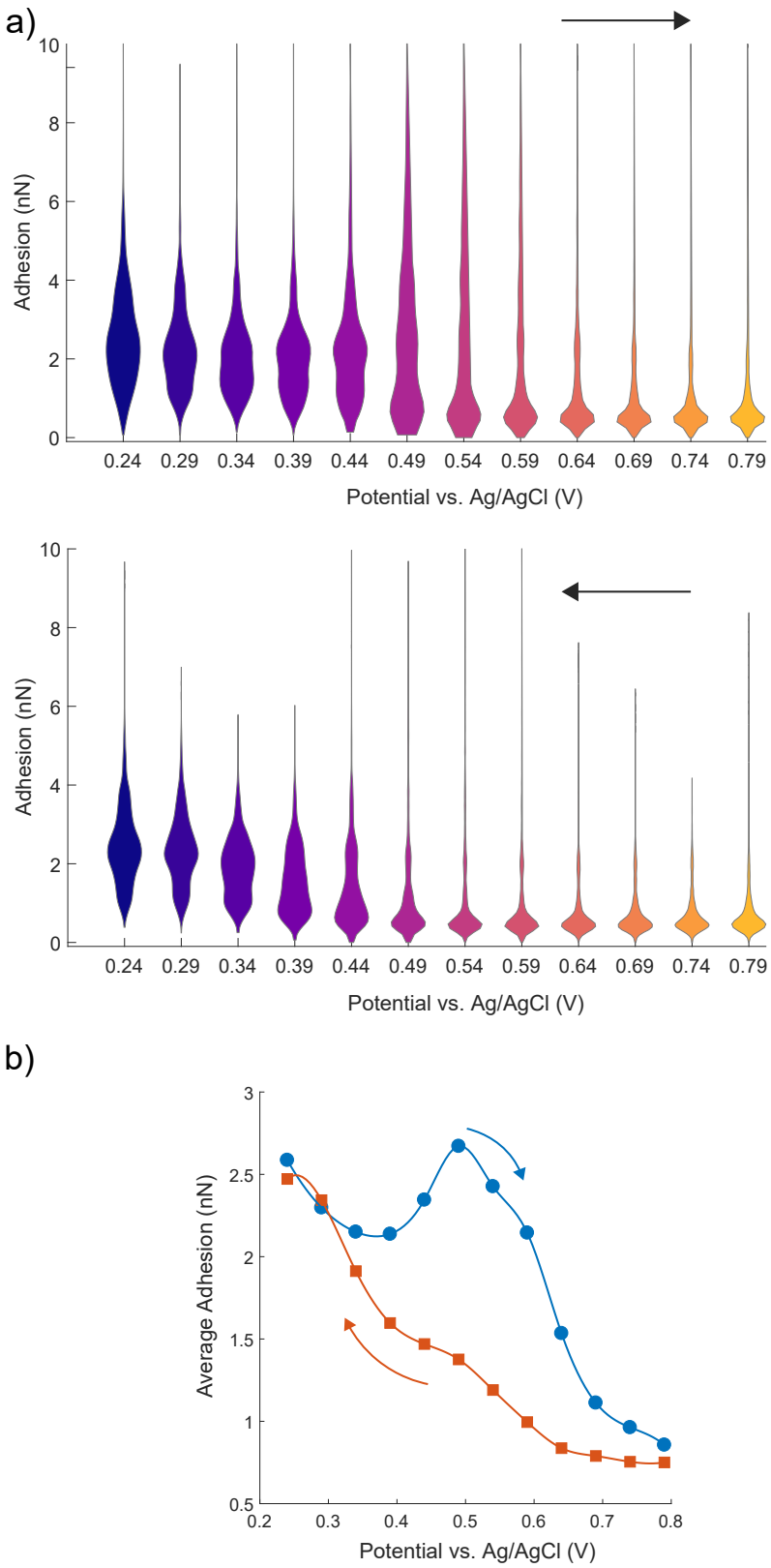

Figure 5-3: a) Violin plots of the adhesion force distribution as a function of substrate potential for the upward (top) and downward (bottom) potential scan, containing both potential cycles. **b)** Average value of the adhesion force as a function of substrate potential for both scan polarities and containing both cycles. The absolute value of the adhesion is shown for clarity for all images.

5-3 Conclusion

In summary, we present adhesion mapping of a potential-controlled gold surface in a Na_2SO_4 electrolyte. We observe a clear dependence of the adhesion value on the potential of the substrate, that is spatially inhomogeneous. Based on literature, this behavior is related to the degree of order of the surface, where the adhesion is a metric for the reorganization energy of the interface. More specifically in our system, this is linked to the adsorption of sulphates at the electrode, based on cyclic voltammetry. From our experiments we observe that this disorder appears at specific locations of the substrate for a certain polarization of the electrode, but appears to be more randomized over different potential cycles. As a final remark, we highlight the possibility of additional potential control of the tip electrode in our experimental setup. Considering the different effects that influence the adhesion force, this provides an additional degree of freedom, where the potential, or chemical makeup of the tip can be changed *in-situ* to modulate the sensitivity of the measurement to electrical, chemical, or solvation forces.

5-4 Methods

Materials
The substrate consists of a Au film ($\sim$ 50 nm thick) with a $\sim$ 5 nm Ti adhesion layer deposited by electron beam evaporation on top of a p-type Silicon sample (Siegert Wafer) as a flat support. The solutions were prepared using Na_2SO_4 (ACS reagent, $\geq$ 99.0%, from Sigma-Aldrich) in MilliQ® (18.2 M$\Omega\cdot$ cm) water.

Electrochemical cell
The electrochemical cell was homemade and consisted of Teflon™, made leak tight by an O-ring. Top-contacts were made by a spring-loaded pin outside of the O-ring. Potential/current control and readout were done with a CH760E potentiostat. Measurement were done in a 3-electrode configuration. The counter electrode (CE) consisted of a circular platinum wire around the edge of the cell. The reference electrode was a leakless miniature Ag/AgCl electrode (EDAQ, ET072-1), inserted on the side of the cell. As such the distance between the CE was closer to the sample than the reference, which we consider not to influence potential control as the experiments are carried out in the EDL charging regime and therefore no IR drop is expected.

Atomic force microscope
The measurements were performed using a Bruker Dimension Icon AFM, controlled through the Nanoscope software. The nanoelectrode AFM probes were obtained from Bruker (PeakForce SECM) and were electrically insulated except for the platinum coated apex, which has a diameter of $\sim$ 50 nm [110]. The AFM spring constant was obtained for each cantilever by doing a thermal tune at a distance of $\sim$ 1 mm from the substrate in air after obtaining the deflection sensitivity on the gold substrate. The resonance frequency of the tip was 52.5 kHz, with a quality factor of 139, which we report here as proposed in reference [115]. From this, a spring constant of 0.77 $\frac{N}{m}$ was obtained.

Reference electrode calibration

The open circuit potential (OCP) of the miniature reference electrode is measured against a larger saturated Ag/AgCl reference electrode (Radiometer analystical B20B300, XR300. Batch: 182B4-A10) in a 1 M Na_2SO_4 solution before the measurement as a means of calibration (where the OCP of the miniature reference was +193 mV for the measurements in this chapter). The large reference electrode is used only for calibration purposes.

Data treatment

HSDC data is read out in MATLAB®, using the NanoScopeMatlabUtilities (NSMU) toolbox. Individual force curves are identified by means of detecting dummy datapoints that are inserted by the NSMU toolbox and separate tapping cycles. The adhesion force is then obtained for every force curve as the lowest value of the unloading curve, defined by a synchronization parameter obtained from the AFM datafile.

5-5 Supplementary information

SI-1 XRD of a gold substrate.

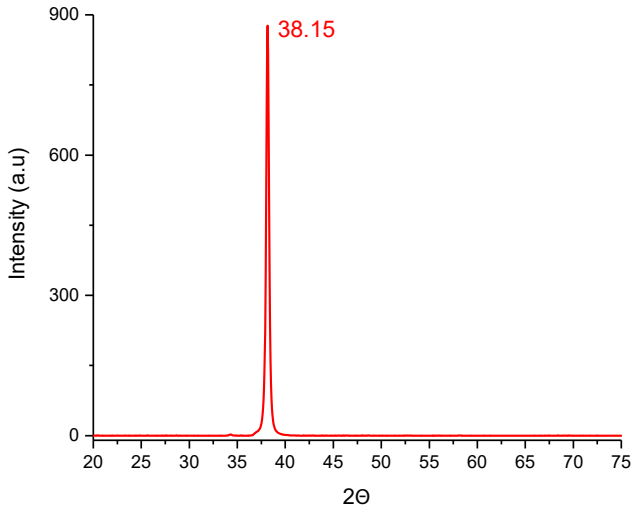

Figure 5-4: X-ray diffraction measurement of a representative sample consisting of 50 nm Au + 5 nm Ti on silicon. A pronounced peak associated with the Au(111) orientation is observed at a 2Θ angle of $\sim 38.1°$.

SI-2 Topography during the potential scan (increasing).

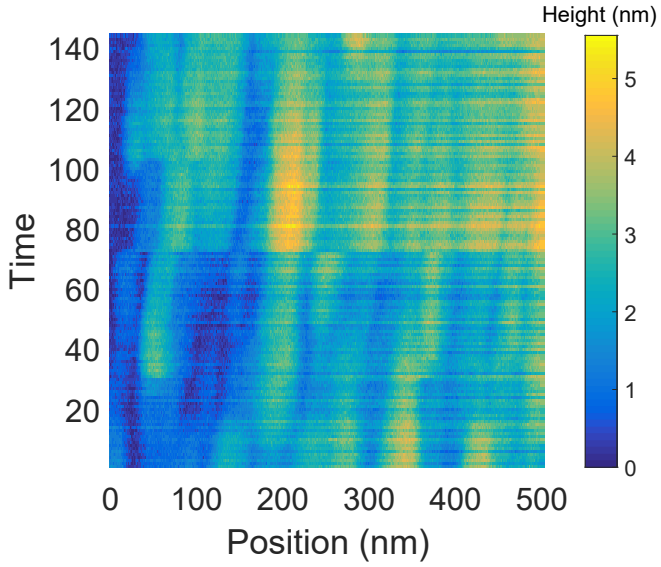

Figure 5-5: Topography obtained during the measurement as shown in Fig. 5-2. The image is modified by a line-by-line linear correction for sample tilt.

SI-2 Adhesion map during the reverse potential sweep

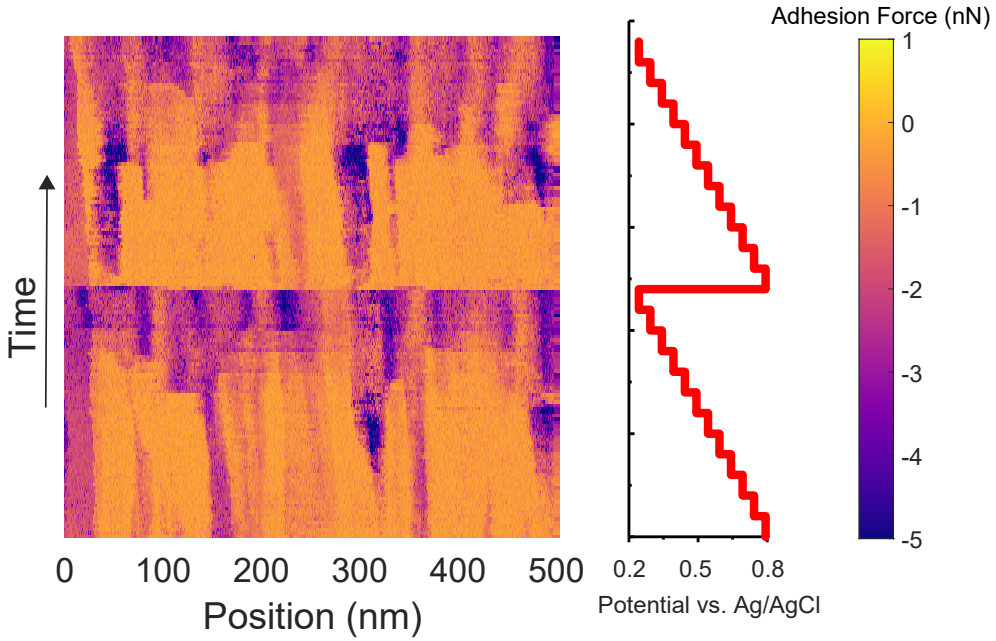

Figure 5-6: Adhesion as a function of potential over a 500 nm wide scan line with the opposite polarization routine as in Fig. 5-2, obtained at a different location on the substrate.

Chapter 6

Nanofluidics in microscopic systems

In this final chapter we turn from scanning probe systems, and rather use electrical transport measurements to investigate ionic current along the electrical double layer. We present an experimental platform designed to observe the phenomenon of ion current rectification (ICR) at large scales, by considering asymmetric microscopic channels. The ICR emerges due to an interplay between bulk and surface transport, and the results presented in this chapter are to the best of our knowledge the first to show this behavior in microscopic channels without the use of chemical modification.

6-1 Introduction

Ionic transport in small channels has unique properties compared to that in the bulk, as the response of the system is influenced by the interface. This allows for interesting phenomena such as selective transport or ion pumps [164, 165], streaming currents [166], and electrical circuit analogues [167,168]. Most of these are understood by considering the electrical double layer (EDL), that forms near the surface in a region bounded by the Debye screening length, λ_D. Within the EDL the solution is not charge neutral, as counterions balance the charge density of the channel wall. Relevant to the measurements presented in this chapter, ionic transport through the EDL differs from the bulk in 2 main ways; i) Surface charge typically present on the channel walls attracts counter,- and repels co-ions, making transport through the EDL selective for a certain polarity of charge carriers [164], ii) as the total charge in the EDL is (at least directly) independent of the bulk concentration, but rather balances the surface charge density of the channel wall, the conductivity is concentration-independent [169, 170].

A unique case is that of ion current rectification (ICR), where the current response of the system displays non-linear current-voltage behavior with a high-, and low conductance state. [171, 172]. Understanding such ionic nonlinear response is of broad interest, extending to applications such as desalination or energy generation [173, 174].

ICR has been observed in asymmetric nanochannels, where the asymmetry can be introduced in different ways, such as geometry, charge, or concentration [175–177]. The process is schematically illustrated in Fig. 6-1 for a geometrically asymmetric channel.

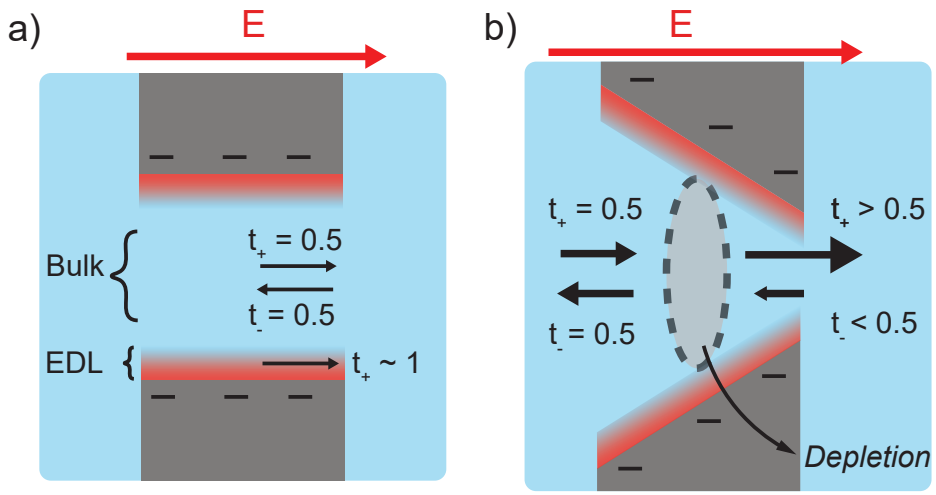

Figure 6-1: a) Schematic representation of a symmetric channel with a negative surface charge, where the channel radius is larger than the EDL. With an electric field applied as indicated, the middle of the channel behaves as the bulk, where $t_+ = t_- = 0.5$ for ions with equal mobility. In the EDL there are mainly counterions present, resulting in selective transport with $t_+ \sim 1$. The transference numbers vary along the cross section of the channel, but are constant along the channel length. **b)** Representation of a tapered channel. As the relative contribution of the EDL to the total transport varies along the channel length, the transference numbers differ at the large base, which is bulk-like with $t_+ = t_- = 0.5$, and the smaller tip, which is more surface-like with $t_+ > 0.5 > t_-$. This asymmetrical transport results in ion depletion (accumulation) for positive (negative) applied potentials and suppressed(enhanced) conductance.

Firstly, Fig. 6-1a shows a symmetric channel carrying a negative surface charge, and with a diameter larger than $2{\cdot}\lambda_D$, as represented by the red shaded area. For simplicity we consider a 1:1 electrolyte with ions of equal mobility. Upon applying of an electric field we then distinguish ion transport through the center of the channel and that near the interface along the EDL. Ion transport through the center behaves as that in the bulk, where anions and cations are transported equally. This results in equal transference numbers for both polarities, $t_+ = t_- = 0.5$, where the transference number is a metric for the partial current due to any of the ion species. In contrast, current is carried mostly by cations at the interface, given the increased density due to screening of the surface charge, resulting in $t_+ \sim 1$ and $t_- \sim 0$. Depending on the size of the channel with respect to λ_D, the total current is therefore either carried equally by both species, or mainly by cations in the symmetric channel.
Fig. 6-1b shows the case for an asymmetric pore. We assume that the opening at the wide base (left) is such that the conductivity is dominated by the bulk response, while the influence of the surface is more pronounced at the small tip (right). In this case, the electric field along the channel yields total a total transfer coefficient that gradually changes along the channel, where $t_+ = t_- = 0.5$ at the base and $t_+ > 0.5 > t_-$ at the tip, as a larger part of the current flows through the charge-selective EDL. As such, cations (anions) leave the tip (base) more easily than they are replenished from the base (tip), as indicated by the arrows in Fig. 6-1b.

Realizing that the total current has to be equal on both sides of the membrane, this results in a depletion of ions inside the channel, suppressing the conductance. The opposite is true for an electric field directed from the tip to the base, which leads to accumulation of charge carriers and enhanced conductance. This therefore results in an asymmetric electrical response of the channel, with a low (high) conductance at positive (negative) potentials applied from base to tip. Furthermore, this implies that the total current is (to a degree) selective, determined by the transference at the tip. This effect of different conductance at opposite polarities is known as ion current rectification.
As the depletion(accumulation) is governed by the varying relative contribution of the EDL to the total transport along the channel length, this has often been thought to require the width of the tip to be smaller than the EDL thickness ($R_{tip} \leq \lambda_D$). However, ICR has also been observed in systems much larger than λ_D recently through chemical modification of the channel walls to increase the surface charge [178–180]. In fact, the argument above does not prescribe double layer overlap at the tip, but merely requires that ionic transport in the tip is influenced by the EDL rather than the bulk, as to achieve a difference in transference between the base and the tip.

The length at which the surface conductance is comparable to that of the bulk is given by the so-called Dukhin length l_{Du}. With the total charge in the EDL being determined by the surface charge, l_{Du} relates the surface charge density to the bulk concentration, and can be much larger than the screening length (up to several microns). Normalizing l_{Du} to the channel radius gives the dimensionless Dukhin number given by; [181]

$$l_{Du} = \frac{|\sigma|}{ec_{bulk}}, Du = \frac{l_{Du}}{R} \tag{6-1}$$

As such, Du > 1 indicates that surface conductance is dominant for a certain channel width. Recent theoretical work has therefore explored the importance of the Dukhin number, rather than the screening length, for ion transport in asymmetric channels, and predicts that this is the key length scale for the occurence of ICR [182, 183]. The measurements conducted in this chapter explicitly aim to verify these predictions experimentally; considering asymmetric silicon microscopic channels without any chemical modification of the surface.

6-2 Conductance measurements in an asymmetric microchannel

Tapered microscopic channels are fabricated in a 2 μm thick silicon membrane by milling a hole with a focused ion beam (FIB). The taper is created by writing concentric circles with decreasing radius, with a base radius of $R_{base} \sim 5\mu m$ and a tip radius of $R_{tip} \sim 1\mu m$. Fig. 6-2 shows two membranes with similar geometry and size, which will be referred to as M1 and M2 hereafter. When immersed in a homogeneous electrolyte, the size ratio of ~ 5 between the tip and base results in the same increase in Dukhin number, where $\mathrm{Du}_{tip} = 5\ \mathrm{Du}_{base}$ following equation 6-1. As the membranes are exposed to air prior to the transport measurements, we expect the Si surface to be covered by a native SiO_2 layer.
Measurements are carried out as depicted in Fig. 6-2c. The membrane is placed between two reservoirs of equal concentration of KCl and a potential difference is applied across the reservoirs using Ag/AgCl wire electrodes. The polarity of the potential is of note for the

expected behavior, which is applied here to the reservoir facing the large opening. KCl is chosen because the mobilities of the K^+ and Cl^- ions are similar. Furthermore, the Ag/AgCl electrodes provide a facile reaction at the electrode to minimize the potential drop at the electrode interfaces, so that the applied potential falls over the channel.
We measure the conductivity of the channel by means of I-V curves at different concentrations, where the KCl concentration is varied by dilution of the baths. We note that unequal concentration of the reservoirs is expected to yield an offset of the open circuit potential (OCP) of magnitude $\sim 60mV * log_{10}(\frac{c1}{c2})$ according to the Nernst equation [164], as was illustrated in section 1-1.

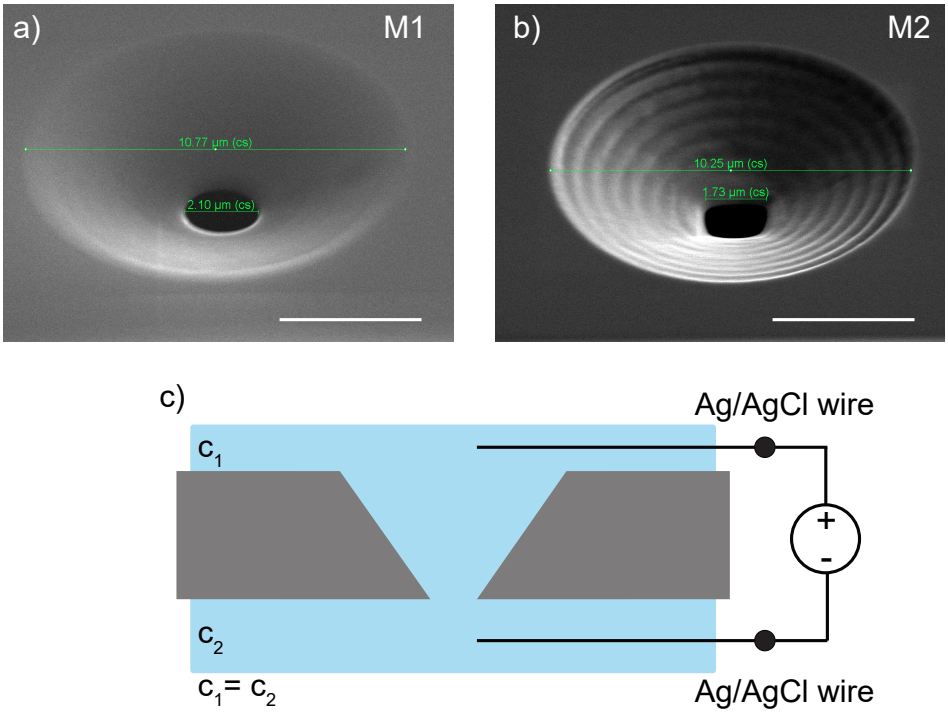

Figure 6-2: **a,b)** SEM images of tapered microchannels in a 2 μm thick crystalline silicon membrane. The dimensions of the base and the tip are indicated in the image as measured in the SEM, with $R_{base} \sim 5\ \mu m$, and $R_{tip} \sim 1\ \mu m$. The scale bar is 4 μm, the images are obtained with a tilt of 52°. **c)** Schematic representation of the experimental setup. Conductance measurements are done with 2 Ag/AgCl wires across the membrane, separating 2 reservoirs of equal concentration. The applied potential polarity is the side with the large opening with respect to the small opening.

The resulting I-V curves for M1 and M2 are shown in Fig. 6-3a and b, respectively, where the potential is swept from positive to negative voltages, for different concentrations of the electrolyte baths. The current is normalized to the value I(-0.75 V) to highlight the shape of the response. The limited concentration range for M2 is due to breaking of the membrane during the dilution step, as the membranes are rather fragile.

At the highest concentrations both channels show ohmic behavior with a linear I-V response, consistent with bulk dominated transport. By decreasing the ion concentration, conductance through the channel starts to show rectification. In agreement with the discussion in section 6-1, the channel displays low(high) conductance at positive(negative) applied potentials as

depletion (accumulation) of ions occurs in the channel.
Additionally, we calculate the differential conductance of the channels at 0 V as a function of ion concentration, shown in Fig. 6-3c. The dashed lines indicate the expected conductivity for a straight-walled 2 μm long channel of either 1 μm, or 5 μm radius (black dashed lines), as given by [170],

$$G = \frac{\pi r^2}{L}((\mu_+ + \mu_-)ne + \mu_+ \frac{2\sigma}{r}) \tag{6-2}$$

with r the radius, L the length of the channel, σ the surface charge of the wall, n the number density of ions in the solution, e the elementary charge, and μ the ion mobilities. We consider the same mobility for both ions, by using a diffusion coefficient of $1.9 \cdot 10^{-9} \frac{m^2}{s}$ [184, 185]. It should be noted that equation 6-2 contains a linear term with ion concentration for the bulk response, and a concentration independent term for conduction through the EDL.

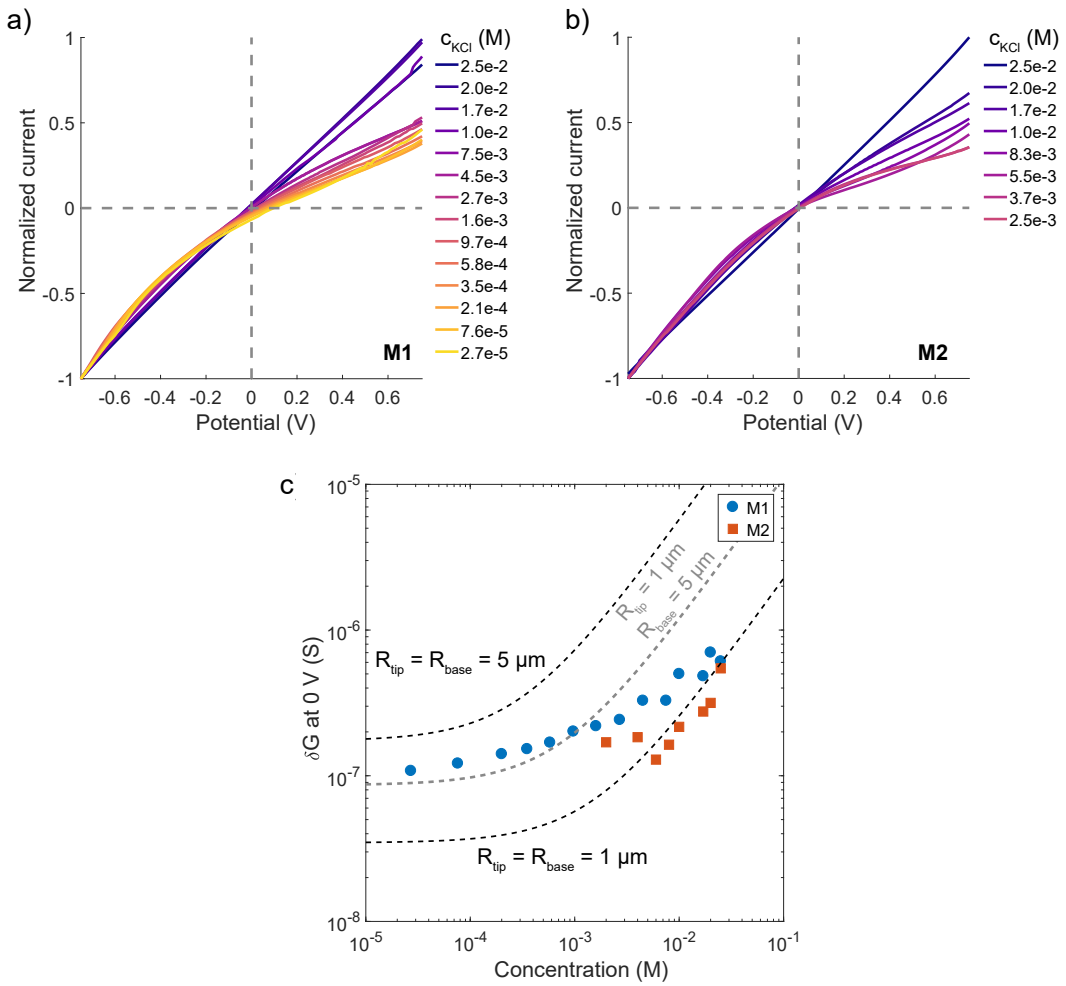

Figure 6-3: a,b) Normalized I-V curves obtained for the micropore membranes from Fig. 6-2 at different concentrations. **c)** Differential conductance at 0 V for both membranes. The dashed lines are obtained from equation 6-2 for straight channels with radius 1 μm, and 5 μm (black), and for a tapered channel (grey) with those dimensions for the two openings (SI-1). The surface charge is taken to be 150 $\frac{mC}{m^2}$, based on the data for M1.

In the case of an asymmetric channel, we derive the expected conductance from equation 6-2 (SI-1), as shown by the grey dashed line for a tapered channel with the same dimensions for the large and small opening, respectively. Based on the data from M1, we therefore use a surface charge of 150 $\frac{mC}{m^2}$ for all three calculations, which is in the same order as values reported in literature [186, 187]. We note that the there is a slight difference in the conductivity of both membranes, despite their dimensions being nominally the same, which can be due to different membrane thicknesses as specified by the supplier ($2 \pm 0.5\ \mu$m). Following equation 6-2 the figure shows a linear decrease of the conductivity at high concentrations, with a plateau at low concentrations most clearly observed for M1. The latter is therefore an important feature as it is associated with the surface dominated transport, which we observe here at concentrations below $\sim 10^{-3}$ M, where the Debye length is much smaller than the tip radius ($\sim$ 10 nm vs. $\sim 1\ \mu$m).

6-3 Ion current rectification

We now focus on the rectifying behavior emerging at low concentrations in the asymmetric channels. To better asses the magnitude of ion current rectification we plot the concentration dependent ICR in Fig. 6-4, given by the ratio $\frac{|I(-0.75V)|}{|I(0.75V)|}$. It should be noted that the absolute ICR value is determined by the potential at which it is calculated, as a consequence of the asymmetric response. Fig. 6-4 also shows the concentration dependent ICR as expected from the model described in reference [183] (grey dashed line), defined as the difference in selectivity between the tip and the base. The predicted ICR value is qualitative and is scaled for clarity in the figure. For the model, we assume the radius of 1 μm, and 5 μm for the tip and the base as obtained from the SEM images, respectively, and a surface charge density of 150 $\frac{mC}{m^2}$, estimated from Fig. 6-3c.

It is clear from Fig. 6-4 that ICR appears as the concentration is decreased, starting from an Ohmic response (ICR = 1). Notably, the screening length is much smaller than R_{tip} at the concentrations where the response starts to deviate from the linear relation (λ_D is $\sim$ 3 nm at 10^{-2} M). Similar to the model prediction, we observe that the ICR peaks, and then decreases by lowering the concentration further in the case of M1 (blue circles). Here, it is important to note that this apparent symmetry in the ICR has a different origin at both ends. At low concentrations the base is also expected to get progressively more selective, ultimately resulting in a transference of 1, similar to the tip. In this case, while the full channel is selective for a certain ionic charge, the asymmetry is lifted, and no rectification occurs. For the 5 μm base radius, the Dukhin number is $\sim$ 30 for a concentration of 10^{-5} M, using $\sigma = 150\ \frac{mC}{m^2}$. At high concentrations on the other hand, the asymmetry persists but decreases in magnitude with the surface becoming progressively less dominant as the Dukhin number decreases (Eq. 6-1). For the 1 μm tip radius, the Dukhin number is $\sim$ 0.15 for a concentration of 10^{-2} M, using $\sigma = 150\ \frac{mC}{m^2}$. As such, the transference number at the tip gets closer to that of the bulk, making the channel more symmetric. In fact, ICR is still expected to occur at higher concentrations, if the potential difference is increased sufficiently so that even small differences between the transference at the tip and the base cause ion accumulation/depletion [182]. In our experiments an exponential increase in the current for both polarities is observed at applied potentials larger than $\sim$ 1 V, which we attribute to the electrochemical response of the electrodes, rather than that of the channel.

As such, the data matches the trend in the model curve, and is rather close for the position

of the peak in the case of M2. For M1, the region of ICR is noticeable wider than the predicted shape. A possible explanation is that we assume a constant surface charge for the model curve, as the main contribution to negative surface charge is thought to be the pH-dependent dissociation of silanol groups and the experiments are conducted at constant pH [188]. The surface charge has been predicted to be dependent on the KCl concentration however, as a lower bulk concentration results in additional H^+ ions in the EDL, effectively lowering the pH near the interface [166,188]. A concentration dependent surface charge would result in stretching of the ICR curve on the low concentration side, as observed for M1. A different consideration is that our experimental system varies from the model calculation as it assumes a slowly varying geometry, with the width halfway through the channel (w_{half}) being much smaller than the total length (L), which is required as to decouple the transversal and longitudinal ion relaxation in the channel [183]. This condition is not met in our channel, where $w_{half} \sim L$.

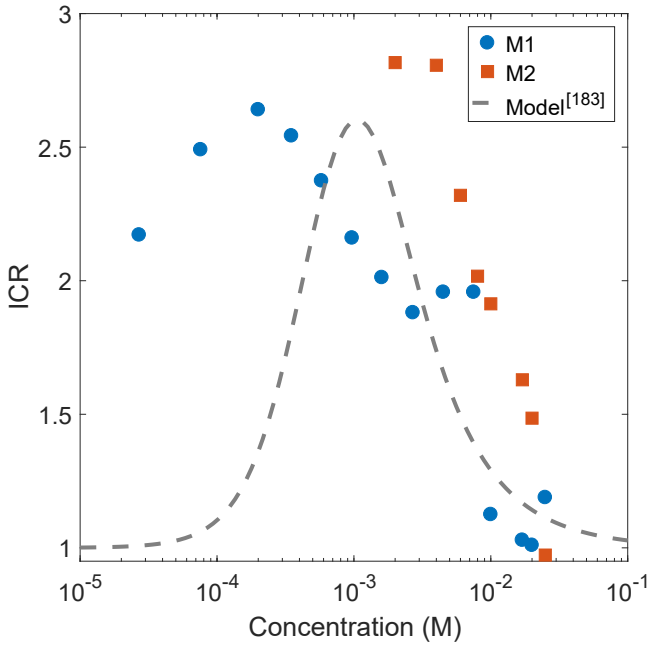

Figure 6-4: ICR obtained at (-)0.75 V from the data in Fig. 6-3 for both membranes. The grey dashed curve is obtained from the model in reference [183] using the dimensions obtained from Fig. 6-2 and a surface charge of $\sigma = 150\ \frac{mC}{m^2}$.

6-4 Conclusion

To conclude, we observe ICR in pores with a radius $R_{tip} > 1\mu m$, validating a recent theoretical description of channel conductance, which is ruled by l_{Du} rather than λ_D. To the best of our knowledge this is the first demonstration of rectification in micron-sized pores without chemical modification of the channels walls [178–180]. Considering the potential of ICR for applications in desalination and osmotic energy generation [173], the use of silicon membranes provides an attractive platform for further functionalization, since the devices are compatible

with standard CMOS fabrication techniques. As the larger base opening allows for higher current throughput, and the larger tip opening makes the system more resistant to clogging/ fouling, this is therefore a first step towards high throughput ion-selective membranes and blue energy harvesting.

6-5 Methods

Current measurements
Conductance measurements were done with a Biologic SP-300 potentiostat using cyclic voltammetry, in a 2 electrode setup with 2 Ag/AgCl wire electrodes. The scan rate was 10 $\frac{mV}{s}$ for concentrations $\geq 9.7{\cdot}10^{-4}$ M, and 15 $\frac{mV}{s}$ at lower concentrations. The membrane was glued to a tube with a silicone sealant to form the first reservoir, and then submerged in a larger bath. The concentration was varied by dilution of the baths.

Electrode preparation
Ag/AgCl electrodes were fabricated following an adapted procedure from reference [189]. A silver wire (99.9%) was immersed in 0.1 M HNO_3 to remove oxide from the surface and then rinsed with Milli-Q® water. The cleaned wire was used as a working electrode in a 3-electrode setup with a platinum counter,- and quasi reference electrode in an aqueous solution of 3 M KCl. The Ag wire was coated with AgCl by applying 2 V vs. the Pt wire reference for 10 minutes.

Micropore fabrication using focused ion beam
Asymmetric pores were fabricated in 2 μm thick crystalline silicon membranes (Norcada, SM10480N) using a focused ion beam (FEI Helios Nanolab 600, Ga ions), by milling concentric circles with decreasing radius. The beam current was 0.46 nA with an acceleration voltage of 30 kV. SEM images of the final device were made after milling in the same system.

6-6 Supplementary information

SI-1 Derivation of the conductance in a tapered nanochannel

Starting from equation 6-2 for a straight segment of the channel and using;

$$r = (\frac{(r_{base} - r_{tip}}{L})x + r_{tip}\ from\ 0\ to\ L \rightarrow$$
$$dr = (\frac{(r_{base} - r_{tip}}{L})dx\ from\ r_{tip}\ to\ r_{base}$$

$$dR_{bulk} = \frac{dx}{\pi r^2 ne(\mu_+ + \mu_-)}$$
$$R_{bulk} = \frac{L}{\pi ne 2\mu_+(r_{base} - r_{tip})} \int_{r_{tip}}^{r_{base}} \frac{1}{r^2}\, dr$$
$$R_{bulk} = \frac{L}{\pi ne 2\mu_+(r_{base} - r_{tip})} \cdot (\frac{1}{r_{tip}} - \frac{1}{r_{base}}) \tag{6-3}$$

$$dR_{surf} = \frac{1}{\sigma\mu_+ 2\pi r} dx$$
$$R_{surf} = \frac{L}{\sigma\mu_+ 2\pi(r_{base} - r_{tip})} \int_{r_{tip}}^{r_{base}} \frac{1}{r}\, dr$$

$$R_{surf} = \frac{L}{\sigma\mu_+ 2\pi(r_{base} - r_{tip})} \cdot ln\frac{r_{base}}{r_{tip}} \tag{6-4}$$
$$G_{taper} = \frac{1}{R_{bulk}} + \frac{1}{R_{surf}} \tag{6-5}$$

Equations 6-3 through 6-5 are used for the conductance of the tapered channel in Fig. 6-3.

Summary

This thesis aims to measure and control behavior of ions in solution near a charged, or electrified, surface. Such electrochemical systems are found everywhere, ranging from biological to industrial processes, and can be greatly affected by small changes at the boundary between the solid and the liquid. A better understanding of the dynamic processes occurring at the electrified interface is therefore of great interest for many applications. In particular, our main focus lies on forcing ions to deposit locally with nanoscale precision under influence of an applied potential, ultimately providing a path to the free-form writing of 3-dimensional functional materials. The bulk of the presented experiments make use of a sharp probe to both initiate the local deposition of metals and inspect the resulting structures, providing information on the underlying process. In the final chapters we expand the range of electrochemical phenomena under investigation from deposition reactions; to the potential-controlled state of the surface; and finally to the behavior of devices tailored to harness excess charge in the solution, near the interface.

As such, we briefly outline the conditions under which electrodeposition occurs in Chapter 1, as a means to frame the history of electrochemical scanning probe lithography. Additionally, this serves as the basis for our initial hypothesis of localizing electrochemical reactions in highly dilute electrolytes using a simplified electric circuit model. As such, Chapter 2 describes the experiments conducted in micromolar concentrations of $CuSO_4$, where we demonstrate the direct writing of copper nanostructures with feature sizes below 100 nm. This is done by applying a potential difference between an atomic force microscope tip and the substrate, while the tip is continuously 'tapping' the surface. From our experiments a rather dynamic picture of the deposition mechanism emerges, where we believe the tip to continuously disrupt the screening layer at the substrate-liquid interface. Without the screening layer, this results in a direct electrostatic interaction between the tip and copper ions in the tip-substrate gap, enabling local electrodeposition. As we only observe the deposition at very low concentrations, this leads us to propose a confinement mechanism that balances the access of ions with shaping of the electrochemical potential in the tip-substrate gap.

Chapter 3 investigates the growth dynamics of the nanostructures deposited by the direct writing mechanism. As there is very little material in the copper deposits, we study the shape evolution of these nanostructures using atomic force microscopy images, and compare

these with non-directed copper growth in a regular (macroscopic) electrochemical cell at millimolar and micromolar concentrations. We observe that individual nuclei have a spheroidal rather than a faceted shape, observed for deposition at higher concentrations. From our results it appears that the directed growth occurs in two main steps, where isotropic in-plane growth is followed by increased out-of-plane growth, as the process is confined to the dimensions of the tip. Compared with the non-directed copper growth, this isotropic growth step resembles that of metallic copper grown at higher concentrations, while the rest of the growth dynamics are similar to samples grown in the dilute electrolyte. As the latter is confirmed to consist mainly of CuO by X-ray photoelectron spectroscopy, we infer that this is a likely composition for the structures obtained in directed growth.

In Chapter 4 we investigate a different scheme for nanoscale electrodeposition, by applying short voltage pulses to the tip of an electrochemical scanning tunneling microscope. The short pulse results in an enhanced electrochemical rate close to the tip, due to a distance dependent charging of the interface. Rather than considering an equivalent RC-model of the system, we frame the mechanism in terms of the charging dynamics in a simple electrochemical system allowing us to express the achievable resolution in terms of fundamental properties of the electrolyte. We compare these predictions with values reported in literature and find good ($\leq$ factor 2) quantitative agreement. Using this framework, we demonstrate the deposition of cobalt nanostructures with feature sizes below 100 nm using dimethyl sulfoxide as a solvent. We show that the distance over which the interface charges is significantly improved over aqueous solutions for a given pulse length. This is attributed to the fast diffusion of protons, and is an important consideration in the experimental design of further research.

In Chapter 5 we look further into the mechanical interaction between the tip of an atomic force microscope and a gold surface under potential control, in a sulphate containing solution. Specifically we map the force of adhesion while changing the potential of the surface and find that the adhesion has both a clear potential,- and spatial dependence. The adhesion is linked to the potential-dependent adsorption of sulphates on the surface, which affects the adhesive force by means of the required energy for reorganization of the surface. We find this adsorption to occur on certain locations on the substrate with the associated increased adhesion persisting over time, but contrastingly these locations of higher adhesion appear to be more randomized over consecutive potential cycles.

In the final Chapter 6 we abandon scanning probe systems and turn to investigate ionic transport in asymmetric microscopic channels. The asymmetry results in the occurrence of ion current rectification, which is typically demonstrated in systems that are similar in size to the screening length. However, the rectification emerges as a larger portion of the current is carried through the electrical double layer at the small,- with respect to the large opening. It is therefore predicted that this phenomenon persists at much larger scales, as long as the electrical double layer contributes significantly to the total current at the small end. In this chapter we observe ion current rectification in microscopic conical channels, fabricated in crystalline silicon membranes by focused ion beam. This validates recent theoretical work, and is the first demonstration of ion current rectification at these scales without chemical modification of the channel walls. The rectification phenomenon is of particular interest to us for its potential in desalination and energy harvesting processes. Integrating large rectifying channels in this CMOS compatible silicon platform is therefore a first step towards membranes and fluidic devices that are more resistant to clogging and with high throughput.

Samenvatting

Dit proefschrift beoogt het gedrag van ionen in een oplossing te observeren en te controleren in de buurt van een geladen, of geëlektrificeerd, oppervlak. Zulke electrochemische systemen zijn overal aanwezig, van biologische tot industriële processen, en kunnen aanzienlijk worden beïnvloed door kleine veranderingen op het grensvlak van de vloeistof en de vaste stof. Een beter begrip van de dynamische processen die plaatsvinden nabij het geëlektrificeerde oppervlak is daarom van groot belang voor allerlei toepassingen. De aandacht van dit proefschrift gaat in het bijzonder uit naar het lokaal deponeren van metaal ionen onder invloed van een aangelegde potentiaal, met precisie op de nanoschaal. Dit heeft als einddoel om in vrije vorm driedimensinoale functionele materialen te 'schrijven'. Het grootste deel van de gepresenteerde experimenten maakt gebruik van een scherpe naald om zowel de lokale depositie te initiëren als de resulterende structuren te onderzoeken, waarmee informatie over het onderliggende proces wordt vergaard. In de laatste hoofdstukken wordt het scala aan onderzochte elektrochemische processen uitgebreid naar oppervlakteprocessen en de staat van het oppervlak onder invloed van de potentiaal; en naar het gedrag van microscopische apparaten, erop toegesneden om gebruik te maken van het overschot aan lading in de vloeistof, nabij het oppervlak.
Met deze doelen wordt in Hoofdstuk 1 een korte beschrijving gegeven van de condities die nodig zijn voor elektrochemische depositie, als kader voor een historisch overzicht van *scanning probe* lithografie. Daarnaast leidt dit tot onze initiële hypothese om elektrochemische reacties te lokaliseren in sterk verdunde oplossingen, gebaseerd op een gesimplificeerd elektrisch circuit. Als zodanig beschrijft Hoofdstuk 2 de uitgevoerde experimenten in oplossing met micromolaire concentraties $CuSO_4$, waar we het directe schrijven van koper nanostructuren demonstreren, met karakteristieke dimensies kleiner dan 100 nm. Dit wordt gedaan door middel van een potentiaalverschil tussen de punt van de naald, de tip, van een atoomkracht-microscoop en het substraat, terwijl de tip continu op het oppervlak 'tikt'. Uit deze experimenten komt een dynamisch beeld van het depositieproces naar voren, waar de punt continu de lading-afschermende laag nabij het vaste stof/vloeistof grensvlak verstoort. Zonder deze afscherming is een directe elektrostatische interactie mogelijk tussen de tip en koper ionen in de tip-substraat opening. Aangezien we de depositie alleen observeren bij deze hele lage concentraties stellen wij een lokalisatiemechanisme voor waarbij er een balans is tussen toegang van ionen en het afschermen van het elektrische veld in de opening.

In Hoofdstuk 3 bestuderen we het mechanisme van de geleide groei uit het vorige hoofdstuk. Omdat er in de gedeponeerde nanostructuren voor veel karakterisatie technieken te weinig materiaal beschikbaar is kijken we naar de tijdsevolutie van de vorm van de structuren met behulp van atoomkrachtmicroscopie. We vergelijken deze met de ongeleide groei van koper in een conventionele (macroscopische) elektrochemische cel uit vloeistoffen met micromolaire en millimolaire concentraties. We observeren dat individuele nuclei een sferische vorm hebben in plaats van een gefacetteerde, zoals in de hogere concentratie. Vanuit deze resultaten lijkt de geleide groei uit twee stappen te bestaan, waar isotrope groei in het vlak (horizontaal) wordt opgevolgd door toenemende groei uit het vlak (verticaal), en waar de isotrope groei wordt begrensd door de dimensies van de tip. Vergeleken met de ongeleide groei van koper lijkt deze isotrope groeistap op die van metallisch koper bij hogere concentraties, terwijl de rest van het groeimechanisme soortgelijk is aan de groei in verdunde oplossingen. Voor deze groei uit verdunde oplossingen bevestigen we dat het voornamelijk bestaat uit CuO door middel van röntgen foto-elektronenspectroscopie, waaruit we afleiden dat dit een waarschijnlijke compositie is voor de structuren verkregen met de geleide groei.
In het vierde Hoofdstuk (4) onderzoeken we een ander concept voor elektrodepositie op de nanoschaal, waar we korte spanningspulsen aanbrengen op de tip van een elektrochemische scanning tunneling microscoop. De korte pulsen resulteren in het versnellen van de elektrochemische reactie in de buurt van de tip, doordat het opladen van het vaste stof/vloeistof grensvlak afstand afhankelijk is. In plaats van dit systeem te behandelen als een equivalent RC-model, bekijken we dit mechanisme vanuit de ladingskarakteristiek van een simpel elektrochemisch systeem. Hierdoor kunnen we de haalbare resolutie uitdrukken in fundamentele eigenschappen van het elektrolyt. We vergelijken deze voorspelde resolutie met waarden uit de literatuur voor het etsen van metalen, waaruit blijkt dat deze kwantitatief overeenkomen ($\leq$ factor 2). Gebruikmakend van dit kader demonstreren we de deposite van kobalt nanostructuren met karakteristieke dimensies kleiner dan 100 nm, waar we dimethylsulfoxide als oplosmiddel gebruiken. We tonen aan dat de afstand tot waar het vaste stof/vloeistof grensvlak voldoende oplaadt voor depositie significant verbetert ten opzichte van het gebruik van water als oplosmiddel. Dit schrijven wij toe aan de snelle diffusie van protonen, wat daarmee een belangrijke overweging is voor vervolgonderzoek.
In Hoofdstuk 5 kijken we verder naar de mechanische interacties tussen de tip van een atoomkrachtmicroscoop en een goud oppervlak waarvan de potentiaal is gecontroleerd, in een oplossing met sulfaten. Om precies te zijn brengen we de adhesie tussen de tip en het substraat in kaart, terwijl we de potentiaal veranderen. Met deze metingen zien we een duidelijke potentiaal,- en locatie afhankelijkheid van de adhesie. We koppelen dit aan de potentiaal afhankelijke adsorptie van sulfaten aan het goudoppervlak, wat de adhesie beïnvloedt door middel van de benodigde reorganisatienergie van het oppervlak. We observeren dat deze adsorptie op bepaalde plekken van het oppervlak plaatsvindt en dat de bijbehorende adhesie aanhoudt met de tijd. In contrast zien we dat deze locaties met hogere adhesie gerandomiseerd zijn over opeenvolgende potentiaal-cycli.
In het zesde en laatste Hoofdstuk (6) laten we de *scanning probe* systemen achter ons en richten ons op ionentransport in asymmetrische microscopische kanalen. Deze asymmetrie resulteert in rectificatie van de ionenstroom, wat normaliter wordt gedemonstreerd in systemen met afmetingen in de orde van de afschermingslengte. Deze rectificatie doet zich echter voor wanneer een relatief groter deel van de ionenstroom door de elektrische dubbellaag wordt geleid bij de kleine opening, vergeleken met de grote opening. Om deze reden is recent voorspeld dat dit fenomeen aanhoudt tot veel grotere lengteschalen, zolang een significant deel van de

stroom door de elektrische dubbellaag gaat, bij de kleine opening. In dit hoofdstuk observeren we rectificatie van de ionenstroom in kegelvormige microscopische kanalen, die we fabriceren in silicium membranen met een gefocusseerde ionenbundel. Hiermee valideren we de recente theoretische voorspellingen, en leveren de eerste demonstratie van ionenstroom rectificatie op deze schaal zonder chemische modificatie van de kanaalwand. Dit effect is specifiek interessant voor ons vanwege de potentie op het gebied van waterzuivering en energieopwekking. Deze gedemonstreerde integratie van grote rectificerende kanalen in een *CMOS*-compatibel platform is daarom een eerste stap richting membranen die resistent zijn tegen verstopping en met hoge doorvoer.

List of Publications

This thesis is based on the following peer-reviewed publication:

- M. Aarts, E. Alarcón-Lladó *Directed nanoscale metal deposition by the local perturbation of charge screening at the solid-liquid interface*, Nanoscale **11**, 18619-18627 (2019). (**Chapter 2**)
  MA and EAL designed the experiments. MA conducted the measurements. MA and EAL analyzed the data and drafted the manuscript.

The following are in preparation for submission:

- M. Aarts, S. van Vliet, R. Bliem, E. Alarcón-Lladó *Investigation of copper nanoscale electro-crystallization from a dilute electrolyte*, **to be submitted**. (**Chapter 3**)
  MA and EAL designed the experiments. M.A. conducted the electrodeposition and atomic force microscopy measurements. These measurements were analyzed by MA and EAL. SvV conducted the XPS measurements. XPS measurements were analyzed by SvV and RB. MA and EAL drafted the manuscript. All authors reviewed and commented on the manuscript.

- M. Aarts*, A. Reiser*, R. Schuster, R. Spolenak, E. Alarcón-Lladó. *Nanoscale metal electrodeposition through diffuse layer charging by potential pulses at an STM tip.* **In preparation (Chapter 4)**
  MA, AR, EAL and RSp designed the experiments. AR built the experimental setup with input from RS. MA conducted the experiments shown in this chapter, which were analyzed by MA and EAL. RSp and EAL supervised the project.

- M. Aarts, J. Carstens, E. Alarcón-Lladó, *Adhesion mapping of a potential-controlled gold surface in sulphate electrolytes with an atomic force microscope* **In preparation (Chapter 5)**
  MA and EAL designed the experiments. MA and JC built the setup. MA conducted the measurements. MA and EAL analyzed the results.

- M. Aarts*, R. Brakkee*, E. Alarcón-Lladó, *Ion current rectification in tapered silicon microchannels.* **In preparation (Chapter 6)**
  MA and EAL designed the experiments. RB conducted the measurements under supervision of MA and EAL. MA, RB, and EAL analyzed the results.

*Equal contribution

Other publications by the author:

- J. Dugay, M. Aarts, M. Giménez-Marqués, T. Kozlova, H.W. Zandbergen, E. Coronado, and H.S.J. van der Zant *Phase Transitions in Spin-Crossover Thin Films Probed by Graphene Transport Measurements*, Nano lett. **17**,186-193 (2016).
- M. Valenti, Y. Bleiji, J. Blanco-Portals, L.A. Muscarella, M. Aarts, F. Peiro, S. Estrade, E. Alarcón-Lladó, *Grain size control of crystalline III-V semiconductors at ambient conditions using electrochemically mediated growth*, J. Mat. Chem. A, **8**, 2752-2759 (2020).

Acknowledgements

I have thoroughly enjoyed the winding path of my PhD over the last four years, leading us to work on topics I would not have imagined at the start. As we delved into many topics we had no experience in, a primary concern is the access to information. Working from an institute with rather restricted access to publicly funded research, I would therefore start by acknowledging the people involved in the cOAlition S and Plan S initiative, and others who's efforts have enabled my research.
Along that line, AMOLF in particular facilitates exposure to many scientific descriptions and perspectives. I am very grateful to all the organizational efforts (and contributions) going into the weekly monday colloquia, the weekly colloquia within the center for nanophotonics, and additional meetings and symposia within the LMPV programme. Combined with the lively discussions during talks and posters this totals to a truly inspiring environment.

Furthermore, the work in this thesis would not have been possible without individual efforts of many people along the way. Firstly I would like to thank my supervisor, Esther. You once described the goal of the PhD to be able to have an enjoyable and substantive scientific conversation. With that goal in mind this was a resounding success from my perspective, time always flies when we are discussing experimental results or possible explanations. You are an extremely good motivator, which often provided the necessary boosts of energy as we struggled with the AFM setup. This also translated in a surprising speed and enthusiasm with which new group members adapted to work in the lab, often stretching regular working hours a bit.
As such, I am very thankful for the efforts of all the master students I had the pleasure to work with directly: Ilya, Alexandra, Rosa Rougoor, Rosa Brakkee, Jim, and Blaise whom all contributed to the work presented in this thesis. I would also like to thank the other regulars of the 3D PhotoVoltaics group. Nasim, your upbeat spirit makes all groupmeetings and lunches more enjoyable. Thank you also for reminding us to put the art in state-of-the-art. Marco, I am particularly grateful for your continued willingness to participate in my favorite lunchtime game: disagreeing-with-Marco. Yorick, you really provide the necessary structure that the rest of us so badly lack. Juliane, we mainly know you virtually, but I look forward to you visiting AMOLF soon. Daphne, I'm pretty sure we will survive working with the lead salts. Also Dion, your speed and creativity in making things for the lab has always amazed

me and many of our experiments were only possible due to your help. Daniël, you are already coming up with similar solutions with setups being 3D printed, in thematic fashion.
With throughput of people being as high as it is in the group, every (academic) year has a unique signature. I would like to thank Carles, Laura, and Giovanni for all the late-night labsessions; Jose and Susan for their new funky setups and surreal lunch conversations; Dominique for openly sharing fabrication frustrations; and Merlinde and Pepijn for helping us get through lockdown; Alex, Jos, and Mees for continuing this task and repopulating the lab.

I would further like to acknowledge our external collaborators. In particular Alain, for building the setup for the measurements in chapter 4 and (also Sabine) even letting me stay in your home during my first visit to Zürich. It was very nice to discuss the electrochemical scanning probe setup with someone facing the same problems. Sophia, for hosting me when visiting EPFL; Ralph for doing so at ETH, and for the discussions on the pulsed deposition. Stefan and Roland for the extremely rapid XPS measurements in chapter 3. Igor and Frieder for the discussions on electrochemical AFM.

Closer to home, everyone at AMOLF benefits from the excellent support. In particular I would like to thank the people who helped fabricate a multitude of electrochemical cells and designs: Marnix, Ricardo, Wessel, Niels, and Tom; Hinco, Marc, Marko, Marco, Ronald, and Duncan for help on lab, chemistry, lasers, software and electronics; Bob, Dimitry, Igor, Andries, and Hans for all the introductions and help in the nanocenter; Petra and Erny for communicating the results from chapter 2; and Henriëtte for logistical details and organizing the SPM day. Furthermore I would acknowledge all the other silent forces that keep AMOLF running smoothly, the continuing work of the Work's Council, and Mathijs, Sjoerd, Christiaan, Marnix, Jan-Bonne, and Melle for doing this with me for two years.
Additionally, I mention again the NP colloquia and all the nanophotonics groupleaders for making this happen, even virtually. I would thank all the contributions and discussions over the years by a sheer endless list of people from the center for nanophotonics. They have introduced me to many different perspectives on as many topics, also resulting in new experiments for which I thank in particular Jenny, Tom, Sven, Andrea, Verena, Magda, Christian, Julia, Ruslan, Isabelle, Robin, Benjamin, Lucie, Stefan, Jian-Yao, Eitan, Harshal, and Nick.

Laboring on a project for 4 years does not always come easily, and there are many people to thank outside the work sphere. As a somewhat organizationally-impaired person I am specifically grateful to all the people that have taken care of vacations and other activities; Tomas, Jochem, Bas, Bram, Joren, Toon, Rob, Okko, Wouter, Sander, Ainoa, Anneke, Inge, Joost, for skiing trips, life-threatening hikes, and games' nights; Members of Cosa Nostra for even more skiing and all the additional candy travels; Cas, Bram, Dennis, Teddy, Robin, and Bernie for Tromp-side football supporting and battling Amsterdam landlords; Also Daan, Koen, Roel, and Tijmen, for a lifetime of mainly afternoon gatherings as we seem to suffer from the same planning deficiency.
Finally I would like to thank all of my family. Paps en mams, for the unconditional support and always being available. Franke, the last stretch of writing is always stressful, and even more so during a global pandemic. I can now start making up for your patience during the last months of extended work,- days and weeks!

References

[1] Eigler, D. M. & Schweizer, E. K. Positioning single atoms with a scanning tunnelling microscope. *Nature* **344**, 524–526 (1990).

[2] Crommie, M. F., Lutz, C. P. & Eigler, D. M. Confinement of Electrons to Quantum Corrals on a Metal Surface. *Science* **262**, 218–220 (1993).

[3] Garcia, R., Knoll, A. W. & Riedo, E. Advanced Scanning Probe Lithography. *Nature nanotechnology* **9**, 577. (2014).

[4] Salaita, K. & Mirkin, C. A. Massively Parallel Dip-Pen Nanolithography with 55000-Pen Two-Dimensional Arrays. *Angewandte Chemie-International Edition* **45**, 7220 –7223 (2006).

[5] Hirt, L., Reiser, A., Spolenak, R. & Zambelli, T. Additive Manufacturing of Metal Structures at the Micrometer Scale. *Advanced Materials* **29**, 1604211 (2017).

[6] Ercolano, G. *et al.* Additive Manufacturing of Sub-Micron to Sub-mm Metal Structures with Hollow AFM Cantilevers. *Micromachines* **11**, 6 (2019).

[7] Schaedler, T. A. *et al.* Ultralight Metallic Microlattices. *Science* **334**, 962–965 (2011).

[8] Gansel, J. K. *et al.* Gold Helix Photonic Metamaterial as Broadband Circular Polarizer. *Science* **325**, 1513–1515 (2009).

[9] Cui, C., Gan, L., Heggen, M., Rudi, S. & Strasser, P. Compositional segregation in shaped Pt alloy nanoparticles and their structural behaviour during electrocatalysis. *Nature Materials* **12**, 765–771 (2013).

[10] Staikov, G. *Electrocrystallization in Nanotechnology* (Wiley-VCH, 2007).

[11] Compton, R. G. & Banks, C. E. *Understanding Voltammetry* (Imperial College Press, 2011), 2 edn.

[12] Kolb, D., Przasnyski, M. & Gerischer, H. Underpotential deposition of metals and work function differences. *Journal of Electroanalytical Chemistry and Interfacial Electrochemistry* **54**, 25–38 (1974).

[13] Liu, Y., Gokcen, D., Bertocci, U. & Moffat, T. P. Self-Terminating Growth of Platinum Films by Electrochemical Deposition. *Science* **338**, 1327–1330 (2012).

[14] Bard, A. J. & Faulkner, L. R. *Electrochemical methods: fundamentals and applications* (Wiley New York, 2001), 2 edn.

[15] Zach, M. P., Ng, K. H. & Penner, R. M. Molybdenum nanowires by electrodeposition. *Science* **290**, 2120–2123 (2000).

[16] Bonnet, N. & Marzari, N. First-Principles Prediction of the Equilibrium Shape of Nanoparticles Under Realistic Electrochemical Conditions. *Physical Review Letters* **110**, 086104 (2013).

[17] Huang, J. *et al.* Potential-induced nanoclustering of metallic catalysts during electrochemical CO2 reduction. *Nature Communications* **9**, 3117 (2018).

[18] Guo, L., Zhang, S. & Searson, P. Growth kinetics of disk-shaped copper islands in electrochemical deposition. *Physical Review E* **79**, 051601 (2009).

[19] Guo, L., Oskam, G., Radisic, A., Hoffmann, P. M. & Searson, P. C. Island growth in electrodeposition. *Journal of Physics D: Applied Physics* **44**, 443001 (2011).

[20] Wang, S., Tian, E. & Lung, C. Surface energy of arbitrary crystal plane of bcc and fcc metals. *Journal of Physics and Chemistry of Solids* **61**, 1295–1300 (2000).

[21] Arenz, M., Broekmann, P., Lennartz, M., Vogler, E. & Wandelt, K. In-situ Characterization of Metal/Electrolyte Interfaces: Sulfate Adsorption on Cu(111). *Physica Status Solidi (a)* **187**, 63–74 (2001).

[22] Siegfried, M. J. & Choi, K.-S. Directing the Architecture of Cuprous Oxide Crystals during Electrochemical Growth. *Angewandte Chemie* **117**, 3282–3287 (2005).

[23] Siegfried, M. J. & Choi, K.-S. Elucidating the Effect of Additives on the Growth and Stability of Cu 2 O Surfaces via Shape Transformation of Pre-Grown Crystals. *Journal of the American Chemical Society* **128**, 10356–10357 (2006).

[24] Guo, L. & Searson, P. C. Anisotropic Island Growth: A New Approach to Thin Film Electrocrystallization. *Langmuir* **24**, 10557–10559 (2008).

[25] Bazant, M. Z., Sabri Kilic, M., Storey, B. D. & Ajdari, A. Nonlinear electrokinetics at large voltages. *New Journal of Physics* **11**, 075016 (2009).

[26] Bazant, M. Z., Thornton, K. & Ajdari, A. Diffuse-charge dynamics in electrochemical systems. *Physical Review E* **70**, 021506 (2004).

[27] Collins, L. *et al.* Probing charge screening dynamics and electrochemical processes at the solid-liquid interface with electrochemical force microscopy. *Nature Communications* **5**, 3871 (2014).

[28] Li, W., Virtanen, J. A. & Penner, R. M. Nanometer-scale electrochemical deposition of silver on graphite using a scanning tunneling microscope. *Applied Physics Letters* **60**, 1181–1183 (1992).

[29] Li, W. *et al.* Mechanistic Study of Silver Nanoparticle Deposition Directed with the Tip of a Scanning Tunneling Microscope in an Electrolytic Environment. *The Journal of Physical Chemistry* **100**, 20103–20113 (1996).

[30] LaGraff, J. R. & Gewirth, A. A. Enhanced Electrochemical Deposition with an Atomic Force Microscope. *The Journal of Physical Chemistry* **98**, 11246–11250 (1994).

[31] LaGraff, J. R. & Gewirth, A. A. Nanometer-Scale Mechanism for the Constructive Modification of Cu Single Crystals and Alkanethiol Passivated Au(111) with an Atomic Force Microscope. *The Journal of Physical Chemistry* **99**, 10009–10018 (1995).

[32] Obermair, C., Wagner, A. & Schimmel, T. The atomic force microscope as a mechano-electrochemical pen. *Beilstein Journal of Nanotechnology* **2**, 659–664 (2011).

[33] Ullmann, R., Will, T. & Kolb, D. Nanostructuring of Electrode Surfaces by Tip-Induced Metal Deposition. *Berichte der Bunsengesellschaft für physikalische Chemie* **99**, 1414–1420 (1995).

[34] Kolb, D. M. Nanofabrication of Small Copper Clusters on Gold(111) Electrodes by a Scanning Tunneling Microscope. *Science* **275**, 1097–1099 (1997).

[35] Engelmann, G., Ziegler, J. & Kolb, D. Electrochemical fabrication of large arrays of metal nanoclusters. *Surface Science* **401**, L420–L424 (1998).

[36] Hofmann, D., Schindler, W. & Kirschner, J. Electrodeposition of nanoscale magnetic structures. *Applied Physics Letters* **73**, 3279–3281 (1998).

[37] Schindler, W., Hofmann, D. & Kirschner, J. Nanoscale electrodeposition : A new route to magnetic nanostructures ? *Journal of Applied Physics* **87**, 1998–2001 (2000).

[38] Schindler, W., Hofmann, D. & Kirschner, J. Localized Electrodeposition Using a Scanning Tunneling Microscope Tip as a Nanoelectrode. *Journal of The Electrochemical Society* **148**, C124 (2001).

[39] Schindler, W., Hugelmann, P., Hugelmann, M. & Kärtner, F. X. Localized electrochemical nucleation and growth of low-dimensional metal structures. *Journal of Electroanalytical Chemistry* **522**, 49–57 (2002).

[40] Liu, M. *et al.* Enhanced electrocatalytic CO2 reduction via field-induced reagent concentration. *Nature* **537**, 382–386 (2016).

[41] Dagata, J. A. *et al.* Modification of hydrogen-passivated silicon by a scanning tunneling microscope operating in air. *Applied Physics Letters* **56**, 2001–2003 (1990).

[42] Suryavanshi, A. P. & Yu, M.-F. Probe-based electrochemical fabrication of freestanding Cu nanowire array. *Applied Physics Letters* **88**, 083103 (2006).

[43] Suryavanshi, A. P. & Yu, M.-F. Electrochemical fountain pen nanofabrication of vertically grown platinum nanowires. *Nanotechnology* **18**, 105305 (2007).

[44] McKelvey, K., O'Connell, M. A. & Unwin, P. R. Meniscus confined fabrication of multidimensional conducting polymer nanostructures with scanning electrochemical cell microscopy (SECCM). *Chemical Communications* **49**, 2986 (2013).

[45] Hu, J. & Yu, M.-F. Meniscus-Confined Three-Dimensional Electrodeposition for Direct Writing of Wire Bonds. *Science* **329**, 313–316 (2010).

[46] Lin, Y.-P., Zhang, Y. & Yu, M.-F. Parallel Process 3D Metal Microprinting. *Advanced Materials Technologies* **4**, 1800393 (2019).

[47] Eliyahu, D., Gileadi, E., Galun, E. & Eliaz, N. Atomic Force Microscope-Based Meniscus-Confined Three-Dimensional Electrodeposition. *Advanced Materials Technologies* **5**, 1900827 (2020).

[48] Momotenko, D., Page, A., Adobes-Vidal, M. & Unwin, P. R. Write-Read 3D Patterning with a Dual-Channel Nanopipette. *ACS Nano* **10**, 8871–8878 (2016).

[49] Hirt, L. *et al.* Local surface modification via confined electrochemical deposition with FluidFM. *RSC Advances* **5**, 84517–84522 (2015).

[50] Hirt, L. *et al.* Template-Free 3D Microprinting of Metals Using a Force-Controlled Nanopipette for Layer-by-Layer Electrodeposition. *Advanced Materials* **28**, 2311–2315 (2016).

[51] Reiser, A. *Additive manufacturing of metals at small length scales - microstructure, properties and novel multi-metal electrochemical concepts.* Ph.D. thesis, ETH Zurich (2019).

[52] Mamin, H. J., Chiang, S., Birk, H., Guethne, P. & Rugar, D. Gold deposition from a scanning tunneling microscope tip. *Journal of Vacuum Science & Technology B: Microelectronics and Nanometer Structures* **9**, 1398 (1991).

[53] Wang, X.-D., Rubel, S. E., Purbach, U. & de Lozanne, A. L. Resistance of Ni nanowires fabricated by STM-CVD. *Proceedings SPIE, Micromachining and Imaging* **3009** (1997).

[54] Torrey, J. D. *et al.* Scanning Probe Direct-Write of Germanium Nanostructures. *Advanced Materials* **22**, 4639–4642 (2010).

[55] Vasko, S. E. *et al.* Serial and parallel Si, Ge, and SiGe direct-write with scanning probes and conducting stamps. *Nano Letters* **11**, 2386–2389 (2011).

[56] Vasko, S. E. *et al.* Insights into scanning probe high-field chemistry of diphenylgermane. *Physical Chemistry Chemical Physics* **13**, 4842 (2011).

[57] Xie, Z.-X. & Kolb, D. Spatially confined copper dissolution by an STM tip: a new type of electrochemical reaction? *Journal of Electroanalytical Chemistry* **481**, 177–182 (2000).

[58] Xie, Z., Cai, X., Tang, J., Chen, Y. & Mao, B. STM tip-induced nanoscale etching on the H-terminated n-Si(111) surfaces under the potential control. *Chemical Physics Letters* **322**, 219–223 (2000).

[59] Láng, G., Bakos, I. & Horányi, G. An alternative explanation of confined copper dissolution by an STM tip. *Journal of Electroanalytical Chemistry* **493**, 141–143 (2000).

[60] García, S. G., Salinas, D. R., Mayer, C. E., Lorenz, W. J. & Staikov, G. STM tip-induced local electrochemical dissolution of silver. *Electrochimica Acta* **48**, 1279–1285 (2003).

[61] Schuster, R., Kirchner, V., Xia, X., Bittner, A. & Ertl, G. Nanoscale electrochemistry. *Physical Review Letters* **80**, 5599–5602 (1998).

[62] Potzschke, R. T., Staikov, G., Lorenz, W. & Wiesbeck, W. Electrochemical Nanostructuring of n-Si(111) Single-Crystal Faces. *Journal of The Electrochemical Society* **146**, 141 (1999).

[63] Widmer, R. & Siegenthaler, H. Nanostructuring experiments in the system Ag(1 1 1)/Pb2+. *Electrochemistry Communications* **7**, 421–426 (2005).

[64] Schuster, R., Kirchner, V., Allongue, P. & Ertl, G. Electrochemical Micromachining. *Science* **289**, 98–101 (2000).

[65] Kirchner, V., Xia, X. & Schuster, R. Electrochemical nanostructuring with ultrashort voltage pulses. *Accounts of Chemical Research* **34**, 371–377 (2001).

[66] de Abril, O., Gündel, A., Maroun, F., Allongue, P. & Schuster, R. Single-step electrochemical nanolithography of metal thin films by localized etching with an AFM tip. *Nanotechnology* **19**, 325301 (2008).

[67] Lee, G. *et al.* Experimental and numerical study of electrochemical nanomachining using an AFM cantilever tip. *Nanotechnology* **21**, 185301 (2010).

[68] Kock, M., Kirchner, V. & Schuster, R. Electrochemical micromachining with ultrashort voltage pulses-a versatile method with lithographical precision. *Electrochimica Acta* **48**, 3213–3219 (2003).

[69] Hüsser, O. E. High-resolution deposition and etching of metals with a scanning electrochemical microscope. *Journal of Vacuum Science & Technology B: Microelectronics and Nanometer Structures* **6**, 1873 (1988).

[70] Lin, C. W., Fan, F.-r. F. & Bard, A. J. High Resolution Photoelectrochemical Etching of n - GaAs with the Scanning Electrochemical and Tunneling Microscope. *Journal of The Electrochemical Society* **134**, 1038–1039 (1987).

[71] Mandler, D. & Bard, A. J. A New Approach to the High Resolution Electrodeposition of Metals via the Feedback Mode of the Scanning Electrochemical Microscope. *Journal of The Electrochemical Society* **137**, 1079 (1990).

[72] Sarkar, S. & Mandler, D. Scanning Electrochemical Microscopy versus Scanning Ion Conductance Microscopy for Surface Patterning. *ChemElectroChem* **4**, 2981–2988 (2017).

[73] Borgwarth, K. & Heinze, J. Increasing the Resolution of the Scanning Electrochemical Microscope Using a Chemical Lens: Application to Silver Deposition. *Journal of The Electrochemical Society* **146**, 3285 (1999).

[74] Ufheil, J., Boldt, F. M., Börsch, M., Borgwarth, K. & Heinze, J. Microstructuring of solid-supported lipid layers using SAM pattern generation by scanning electrochemical microscopy and the chemical lens. *Bioelectrochemistry and Bioenergetics* **52**, 103–110 (2000).

[75] Ufheil, J., Heß, C., Borgwarth, K. & Heinze, J. Nanostructuring and nanoanalysis by scanning electrochemical microscopy (SECM). *Physical Chemistry Chemical Physics* 3185 (2005).

[76] Radtke, V., Heß, C., Souto, R. M. & Heinze, J. Electroless, Electrolytic and Galvanic Copper Deposition with the Scanning Electrochemical Microscope (SECM). *Zeitschrift für Physikalische Chemie* **220**, 393–406 (2006).

[77] Schneir, J. *et al.* Creating And Observing Surface Features With A Scanning Tunneling Microscope. *Proceedings SPIE, Scanning Microscopy Technologies and Applications* **0897** (1988).

[78] Madden, J. D. & Hunter, I. W. Three-dimensional microfabrication by localized electrochemical deposition. *Journal of Microelectromechanical Systems* **5**, 24–32 (1996).

[79] El-Giar, E. M., Said, R. A., Bridges, G. E. & Thomson, D. J. Localized Electrochemical Deposition of Copper Microstructures. *Journal of The Electrochemical Society* **147**, 586–591 (2000).

[80] Seol, S. K., Pyun, A. R., Hwu, Y., Margaritondo, G. & Je, J. H. Localized electrochemical deposition of copper monitored using real-time X-ray microradiography. *Advanced Functional Materials* **15**, 934–937 (2005).

[81] Jansson, A., Thornell, G. & Johansson, S. High Resolution 3D Microstructures Made by Localized Electrodeposition of Nickel. *Journal of The Electrochemical Society* **147**, 1810 (2000).

[82] Said, R. A. Microfabrication by localized electrochemical deposition: Experimental investigation and theoretical modelling. *Nanotechnology* **14**, 523–531 (2003).

[83] Schultze, J. W., Heidelberg, A., Rosenkranz, C., Schäpers, T. & Staikov, G. Principles of electrochemical nanotechnology and their application for materials and systems. *Electrochimica Acta* **51**, 775–786 (2005).

[84] Heidelberg, A., Rozenkranz, C., Schultze, J., Schäpers, T. & Staikov, G. Localized electrochemical oxidation of thin Nb Films in microscopic and nanoscopic dimensions. *Surface Science* **597**, 173–180 (2005).

[85] Bloeß, H., Staikov, G. & Schultze, J. W. AFM induced formation of SiO2 structures in the electrochemical nanocell. *Electrochimica Acta* **47**, 335–344 (2001).

[86] Nyffenegger, R. M. & Penner, R. M. Nanometer-Scale Surface Modification Using the Scanning Probe Microscope: Progress since 1991. *Chemical Reviews* **97**, 1195–1230 (1997).

[87] Kolb, D. M. & Simeone, F. C. Electrochemical nanostructuring with an STM: A status report. *Electrochimica Acta* **50**, 2989–2996 (2005).

[88] Bešter-Rogač, M. Electrical conductivity of concentrated aqueous solutions of divalent metal sulfates. *Journal of Chemical and Engineering Data* **53**, 1355–1359 (2008).

[89] Donepudi, V. S., Venkatachalapathy, R., Ozemoyah, P. O., Johnson, C. S. & Prakash, J. Electrodeposition of copper from sulfate electrolytes. Effects of Thiourea on Resistivity and Electrodeposition Mechanism of Copper. *Electrochemical and Solid-State Letters* **4**, 13–16 (2001).

[90] Fischer, S. A., Dunlap, B. I. & Gunlycke, D. Correlated dynamics in aqueous proton diffusion. *Chemical Science* **9**, 7126–7132 (2018).

[91] Aarts, M. & Alarcon-Llado, E. Directed nanoscale metal deposition by the local perturbation of charge screening at the solid-liquid interface. *Nanoscale* **11**, 18619–18627 (2019).

[92] Oja, S. M., Fan, Y., Armstrong, C. M., Defnet, P. & Zhang, B. Nanoscale Electrochemistry Revisited. *Analytical Chemistry* **88**, 414–430 (2016).

[93] Staikov, G. Nanoscale electrodeposition of low-dimensional metal phases and clusters. *Nanoscale* **8**, 13880–13892 (2016).

[94] Ghatkesar, M., Garza, H., Heuck, F. & Staufer, U. Scanning Probe Microscope-Based Fluid Dispensing. *Micromachines* **5**, 954–1001 (2014).

[95] Maynor, B. W., Li, Y. & Liu, J. Au "Ink" for AFM "Dip-Pen" Nanolithography. *Langmuir* **17**, 2575–2578 (2001).

[96] Je, J. H., Kim, J.-m. & Jaworski, J. Progression in the Fountain Pen Approach: From 2D Writing to 3D Free-Form Micro/Nanofabrication. *Small* **13**, 1600137 (2017).

[97] Szunerits, S., Pust, S. E. & Wittstock, G. Multidimensional electrochemical imaging in materials science. *Analytical and Bioanalytical Chemistry* **389**, 1103–1120 (2007).

[98] Lee, S. S., Fenter, P., Nagy, K. L. & Sturchio, N. C. Real-time observation of cation exchange kinetics and dynamics at the muscovite-water interface. *Nature Communications* **8**, 15826 (2017).

[99] Hugelmann, M., Hugelmann, P., Lorenz, W. & Schindler, W. Nanoelectrochemistry and nanophysics at electrochemical interfaces. *Surface Science* **597**, 156–172 (2005).

[100] Collins, L., Kilpatrick, J. I., Kalinin, S. V. & Rodriguez, B. J. Towards nanoscale electrical measurements in liquid by advanced KPFM techniques: a review. *Reports on Progress in Physics* **81**, 086101 (2018).

[101] Hiesgen, R., Eberhardt, D. & Meissner, D. Direct investigation of the electrochemical double layer using the STM. *Surface Science* **597**, 80–92 (2005).

[102] Harniman, R. L. *et al.* Real-time tracking of metal nucleation via local perturbation of hydration layers. *Nature Communications* **8**, 971 (2017).

[103] Martin-Jimenez, D., Chacon, E., Tarazona, P. & Garcia, R. Atomically resolved three-dimensional structures of electrolyte aqueous solutions near a solid surface. *Nature Communications* **7**, 12164 (2016).

[104] Fukuma, T., Kobayashi, K., Matsushige, K. & Yamada, H. True atomic resolution in liquid by frequency-modulation atomic force microscopy. *Applied Physics Letters* **87**, 034101 (2005).

[105] Umeda, K., Kobayashi, K., Minato, T. & Yamada, H. Atomic-Level Viscosity Distribution in the Hydration Layer. *Physical Review Letters* **122**, 116001 (2019).

[106] Voïtchovsky, K., Kuna, J. J., Contera, S. A., Tosatti, E. & Stellacci, F. Direct mapping of the solid-liquid adhesion energy with subnanometre resolution. *Nature Nanotechnology* **5**, 401–405 (2010).

[107] Siretanu, I. *et al.* Direct observation of ionic structure at solid-liquid interfaces: a deep look into the Stern Layer. *Scientific Reports* **4**, 4956 (2014).

[108] Hirata, K. *et al.* Visualizing charges accumulated in an electric double layer by three-dimensional open-loop electric potential microscopy. *Nanoscale* **10**, 14736–14746 (2018).

[109] Perry, D., Al Botros, R., Momotenko, D., Kinnear, S. L. & Unwin, P. R. Simultaneous Nanoscale Surface Charge and Topographical Mapping. *ACS Nano* **9**, 7266–7276 (2015).

[110] Huang, Z. *et al.* PeakForce Scanning Electrochemical Microscopy with Nanoelectrode Probes. *Microscopy Today* **24**, 18–25 (2016).

[111] Quickenden, T. I. & Xu, Q. Toward a Reliable Value for the Diffusion Coefficient of Cupric Ion in Aqueous Solution. *Journal of The Electrochemical Society* **143**, 1248–1253 (1996).

[112] Yan, J. *et al.* Formation and STM tip-induced reduction of ultra thin SnO film on Au(111). *Chemical Physics Letters* **373**, 575–579 (2003).

[113] Daryadel, S. *et al.* Localized Pulsed Electrodeposition Process for Three-Dimensional Printing of Nanotwinned Metallic Nanostructures. *Nano Letters* **18**, 208–214 (2018).

[114] Gebbie, M. A. *et al.* Long range electrostatic forces in ionic liquids. *Chemical Communications* **53**, 1214–1224 (2017).

[115] Sader, J. E. *et al.* A virtual instrument to standardise the calibration of atomic force microscope cantilevers. *Review of Scientific Instruments* **87**, 093711 (2016).

[116] Nečas, D. & Klapetek, P. Gwyddion: An open-source software for SPM data analysis. *Central European Journal of Physics* **10**, 181–188 (2012).

[117] Liao, H.-G. *et al.* Facet development during platinum nanocube growth. *Science* **345**, 916–919 (2014).

[118] Jin, R. *et al.* Photoinduced Conversion of Silver Nanospheres to Nanoprisms. *Science* **294**, 1901–1903 (2001).

[119] Tian, N., Zhou, Z.-Y., Sun, S.-G., Ding, Y. & Wang, Z. L. Synthesis of Tetrahexahedral Platinum Nanocrystals with High-Index Facets and High Electro-Oxidation Activity. *Science* **316**, 732–735 (2007).

[120] Robatjazi, H. *et al.* Plasmon-induced selective carbon dioxide conversion on earth-abundant aluminum-cuprous oxide antenna-reactor nanoparticles. *Nature Communications* **8**, 27 (2017).

[121] Huang, L. *et al.* Shape regulation of high-index facet nanoparticles by dealloying. *Science* **365**, 1159–1163 (2019).

[122] Lai, S. C., Lazenby, R. A., Kirkman, P. M. & Unwin, P. R. Nucleation, aggregative growth and detachment of metal nanoparticles during electrodeposition at electrode surfaces. *Chemical Science* **6**, 1126–1138 (2015).

[123] Borland, D. & Taylor Ii, R. M. Rainbow Color Map (Still) Considered Harmful. *IEEE Computer Graphics and Applications* **27**, 14–17 (2007).

[124] Mativetsky, J. M. *et al.* Graphene Transistors via in Situ Voltage-Induced Reduction of Graphene-Oxide under Ambient Conditions. *Journal of the American Chemical Society* **133**, 14320–14326 (2011).

[125] Basset, F. B. *et al.* High-Yield Fabrication of Entangled Photon Emitters for Hybrid Quantum Networking Using High-Temperature Droplet Epitaxy. *Nano Letters* **18**, 505–512 (2018).

[126] Grujicic, D. & Pesic, B. Electrodeposition of copper: the nucleation mechanisms. *Electrochimica Acta* **47**, 2901–2912 (2002).

[127] Grosse, P. *et al.* Dynamic Changes in the Structure, Chemical State and Catalytic Selectivity of Cu Nanocubes during CO2 Electroreduction: Size and Support Effects. *Angewandte Chemie - International Edition* **57**, 6192–6197 (2018).

[128] Beverskog, B. & Puigdomenech, I. Revised Pourbaix Diagrams for Copper at 25 to 300°C. *Journal of The Electrochemical Society* **144**, 3476–3483 (1997).

[129] Siegfried, M. J. & Choi, K.-S. Electrochemical Crystallization of Cuprous Oxide with Systematic Shape Evolution. *Advanced Materials* **16**, 1743–1746 (2004).

[130] Zhang, L. *et al.* Cu2O-CuO composite microframes with well-designed micro/nano structures fabricated via controllable etching of Cu2O microcubes for CO gas sensors. *CrystEngComm* **15**, 7462 (2013).

[131] Kartal, C., Hanedar, Y., Öznülüer, T. & Demir, Ü. Stoichiometry, Morphology, and Size-Controlled Electrochemical Fabrication of Cu x O (x = 1, 2) at Underpotential. *Langmuir* **33**, 3960–3967 (2017).

[132] Biesinger, M. C. Advanced analysis of copper X-ray photoelectron spectra. *Surface and Interface Analysis* **49**, 1325–1334 (2017).

[133] Guo, L. & Searson, P. C. Influence of anion on the kinetics of copper island growth. *Nanoscale* **2**, 2431 (2010).

[134] Zhan, D. *et al.* Electrochemical micro/nano-machining: Principles and practices. *Chemical Society Reviews* **46**, 1526–1544 (2017).

[135] Ma, X., Bán, A. & Schuster, R. Electrochemical machining of gold microstructures in LiCl/dimethyl sulfoxide. *ChemPhysChem* **11**, 616–621 (2010).

[136] Ma, X. & Schuster, R. Locally enhanced cathodoluminescence of electrochemically fabricated gold nanostructures. *Journal of Electroanalytical Chemistry* **662**, 12–16 (2011).

[137] Abbott, A. P., Ballantyne, A., Harris, R. C., Juma, J. A. & Ryder, K. S. A Comparative Study of Nickel Electrodeposition Using Deep Eutectic Solvents and Aqueous Solutions. *Electrochimica Acta* **176**, 718–726 (2015).

[138] Ribeiro, A. C. F., Lobo, V. M. M. & Natividade, J. J. S. Diffusion Coefficients in Aqueous Solutions of Cobalt Chloride at 298.15 K. *Journal of Chemical & Engineering Data* **47**, 539–541 (2002).

[139] Butler, J. N. Electrochemistry in dimethyl sulfoxide. *Journal of Electroanalytical Chemistry and Interfacial Electrochemistry* **14**, 89–116 (1967).

[140] Zhao, C., Bai, X. & Xu, L. Controlled Electrochemical Nanomachining with Adjustable Capacitance. *Journal of The Electrochemical Society* **165**, E269–E273 (2018).

[141] Legrand, L., Tranchant, A. & Messina, R. Electrodeposition Studies of Aluminum on Tungsten Electrode from DMSO 2 Electrolytes: Determination of AlIII Species Diffusion Coefficients. *Journal of The Electrochemical Society* **141**, 378–382 (1994).

[142] Faisal, F. *et al.* Electrifying model catalysts for understanding electrocatalytic reactions in liquid electrolytes. *Nature Materials* **17**, 592–598 (2018).

[143] Fréchette, J. & Vanderlick, T. K. Double Layer Forces over Large Potential Ranges as Measured in an Electrochemical Surface Forces Apparatus. *Langmuir* **17**, 7620–7627 (2001).

[144] Fréchette, J. & Vanderlick, T. K. Electrocapillary at Contact: Potential-Dependent Adhesion between a Gold Electrode and a Mica Surface. *Langmuir* **21**, 985–991 (2005).

[145] Israelachvili, J. N. *et al.* The Intersection of Interfacial Forces and Electrochemical Reactions. *The Journal of Physical Chemistry B* **117**, 16369–16387 (2013).

[146] Roldan Cuenya, B. Metal Nanoparticle Catalysts Beginning to Shape-up. *Accounts of Chemical Research* **46**, 1682–1691 (2013).

[147] Li, H. *et al.* Kinetic Study of Hydrogen Evolution Reaction over Strained MoS_2 with Sulfur Vacancies Using Scanning Electrochemical Microscopy. *Journal of the American Chemical Society* **138**, 5123–5129 (2016).

[148] Suchorski, Y. *et al.* The role of metal/oxide interfaces for long-range metal particle activation during CO oxidation. *Nature Materials* **17**, 519–522 (2018).

[149] Giannakakis, G., Flytzani-Stephanopoulos, M. & Sykes, E. C. H. Single-Atom Alloys as a Reductionist Approach to the Rational Design of Heterogeneous Catalysts. *Accounts of Chemical Research* **52**, 237–247 (2019).

[150] Leite, F. L., Bueno, C. C., Da Róz, A. L., Ziemath, E. C. & Oliveira, O. N. Theoretical Models for Surface Forces and Adhesion and Their Measurement Using Atomic Force Microscopy. *International Journal of Molecular Sciences* **13**, 12773–12856 (2012).

[151] Wang, R. *et al.* Operando Atomic Force Microscopy Reveals Mechanics of Structural Water Driven Battery-to-Pseudocapacitor Transition. *ACS Nano* **12**, 6032–6039 (2018).

[152] Zhao, C., Ebeling, D., Siretanu, I., van den Ende, D. & Mugele, F. Extracting local surface charges and charge regulation behavior from atomic force microscopy measurements at heterogeneous solid-electrolyte interfaces. *Nanoscale* **7**, 16298–16311 (2015).

[153] Nellist, M. R. *et al.* Potential-sensing electrochemical atomic force microscopy for in operando analysis of water-splitting catalysts and interfaces. *Nature Energy* **3**, 46–52 (2018).

[154] Raiteri, R., Grattarola, M. & Butt, H.-J. Measuring Electrostatic Double-Layer Forces at High Surface Potentials with the Atomic Force Microscope. *The Journal of Physical Chemistry* **100**, 16700–16705 (1996).

[155] Serafin, J. M. & Gewirth, A. A. Measurement of adhesion force to determine surface composition in an electrochemical environment. *Journal of Physical Chemistry B* **101**, 10833–10838 (1997).

[156] Serafin, J. M., Hsieh, S.-J., Monahan, J. & Gewirth, A. A. Potential Dependent Adhesion Forces on Bare and Underpotential Deposition Modified Electrode Surfaces. *The Journal of Physical Chemistry B* **102**, 10027–10033 (1998).

[157] Sinniah, S. K., Steel, A. B., Miller, C. J. & Reutt-Robey, J. E. Solvent Exclusion and Chemical Contrast in Scanning Force Microscopy. *Journal of the American Chemical Society* **118**, 8925–8931 (1996).

[158] Noy, A., Sanders, C. H., Vezenov, D. V., Wong, S. S. & Lieber, C. M. Chemically-Sensitive Imaging in Tapping Mode by Chemical Force Microscopy: Relationship between Phase Lag and Adhesion. *Langmuir* **14**, 1508–1511 (1998).

[159] Grierson, D. S., Flater, E. E. & Carpick, R. W. Accounting for the JKR-DMT transition in adhesion and friction measurements with atomic force microscopy. *Journal of Adhesion Science and Technology* **19**, 291–311 (2005).

[160] Lipkowski, J., Shi, Z., Chen, A., Pettinger, B. & Bilger, C. Ionic adsorption at the Au(111) electrode surface. *Journal of Electroanalytical Chemistry* **467**, 342–353 (1999).

[161] Kondo, T. *et al.* Structure of Au(111) and Au(100) Single-Crystal Electrode Surfaces at Various Potentials in Sulfuric Acid Solution Determined by In Situ Surface X-ray Scattering. *The Journal of Physical Chemistry C* **111**, 13197–13204 (2007).

[162] Hintze, J. L. & Nelson, R. D. Violin Plots: A Box Plot-Density Trace Synergism. *The American Statistician* **52**, 181 (1998).

[163] Kasuya, M. *et al.* Anion Adsorption on Gold Electrodes Studied by Electrochemical Surface Forces Measurement. *Journal of Physical Chemistry C* **120**, 15986–15992 (2016).

[164] Nishizawa, M., Menon, V. P. & Martin, C. R. Metal Nanotubule Membranes with Electrochemically Switchable Ion-Transport Selectivity. *Science* **268**, 700–702 (1995).

[165] Siwy, Z. & Fuliński, A. Fabrication of a Synthetic Nanopore Ion Pump. *Physical Review Letters* **89**, 198103 (2002).

[166] Van Der Heyden, F. H., Stein, D. & Dekker, C. Streaming currents in a single nanofluidic channel. *Physical Review Letters* **95**, 9–12 (2005).

[167] Vlassiouk, I. & Siwy, Z. S. Nanofluidic Diode. *Nano Letters* **7**, 552–556 (2007).

[168] Kalman, E. B., Vlassiouk, I. & Siwy, Z. S. Nanofluidic Bipolar Transistors. *Advanced Materials* **20**, 293–297 (2008).

[169] Stein, D., Kruithof, M. & Dekker, C. Surface-charge-governed ion transport in nanofluidic channels. *Physical Review Letters* **93**, 1–4 (2004).

[170] Smeets, R. M. M. *et al.* Salt Dependence of Ion Transport and DNA Translocation through Solid-State Nanopores. *Nano Letters* **6**, 89–95 (2006).

[171] Wei, C., Bard, A. J. & Feldberg, S. W. Current Rectification at Quartz Nanopipet Electrodes. *Analytical Chemistry* **69**, 4627–4633 (1997).

[172] Siwy, Z., Heins, E., Harrell, C. C., Kohli, P. & Martin, C. R. Conical-Nanotube Ion-Current Rectifiers: The Role of Surface Charge. *Journal of the American Chemical Society* **126**, 10850–10851 (2004).

[173] Siria, A., Bocquet, M.-l. & Bocquet, L. New avenues for the large-scale harvesting of blue energy. *Nature Reviews Chemistry* **1**, 0091 (2017).

[174] Xiao, K., Jiang, L. & Antonietti, M. Ion Transport in Nanofluidic Devices for Energy Harvesting. *Joule* **3**, 2364–2380 (2019).

[175] Siwy, Z. S. Ion-Current Rectification in Nanopores and Nanotubes with Broken Symmetry. *Advanced Functional Materials* **16**, 735–746 (2006).

[176] Cheng, L.-J. & Guo, L. J. Rectified Ion Transport through Concentration Gradient in Homogeneous Silica Nanochannels. *Nano Letters* **7**, 3165–3171 (2007).

[177] Xiong, T., Zhang, K., Jiang, Y., Yu, P. & Mao, L. Ion current rectification: from nanoscale to microscale. *Science China Chemistry* **62**, 1346–1359 (2019).

[178] He, X. *et al.* Micrometer-Scale Ion Current Rectification at Polyelectrolyte Brush-Modified Micropipets. *Journal of the American Chemical Society* **139**, 1396–1399 (2017).

[179] Lin, C.-y., Yeh, L.-h. & Siwy, Z. S. Voltage-Induced Modulation of Ionic Concentrations and Ion Current Rectification in Mesopores with Highly Charged Pore Walls. *The Journal of Physical Chemistry Letters* **9**, 393–398 (2018).

[180] Lin, C.-Y., Combs, C., Su, Y.-S., Yeh, L.-H. & Siwy, Z. S. Rectification of Concentration Polarization in Mesopores Leads To High Conductance Ionic Diodes and High Performance Osmotic Power. *Journal of the American Chemical Society* **141**, 3691–3698 (2019).

[181] Bocquet, L. & Charlaix, E. Nanofluidics, from bulk to interfaces. *Chemical Society Reviews* **39**, 1073–1095 (2010).

[182] Poggioli, A. R., Siria, A. & Bocquet, L. Beyond the Tradeoff: Dynamic Selectivity in Ionic Transport and Current Rectification. *The Journal of Physical Chemistry B* **123**, 1171–1185 (2019).

[183] Dal Cengio, S. & Pagonabarraga, I. Confinement-controlled rectification in a geometric nanofluidic diode. *The Journal of Chemical Physics* **151**, 044707 (2019).

[184] Harned, H. S. & Nuttall, R. L. The Diffusion Coefficient of Potassium Chloride in Dilute Aqueous Solution. *Journal of the American Chemical Society* **69**, 736–740 (1947).

[185] Lobo, V. M., Ribeiro, A. C. & Verissimo, L. M. Diffusion coefficients in aqueous solutions of potassium chloride at high and low concentrations. *Journal of Molecular Liquids* **78**, 139–149 (1998).

[186] Fan, R., Huh, S., Yan, R., Arnold, J. & Yang, P. Gated proton transport in aligned mesoporous silica films. *Nature Materials* **7**, 303–307 (2008).

[187] Nam, S.-w., Rooks, M. J., Kim, K.-b. & Rossnagel, S. M. Ionic Field Effect Transistors with Sub-10 nm Multiple Nanopores. *Nano Letters* **9**, 2044–2048 (2009).

[188] Taghipoor, M., Bertsch, A. & Renaud, P. An improved model for predicting electrical conductance in nanochannels. *Physical Chemistry Chemical Physics* **17**, 4160–4167 (2015).

[189] Inamdar, S. N., Bhat, M. A. & Haram, S. K. Construction of Ag/AgCl Reference Electrode from Used Felt-Tipped Pen Barrel for Undergraduate Laboratory. *Journal of Chemical Education* **86**, 355 (2009).